Stable and Efficient Perovskite Solar Cells Fabricated in Ambient Air

by

Muhammad Awais

A Dissertation Submitted in Partial Fulfillment of the Requirements for the Degree of

DOCTOR OF PHILOSOPHY

In the Department of Electrical and Computer Engineering

University of Victoria

We acknowledge and respect the Lək̓ ʷəŋən (Songhees and Esquimalt) Peoples on whose territory the university stands, and the Lək̓ ʷəŋən and W̱SÁNEĆ Peoples whose historical relationships with the land continue to this day

Stable and Efficient Perovskite Solar Cells Fabricated in Ambient Air

by

Muhammad Awais

B.Sc., Bahauddin Zakariya University, Pakistan, 2015
M.S., University of Science and Technology, South Korea, 2020

Supervisory Committee

Prof. Dr. Makhsud I. Saidaminov (Supervisor)

Department of Electrical and Computer Engineering

Prof. Dr. Thomas Tiedje, Departmental Member

Department of Electrical and Computer Engineering
Supervisory Committee

Prof. Dr. Alexandre Brolo, Outside Member

Department of Chemistry
Supervisory Committee

Abstract

Search for efficient energy materials has been at the forefront of mitigating climate change and meeting ever-growing energy demand. Solar cells have proven to facilitate both challenges, and significant efforts were dedicated in improving the current state-of-art technology, *i.e.,* silicon solar cells, but also to look for more efficient and inexpensive materials. Among them, perovskite solar cells (PSCs) have shown promising results within a decade and are now at the edge of commercialization.

This thesis focuses on addressing the key challenges in fabricating stable and efficient PSCs under ambient conditions, a crucial step toward their scalable production and industrial manufacturing viability. While PSCs exhibit outstanding optoelectronic properties, their performance and stability are compromised by both extrinsic environmental factors (moisture, heat, oxygen) and intrinsic material/interface instabilities. This thesis adopts a comprehensive approach by developing robust ambient-air fabrication protocols to overcome environmental sensitivity, and surface passivation of electron transport layer and perovskite towards scalable fabrication of efficient perovskite solar cells. By systematically addressing these extrinsic and intrinsic stability challenges through material engineering, interface optimization, and reliable encapsulation methods, this bridges the gap between laboratory-scale fabrication and industrially relevant manufacturing requirements for PSCs.

Chapter 1 provides an overview of the global energy landscape, highlighting the environmental impacts of non-renewable resources and the pivotal role of solar energy in addressing these challenges. Focusing on photovoltaic technologies, it introduces PSCs as a

promising solution, detailing their crystal structure and optoelectronic properties. The chapter systematically reviews PSC fabrication, covering perovskite composition selection, role of charge transport layers, and metal electrode. It concludes with performance characterization metrics and device improvement strategies, providing a foundation for advancing PSC technology in subsequent research.

In Chapter 2, the thesis addresses the challenge of extrinsic factors by developing optimized methods and protocols for ambient-air fabrication. A key component of this work involves a comparative study of two widely reported perovskite compositions: CsMAFA and MAFA (Cs: cesium; MA: methylammonium, $CH_3NH_3^+$; FA: formamidinium, $HC(NH_2)_2^+$). This chapter reveals that the CsMAFA perovskite exhibits instability in ambient air, attributed to the hygroscopic nature of cesium. To evaluate long-term operational stability, an accelerated aging protocol to test encapsulated devices under extreme conditions is also developed. This chapter achieves a milestone of 20% efficiency for PSCs made in ambient conditions.

Chapter 3 focuses on the grain boundary degradation in perovskite films, which is one of the major sources of degradation. A selective passivation strategy using biphenyl-containing molecules that specifically interact with PbI_2-rich interfaces at grain boundaries while remaining inert toward the perovskite is developed. This targeted approach results in significant improvements in optoelectronic properties, extending the radiative recombination lifetime from 1 µs to 2.7 µs. When implemented in ambient-air fabricated devices, this technique demonstrates excellent reproducibility, with champion device achieving an efficiency of 21% and consistently high open-circuit voltages of ~1.1 V.

Chapter 4 introduces chemical bath deposition method for fabricating SnO_2 electron transport layers in fully scalable, ambient-air-processed perovskite solar cells. The optimized deposition approach enables uniform, high-quality SnO_2 films that enhance charge extraction and minimize interfacial recombination. PSCs fabricated entirely using scalable methods under ambient conditions achieve an efficiency of 24.5%. The devices demonstrated excellent photovoltaic parameters, including an open-circuit voltage of ~1.14, validating the effectiveness of this scalable SnO_2 deposition technique for high-performance all-scalable PSC fabrication.

Finally, this thesis concludes with the conclusion and outlook in Chapter 5.

Table of Contents

Abbreviations

CBM	Conduction band minimum
CB	Chlorobenzene
CBD	Chemical bath deposition
CTL	Charge transport layer
DMF	Dimethylformamide
DMSO	Dimethyl sulfoxide
ETL	Electron transportation layer
FF	Fill factor
GHG	Greenhouse gases
HTL	Hole transportation layer
IRENA	International Renewable Energy Agency
ITO	Indium doped tin oxide
ISOS	International Summit on Organic Photovoltaic Stability
J_{SC}	Short-circuit current density
J_{MPP}	Current density at maximum power point
JV	Current-voltage
LED	Light-emitting diode
2ME	2-Methoxyethanol
MeO-2PACz	[2-(3,6-dimethoxy-9H-carbazol-9-yl)ethyl]phosphonic acid
MPP	Maximum power point
n-i-p	Negative-intrinsic-positive
NMP	N-Methyl-2-pyrrolidone
NREL	National Renewable Energy Laboratory
2PACz	[2-(9H-carbazol-9-yl)ethyl]phosphonic acid
PCE	Power conversion efficiency
p-i-n	Positive-intrinsic-negative
PSC	Perovskite solar cell
PL	Photoluminescence
PTAA	poly(triaryl amine)
RH	Relative humidity
SAM	Self-assembled monolayer
SEM	Scanning electron microscopy

Spiro-OMeTAD	2,2',7,7'-Tetrakis-(N,N-di-4-methoxyphenylamino)-9,9'-spirobifluorene
S-Q	Shockley-Queisser
TCO	Transparent conductive oxide
TRPL	Time-resolved photoluminescence
UPS	Ultraviolet photoelectron spectroscopy
UV-vis	Ultraviolet–visible spectrophotometry
VBM	Valence band maximum
V_{OC}	Open-circuit voltage
V_{MPP}	Voltage at maximum power point
XRD	X-ray diffraction
XPS	X-ray photoemission spectroscopy

Figures

Tables

Acknowledgement

All praise and gratitude to the Almighty God, who bestowed upon me the health, patience, and perseverance to achieve this milestone. The research I conducted during my PhD at the University of Victoria would not have been possible without the unwavering guidance, mentorship, and support of my advisor, Dr. Makhsud I. Saidaminov, to whom I am eternally indebted. I also extend my sincere gratitude to Dr. Thomas Tiedje and Dr. Alexandre Brolo for their invaluable insights and encouragement throughout my academic journey. My gratitude also goes out to ECE and Chemistry staff members who have been very kind and supportive throughout my time at UVic.

I am profoundly grateful to my colleagues—Yameen, Parinaz, Wanlong, Xingnan, Vishal, Reza, Dongyang, Victor, Sam, Augusto, Aleks, Dr. Emily and Dr. Sergey—for their pivotal contributions to my research. My heartfelt thanks also go to my friends, including Dr. Shams, Dr. Abubakar, Dr. Haris, Dr. Awais, Atta, Zain, Ammad, Mufaz, Aleem, Farjeel, Adnan, Kamran, Faisal, Mujahid, Noman, Umair, Mumtaz, and Zuhaib, for their camaraderie and moral support.

To my family, whose unwavering love and sacrifices laid the foundation for my success: I owe everything to them. My father, Prof. Malik Altaf Hussain; my father-in-law, Malik Abdul Hafeez; my mother, Nadra Yasmin; my sisters (Nimra, Ayesha, Iqra, Quba, Dua, Ahad, Sadia, Sajida, Maria, and my beloved youngest sister Anzish Zahra, and nephew Malik Moosa); and my brothers (Haseeb, Qaiser, Dr. Rashid, Judge Yasir, Abubakar, Shahid, Usman, Zubair, Vicky, Shakeel, Yasir, Khizer, Behzad, and Shahzad)—I owe everything to your collective strength and encouragement. My parents spared no effort in nurturing my ambitions; their resilience and sacrifices remain my greatest inspiration.

Lastly, and most profoundly, I owe immeasurable gratitude to my beloved wife, Asma Hafeez, whose boundless love, resilience, and sacrifices have been the bedrock of this journey. Her unwavering support transcended the immense challenges of a prolonged long-distance marriage—a testament to her extraordinary strength and selflessness. While I pursued this path, she gracefully relinquished personal aspirations, and shouldered countless responsibilities alone, all to nurture our bond and preserve its trust, sincerity, and harmony. Her sacrifices were not mere acts of endurance but profound gestures of love that anchored me through moments of doubt and distance. Words fall short of capturing the depth of her contributions; her unwavering belief in our shared vision transformed challenges into triumphs. She is not only my partner but the cornerstone of my strength, the quiet force behind every achievement, and the heart of this journey.

Chapter 1.

Energy and Perovskite Solar Cells

1.1 Why do we need energy?

The need for energy is deeply intertwined with the evolution of human civilization. In the earliest days of human existence, they relied on energy in its most basic form, for example, discovery of fire provided warmth and means to cook which improved their health. After these basic harnessing means of energy and with growth of human civilization, the energy generation and harnessing systems evolved into more complex forms.

Today, energy has become the backbone of modern civilization. From switching on a bulb to our body, everything in the universe needs energy. It is the primary driving force for the economic growth, technological advancements and social development. The energy in our bodies is supplied by the food that we eat, and energy to the bulbs is supplied by the (electric) generators. While world faces challenges in all forms of energy which is required for human existence, the most vulnerable sector (in terms of demand and supply) has become electrical energy. The growing global demand for energy, coupled with the rapid depletion of fossil fuels, has necessitated a shift toward unconventional and sustainable energy sources. In today's world, nearly every aspect of modern life relies on energy to perform basic functions, making it imperative to identify and harness alternative energy sources. These alternatives, known as renewable energy resources, are derived from natural processes and their installed capacity is consistently increasing over years, as reported by the International Renewable Energy Agency (IRENA)[1] (**Figure 1-1**).

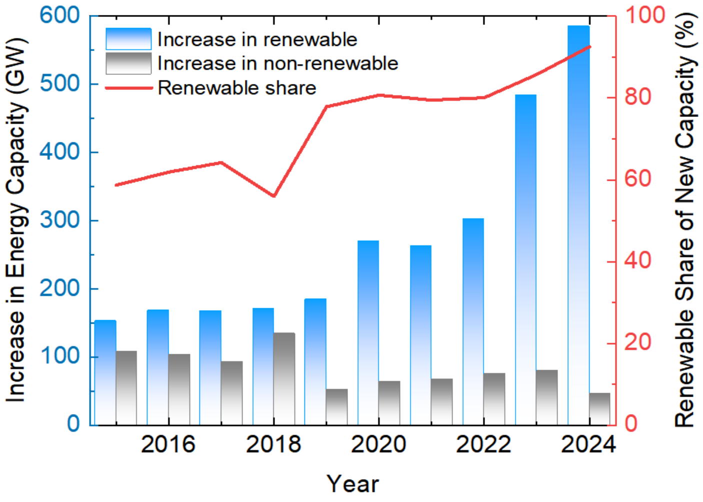

Figure 1-1. Total renewable energy generation capacity growth between 2015 to 2024. The figure is courtesy to International Renewable Energy Agency (IRENA).[1]

1.2 World energy overview

The global energy system is characterized by a complex interplay of supply and demand, influenced by economic growth, population expansion, technological advancements, and geopolitical factors. Global primary energy (includes both conventional and renewable sources of energy) consumption increased to more than 180,000 TWh in the year 2023 compared to about 120,000 TWh in the year 2000, and this trend continues to grow, averaging around 1% to 2% per year.[2] It is interesting to note that fossil fuels-based energy still accounts for more than 80% of the global energy mix, and renewable resources account for about 15% (and nuclear energy ~5%) in 2023 compared to ~7% in 2000.[2] Electricity is a major sector for increased demand in energy where demand nearly doubled, from 15,277 TWh in the year 2000 to 29,471 TWh in 2023.[2,3] However, the reliance on fossil fuels has led to significant environmental challenges, including the accumulation of carbon dioxide (CO_2) and other greenhouse gases (GHG) in the atmosphere, contributing to global climate change.[4–7]

The uneven distribution of energy resources and the geopolitical tensions surrounding their extraction and trade further complicate the global energy landscape. For instance, oil and natural gas reserves are concentrated in a few regions, creating dependencies and vulnerabilities for energy-importing countries. In contrast, renewable energy resources, such as solar and wind, are more evenly distributed, democratic and offer a pathway to greater energy independence and security.

1.2.1. Supply and demand of energy

The supply and demand of energy are influenced by a multitude of factors, including population growth, economic development, technological innovation, and policy frameworks. On the demand side, the rapid industrialization of developing nations, coupled with rising living standards, has led to a surge in energy consumption. The transportation, industrial, and residential sectors are the largest consumers of energy, with electricity generation being a critical component of the global energy system.[8,9]

On the supply side, the energy mix is dominated by fossil fuels, which provide a reliable and cost-effective source of energy but come with significant environmental and social costs. The extraction, processing, and combustion of fossil fuels release large quantities of CO_2, methane, and other pollutants, contributing to climate change and public health issues. In recent years, there has been a growing emphasis on diversifying the energy supply by integrating renewable energy sources, improving energy efficiency, and adopting cleaner technologies.

The imbalance between energy supply and demand is further exacerbated by the intermittent nature of some renewable energy sources, such as solar and wind, which require advanced storage solutions and grid management systems to ensure a stable and reliable energy supply. Addressing these challenges requires a holistic approach that combines technological innovation, policy support, and international cooperation.

1.3 Resources of energy

Energy resources can be broadly classified into two categories: conventional and renewable. Conventional energy resources include fossil fuels (coal, oil, and natural gas) and nuclear energy, which have been the backbone of global energy systems for decades. These resources are characterized by their high energy density and established infrastructure but are associated with significant environmental and geopolitical challenges.

Renewable energy resources, on the other hand, are derived from natural processes that are continuously replenished. These include solar, wind, hydro, geothermal, and biomass energy. Unlike fossil fuels, renewable energy sources produce little to no greenhouse gas emissions during operation, making them a key component of strategies to combat climate change. Additionally, renewable energy resources are abundant and widely distributed, reducing the risk of supply disruptions and enhancing energy security.[10,11]

1.3.1 Renewable energy

Renewable energy not only addresses the increasing energy demand but also plays a critical role in mitigating the adverse effects of climate change. Conventional energy sources, such as coal, oil, and natural gas, are major contributors to air pollution, GHG emissions, and the contamination of water and soil. In contrast, renewable energy sources have minimal to no negative environmental impact. For instance, global CO_2 equivalent emissions from the power sector were 10.9 gigatons in 2005 and are projected to rise to 18.7 gigatons annually by 2030 if current trends continue.[12] However, a report suggests that more efficient utilization of renewable energy could reduce CO_2 emissions by up to 70% by 2050.[13] Such a reduction would significantly mitigate climate change and help achieve the global target of limiting warming to below 2°C by curbing GHG emissions.[14]

The importance of renewable energy for sustainable development cannot be overstated. **Table 1-1** highlights the top 10 countries with the highest CO_2 emissions as of 2009, which collectively account for nearly 70% of global emissions.[15] China alone contributes 25.4% of total global CO_2 emissions, although its per capita emissions remain relatively low compared to other top emitters. United States has the highest per capita CO_2 emissions among these nations. This disparity underscores the need for a global effort to transition to renewable energy, particularly in high-emitting countries, to ensure a sustainable and equitable future.

By prioritizing renewable energy, the world can not only meet its energy needs but also protect the environment, reduce health risks associated with pollution, and combat the escalating threat of climate change. This transition is essential for achieving long-term sustainability and ensuring a healthier planet for future generations.

Table 1-1. Top 10 countries with the highest CO_2 emissions by 2009.[15]

Country	Annual CO_2 emissions (million tons)	% of global total	Per capita (tons)
China	7710.50	25.4	5.83
United States	5424.53	17.8	17.67
India	1602.12	5.27	1.38
Russia	1572.07	5.17	11.23
Japan	1097.96	3.61	8.64
Germany	765.56	2.52	9.30
Canada	540.97	1.78	16.15
South Korea	528.13	1.74	10.89
Iran	527.18	1.73	6.94
UK	519.94	1.71	8.35

1.3.2 Types of renewable energy

Renewable energy encompasses a diverse range of technologies and resources, each with unique characteristics and applications. The major types of renewable energy resources include:

1. **Solar energy:** Harnessed from sunlight using photovoltaic (PV) cells or solar thermal systems, solar energy is one of the most abundant and widely available renewable energy sources.
2. **Wind energy:** Generated by converting the kinetic energy of wind into electricity using wind turbines, wind energy is a rapidly growing sector with significant potential for large-scale deployment.
3. **Hydropower:** Derived from the energy of flowing or falling water, hydropower is a mature and reliable renewable energy technology, accounting for a significant share of global electricity generation.

4. **Geothermal energy:** Tapped from the heat stored beneath the Earth's surface, geothermal energy is used for electricity generation and direct heating applications.
5. **Biomass energy:** Produced from organic materials such as plant and animal waste, biomass can be converted into electricity, heat, or biofuels.

Each of these renewable energy sources has its advantages and limitations, and their suitability depends on factors such as geographic location, resource availability, and technological feasibility.

From the above-mentioned types of renewable energy resources hydroelectricity, solar energy and wind energy are widely popular and installed commercially in many parts of the world. Our scope in this thesis is largely related to solar energy; therefore, we will now elucidate the importance of solar energy.

1.4 Solar energy

Human civilization has seen rapid growth in the past few decades. It is evident by the fact that for the first time in recorded human history, more than half of the world’s population has been living in the cities since 2007.[16] With the unprecedented rise in urbanization & industrialization, and growth in the population of the world, demand for energy is also linearly increasing.

Every year we get more energy from the Sun than all energy resources available on Earth combined. For example, total energy from oil reserves is estimated to be 240 TWy and we get 23,000 TWy every year from the Sun (**Figure 1-2**).[17] Hence, solar energy is free, cheap, and abundantly available for use.

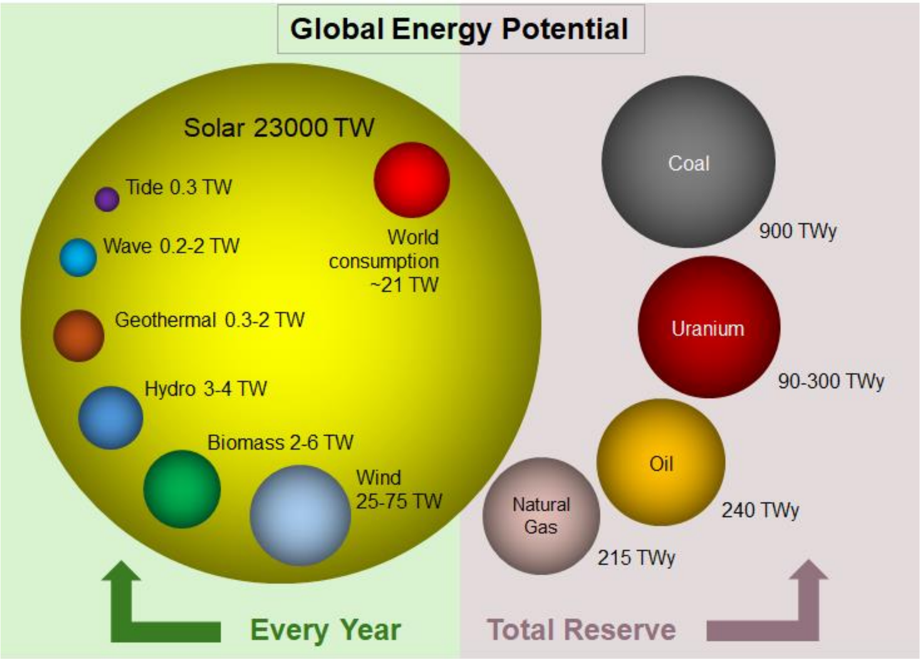

Figure 1-2. Global energy potential of different renewable and non-renewable resources. Note that the reserves for renewable energy resources are available every year while from conventional resources they are available as total.[17]

1.4.1 Development of solar cells

A solar cell is a device that converts sunlight into electrical energy. The origins of this technology trace back to 1839, when Alexandre-Edmond Becquerel first discovered the photovoltaic effect—a phenomenon where light exposure generates voltage or electric current. He observed this effect in an electrochemical cell under illumination, marking the first step toward harnessing solar energy.[18]

In 1876, W. G. Adams and R. E. Day advanced the understanding of photovoltaic principles by observing the same effect in a solid-state selenium device. This discovery laid the groundwork for further exploration into photovoltaic technology.

The potential of solar energy conversion was realized in 1883, when C. E. Fritts developed a “photocell” capable of converting solar radiation into electrical energy. The theoretical understanding of this process was established in 1905 by Albert Einstein, who explained that light is composed of discrete packets of energy, called photons. These photons can eject electrons from a material if their energy exceeds the material’s work function. This explanation of photoelectric effect earned Einstein the 1921 Nobel Prize in Physics. Despite this breakthrough, early devices, including semiconductor metal junction solar cells developed in the late 1920s and early 1930s, demonstrated power conversion efficiencies (PCE) of less than 1%. PCE measures a solar cell’s power output relative to the power input from sunlight.

A breakthrough came in the 1950s with the development of the first silicon-based solar cells, which achieved an efficiency of 6%. This marked the beginning of the modern solar cell industry, as silicon-based devices offered higher efficiencies and practical applications. Today, silicon solar cells have surpassed 27% efficiency and dominate the commercial market. **Figure 1-3** shows the efficiency of different solar cells including Si which is represented by blue color code. This chart is maintained by National Renewable Energy Laboratory (NREL), United States.

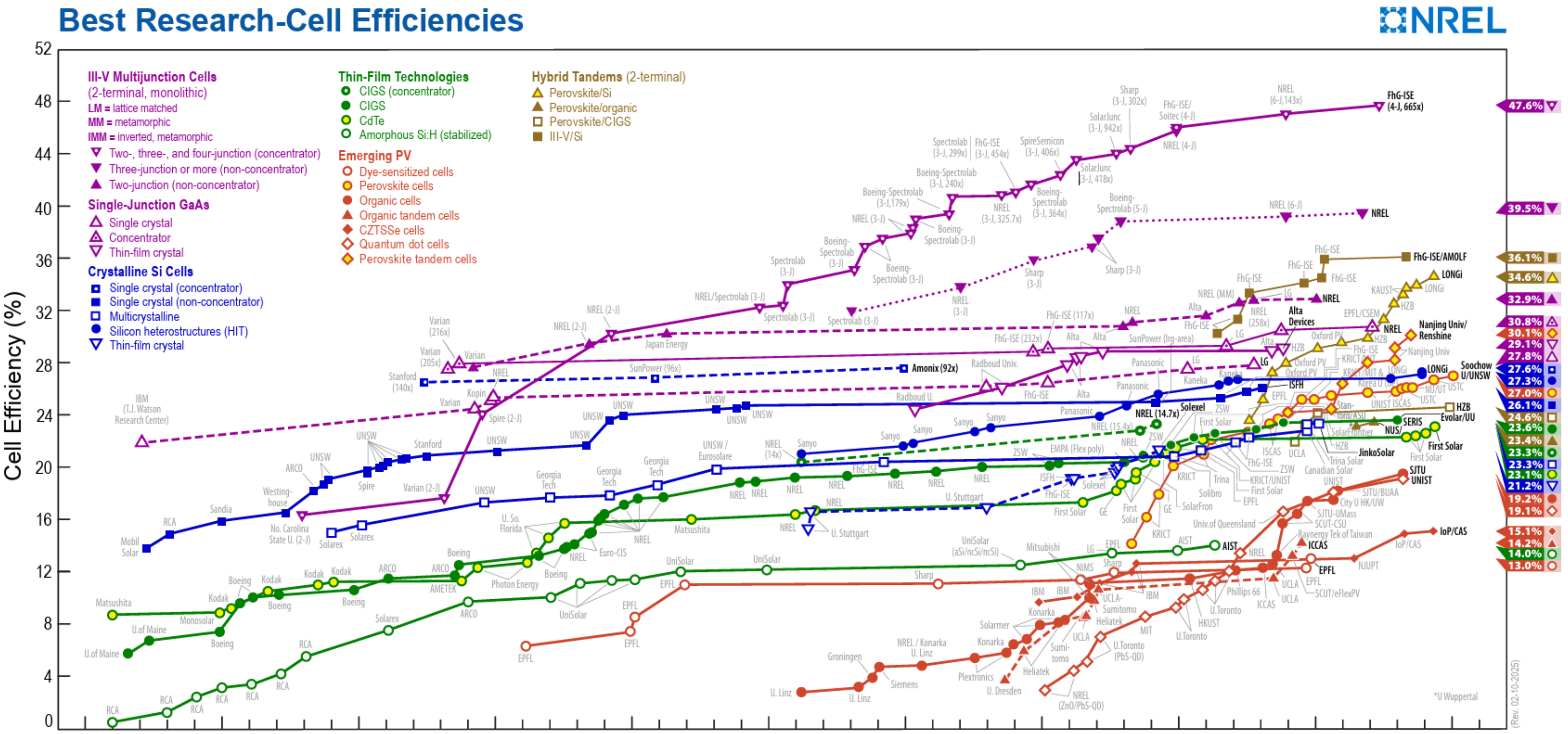

Figure 1-3. The highest confirmed power conversion efficiencies of research solar cells for a range of photovoltaic technologies, plotted from 1976 to present. This plot is courtesy of the National Renewable Energy Laboratory, Golden, CO.[19]

In 2009, another significant milestone was achieved with the development of the first perovskite solar cells (PSCs). These devices, based on perovskite-structured materials, have seen rapid advancements, with their efficiencies now 27% (**Figure 1-3**).[19] Gallium Arsenide (GaAs) solar cells are although high performing but extremely costly that they are only limited to space applications. Then, there are silicon solar cells being the industry champion thus far. Despite having relatively acceptable device performance, silicon solar cell manufacturing process is complicated and less energy efficient.

1.5 Perovskite structure

Perovskite is named after a Russian mineralogist Lev Perovski (1792-1856). Any material that has the same crystal structure as that of mineral calcium titanium oxide ($CaTiO_3$) with ABX_3 chemical formula is called perovskite.[20,21]

Halide perovskites have a cubic cell structure and general formula of ABX_3 (**Figure 1-4**), where A-site is generally a monovalent cation such as methylammonium ($CH_3NH_3^+$), formamidinium ($HC(NH_2)_2^+$) and Cs^+ which is surrounded by an octahedral cage of $[PbX_6]^{4-}$, B-site has a bivalent metal cation such as Pb^{2+}, Sn^{2+} and X is the halogen anion like Cl^-, I^-, Br^-.[3] In perovskite structure BX_6 octahedra is formed by B and X with B (metal cation) in the center and X (halogen anions) in the corner and upon extension of BX_6 octahedra a three-dimensional structure is formed.[22–26] Organic/inorganic metal lead halide compounds such as methylammonium lead iodide ($MAPbI_3$), formamdinium lead iodide ($FAPbI_3$), and cesium lead iodide ($CsPbI_3$) are some of the specific examples of perovskite semiconductor which hold particular interest because of their excellent optoelectronic properties.[27–29] This structure is adopted for various complex compounds. This thesis will mainly focus on the heavy metal containing perovskite such as lead (Pb).

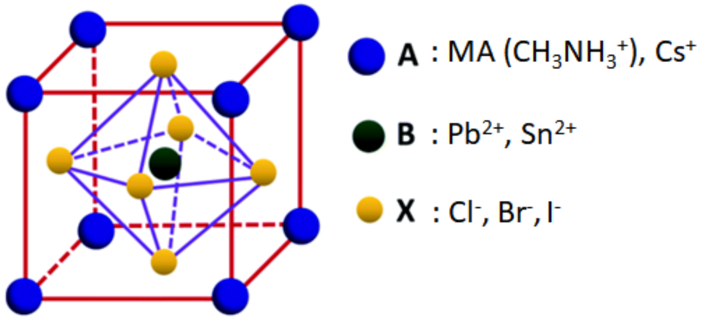

Figure 1-4. Crystal structure of metal halide perovskites. Following ABX_3 chemical formula, it has organic or inorganic A-site cations such as $CH_3NH_3^+$ on its corners, metals such as Pb in the center and halide anions such as I^- on the face of cubic structure.

1.6 Advantages of halide perovskites

There are certain advantages of perovskite materials for an application in optoelectronic devices, particularly solar cells which are discussed below:

1) **Solution processability**

PSCs have emerged as a highly promising photovoltaic technology, largely due to their solution processability, which simplifies fabrication and significantly reduces production costs.[30,31] The process begins with the preparation of a perovskite ink, typically composed of lead halides (e.g., PbI_2 or $PbBr_2$) and A-site organic cations (e.g., methylammonium iodide (MAI, CH_3NH_3I) or formamidinium iodide (FAI, $HC(NH_2)_2I$)) dissolved in polar solvents such as dimethylformamide (DMF) or dimethyl sulfoxide (DMSO).

The choice of solvents and precursors is critical, as they influence the crystallization kinetics, film morphology, and overall performance of the perovskite solar cell.

A few microliters of this ink are deposited onto a clean substrate, such as glass coated with indium doped tin oxide (ITO) or flexible polymer substrates and then spin-coated to ensure uniform spreading and controlled thickness of the perovskite layer. Spin-coating is a simple and cost-effective technique that allows precise control over film formation. Following deposition, the substrate is annealed on a hotplate at moderate temperatures (typically 100–150 °C) to evaporate the solvents and induce crystallization, resulting in a high-quality perovskite thin film with excellent optoelectronic properties.

This low-temperature processing is a significant advantage, as it enables the use of flexible and lightweight substrates, such as polymers, which are incompatible with high-temperature processing. Additionally, the low energy consumption and scalability of this process make perovskites highly attractive for large-scale manufacturing and integration into next-generation photovoltaic devices. Some of the reported solution processed deposition methods are shown in **Figure 1-5**.[32]

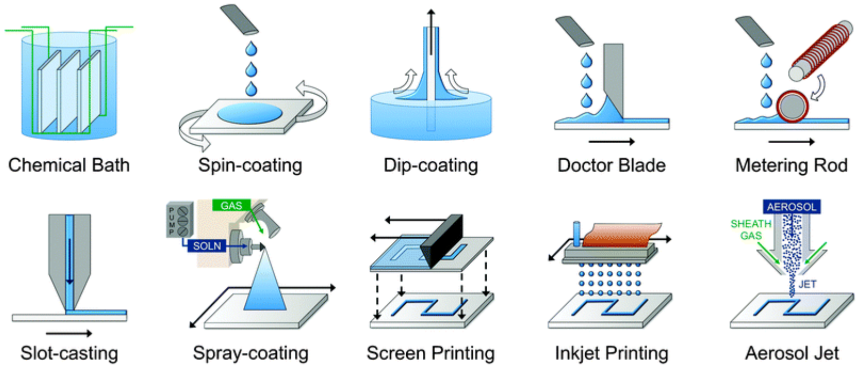

Figure 1-5. Schematic describing various solution processing methods. Reprinted with permission from ref.[32] Copyright 2011 Royal Society of Chemistry.

In stark contrast, the fabrication of silicon solar cells involves energy-intensive processes.[33,34] The production of silicon wafers begins with the growth of a silicon ingot using the Czochralski process, which requires temperatures exceeding 1500 °C.[35,36] The silicon ingot is then sliced into thin wafers using advanced cutting technologies, such as diamond wire sawing, a process that generates significant material waste.[37,38] The high-temperature processing of silicon not only increases production costs but also limits the choice of substrates to rigid materials, such as glass or crystalline silicon. Furthermore, the fabrication of silicon solar cells involves multiple steps, including diffusion doping, anti-reflection coating deposition, and metallization, all of which require specialized equipment and high energy input.[39–41] These factors contribute to the high cost of silicon solar cell production. A schematic diagram of the Si solar cell fabrication steps is shown in **Figure 1-6**.

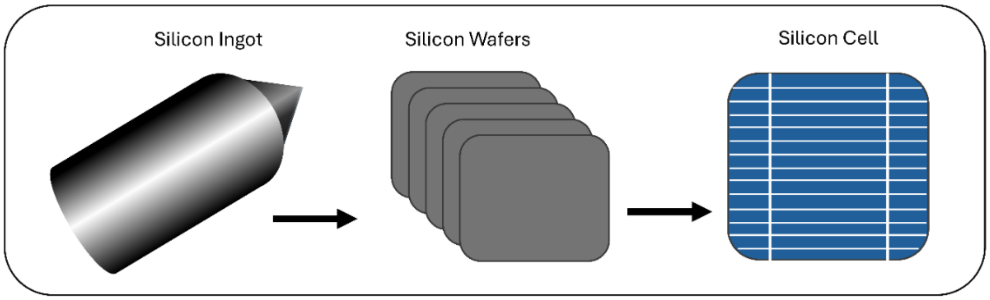

Figure 1-6. Schematic describing how silicon solar cells are made from silicon ingots.

The solution processability of PSCs is a game-changing feature that sets them apart from traditional silicon solar cells (a complete PSC life cycle from ink preparation to fabrication and its application is shown in **Figure 1-7**).[42] The ability to fabricate high-quality perovskite films at low temperatures using simple and scalable techniques makes perovskites a promising candidate for next-generation photovoltaics.[43–46]

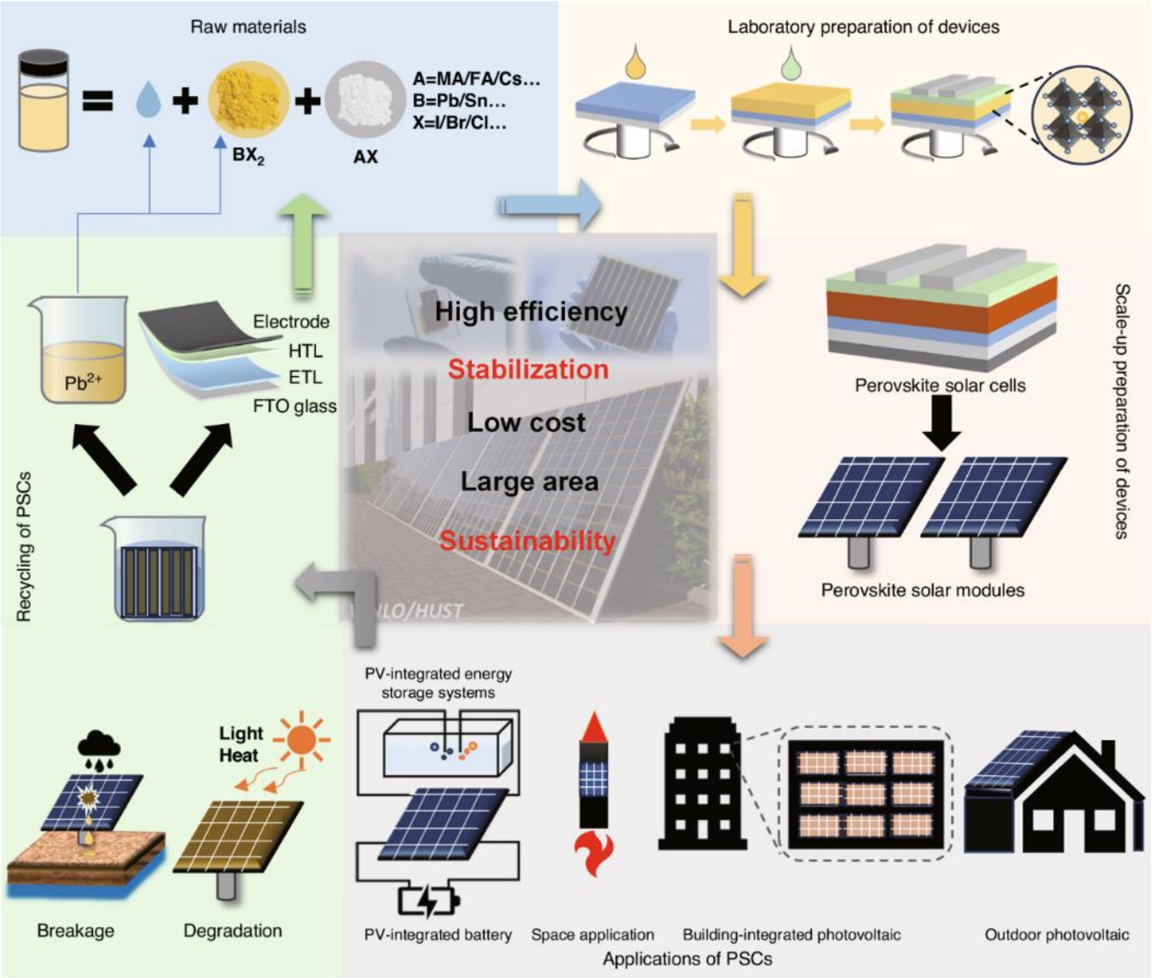

Figure 1-7. The life cycle of perovskite materials. Reproduced from ref.[42], used under Creative Commons CC-BY license 4.0.

While challenges such as stability and scalability remain, ongoing research aims to address these issues and unlock the full potential of PSCs for sustainable and cost-effective energy production.[47–50] The combination of low fabrication costs, compatibility with flexible substrates, and high efficiency positions PSCs as a transformative technology in the renewable energy landscape.

2) Bandgap tunability

Bandgap tunability in semiconductors is a critical property that enables their application in a wide range of optoelectronic devices, including light-emitting diodes (LEDs) and tandem solar cells (**Figure 1-8**).[51] In perovskite materials, bandgap tunability can be achieved through three primary mechanisms:

i. Elemental composition,

ii. Crystal structure modification.

These mechanisms allow the bandgap of perovskites to be finely tuned across nearly the entire visible spectrum, making them highly versatile for optoelectronic applications.

For solar cells, this tunability is particularly advantageous in the design of tandem solar cells, which consist of two or more sub-cells with different bandgaps. By combining a wide-bandgap sub-cell with a narrow-bandgap sub-cell, tandem solar cells minimize thermalization losses and maximize the utilization of the solar spectrum. This approach has led to significant advancements in photovoltaic efficiency.[52–56]

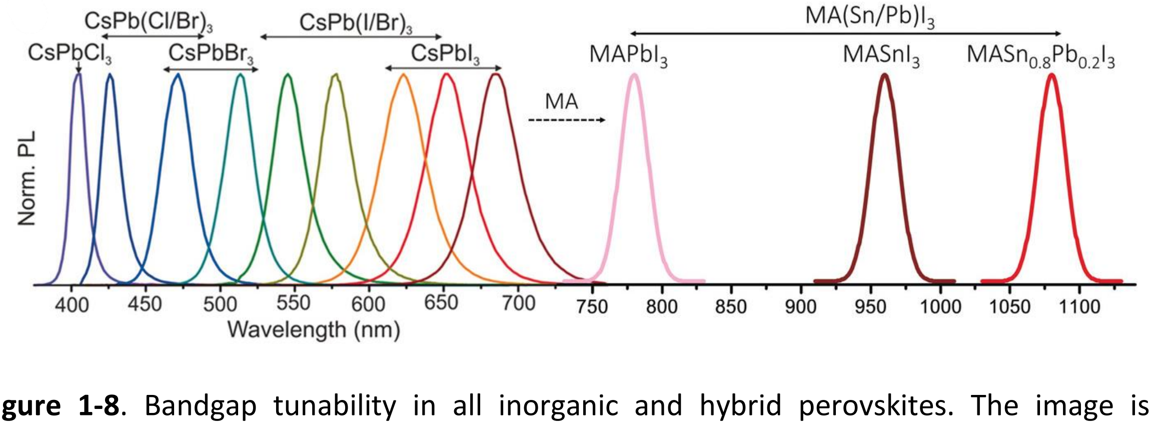

Figure 1-8. Bandgap tunability in all inorganic and hybrid perovskites. The image is reprinted from ref.[51] with permission from Wiley, copyright 2018.

Currently, perovskite–Si, perovskite–copper indium gallium selenide (CIGS), and perovskite–perovskite tandem solar cells have garnered considerable attention.[57–60] Among these, perovskite–Si tandem solar cells have achieved remarkable efficiencies exceeding 33%, showcasing their potential for next-generation photovoltaics.[61] Additionally, the solution processability of perovskite–perovskite tandem solar cells offer a pathway for the fabrication of low-cost, high-efficiency, and flexible solar cells, further enhancing their appeal for commercial applications.

3) Photophysics

A photoactive layer, perovskite in our case, essentially performs the following three functions.

i. Efficiently absorbs sunlight,
ii. Creates and separates electron (e^-) and hole (h^+) pairs, and
iii. Efficiently transports the carriers to charge selective layers.

Firstly, perovskite offers high optical absorption coefficient which is the intrinsic property of a material.[62,63] Being a direct bandgap material, the absorption coefficient of perovskites is much higher than that of an indirect material such as Si (**Figure 1-9**). It means that same amount of light can be captured in a much thinner perovskite photoactive layer (0.5-1 μm) than a much thicker silicon material (100-500 μm).[64,65]

The exciton binding energy of perovskite materials is a critical parameter that determines the energy required to separate electron-hole (e^--h^+) pairs (excitons) into free charge carriers. For efficient photovoltaic operation, it is essential to have a low exciton binding energy, as this facilitates the dissociation of excitons into free carriers upon light absorption, enabling their collection at the charge-selective contacts.

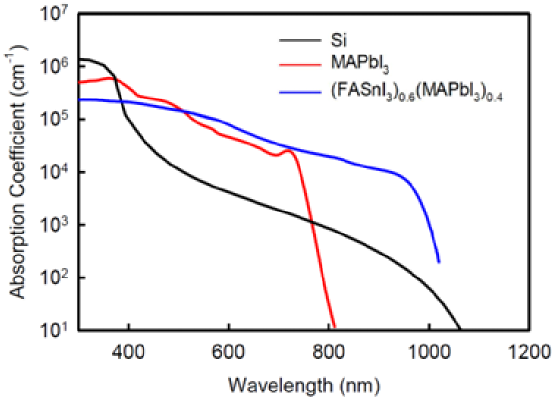

Figure 1-9. Absorption coefficients of silicon and perovskites. It shows that the absorption coefficient of perovskite materials is higher than the Si. Reprinted from ref.[66] with permission from American Chemical Society, copyright 2022.

In perovskite materials, the exciton binding energy is remarkably low, typically ranging between ~15–40 meV.[67] This value is comparable to the thermal energy at room temperature ($k_BT \approx 25.7$ meV), where k_B is the Boltzmann constant (8.617×10^{-5} eV/K) and T is the temperature in Kelvin (298 K). Such a low binding energy ensures that excitons can be easily dissociated into free carriers even at ambient conditions, contributing to the high performance of perovskite solar cells.

Perovskite semiconductors exhibit a remarkable characteristic known as defect tolerance, which contributes to their exceptionally long charge carrier lifetimes.[68] A long carrier lifetime indicates a low density of defects capable of trapping charge carriers, as trapped carriers cannot be extracted at the charge-selective layers and instead contribute to non-radiative recombination, reducing device efficiency. This defect tolerance is particularly unusual for materials fabricated at relatively low temperatures (~150 °C), unlike traditional semiconductors such as Si, which require extremely high processing temperatures to achieve their desired thermodynamic state. Interestingly, despite being solution-processed at low temperatures, perovskites exhibit a total trap density comparable to that of traditional semiconductors, raising the question of then what makes perovskites defect-tolerant?

The defect tolerance of perovskites can be attributed to the nature and energy levels of their trap states (**Figure 1-10**). In defect-intolerant materials like gallium arsenide (GaAs) and cadmium telluride (CdTe), deep trap states within the bandgap create a significant energy difference between the trap states and the conduction or valence bands. Once charge carriers are trapped in these deep states, they cannot easily return to the transport bands because the energy difference is much larger than the available thermal energy (k_BT). As a result, trapped carriers are lost to non-radiative recombination, significantly reducing carrier lifetime and device performance. In contrast, perovskite materials have trap states that are either within the transport bands or very close to them, known as shallow trap states. The energy difference between these trap states and the transport bands is small, often comparable to or less than the thermal energy (k_BT). This allows trapped charge carriers to easily thermalize back into the transport bands without losing their energy to non-radiative mechanisms. As a result, even if defects are present, they do not significantly degrade the carrier lifetime or device performance.

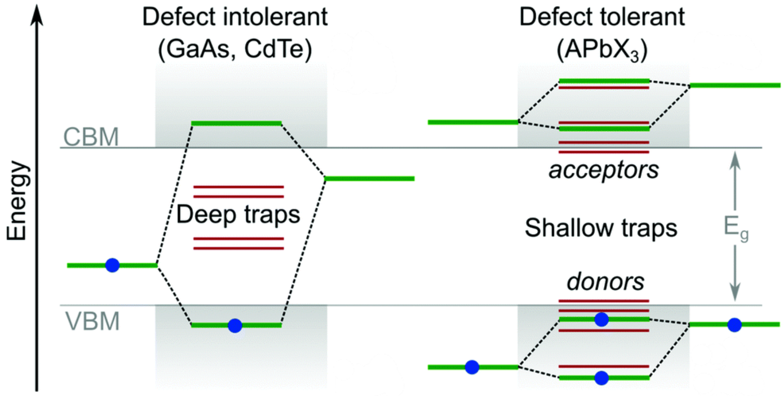

Figure 1-10. Energy level diagram of traditional semiconductor materials, GaAs and CdTe, and the location of deep traps versus shallow traps in perovskite semiconductors. The image is reprinted from ref.[68] , licensed under Creative Commons Attribution-NonCommercial 3.0.

Traditional semiconductors like Si and GaAs require high-temperature processing to achieve a low density of deep traps, as deep trap states within the bandgap lead to significant non-radiative recombination, reducing carrier lifetime and device efficiency. In contrast, perovskite semiconductors can be fabricated at low temperatures (~150 °C) while maintaining low trap densities. The shallow trap states and benign defects in perovskites enable long carrier lifetimes and high device performance, even in the presence of defects. This defect tolerance is a key factor behind the high PCEs and long carrier diffusion lengths observed in perovskite solar cells, which are critical for efficient charge extraction. Additionally, this property makes perovskites suitable for low-cost, solution-processed fabrication, as they do not require the high-temperature annealing or ultra-pure conditions needed for traditional semiconductors.

In addition to the above advantages, perovskite materials exhibit the following properties as well which set them apart from their counterparts:

i. Devices based on perovskite materials are low cost and have easy fabrication process e.g., roll-to-roll fabrication of flexible devices.[69]
ii. These materials exhibit modest mobility of photogenerated carriers. The mobility of electrons is reported to be 5-10 $cm^2V^{-1}s^{-1}$ and that of hole is 1-5 $cm^2V^{-1}s^{-1}$.[70]
iii. These materials also show long diffusion lengths (> 3 μm) of charge carriers that enable them for use in high-performance optoelectronic devices.[71,72]

1.7 Efficiency limit of solar cells

Single-junction solar cells face fundamental limitations in converting 100% sunlight into electricity, with their maximum theoretical efficiency constrained by inherent physical processes. The widely recognized Shockley-Queisser (S-Q) limit, established in 1961,[73] sets an efficiency limit of ~33**%** for an ideal solar cell under standard test conditions (AM1.5 spectrum, 1 sun illumination). This model considers only radiative recombination as the primary loss mechanism and identifies an optimal bandgap range of 1.1–1.3 eV for maximizing photovoltaic conversion.

However, additional non-radiative loss mechanisms further reduce this limit. In 1984, Tiedje *et al.* refined the S-Q model by considering:[74]

1. Free-carrier absorption (absorption of photons by charge carriers)
2. Auger recombination (non-radiative energy loss via carrier-carrier scattering)

Their calculations revealed a lower efficiency limit of 29.8%, demonstrating that practical single-junction solar cells cannot reach the idealized S-Q threshold due to these unavoidable losses. It is also important to note that Auger recombination is generally significant in Si semiconductors, but not typically dominant in most other semiconductors. **Figure 1-11** illustrates this revised limit, highlighting the efficiency-thickness relationship while accounting for all three recombination pathways.

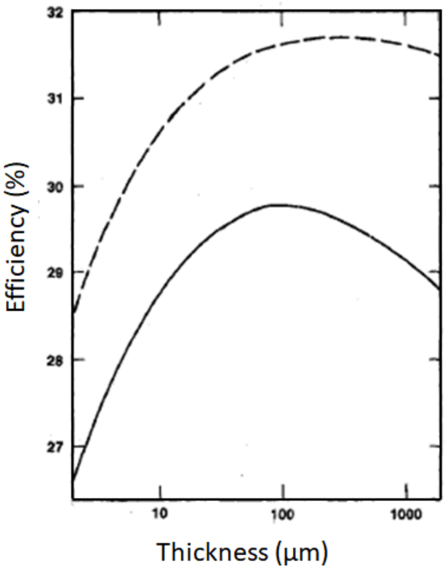

Figure 1-11. Efficiency of silicon solar cells as a function of thickness for textured cells with back reflectors. The top curve includes only radiative recombination, and the bottom curve includes Auger recombination and free carrier absorption in addition to radiative recombination. Reprinted with permission from ref.[74] IEEE, copyright 1984.

1.8 Architecture of perovskite solar cells

A perovskite solar cell mainly consists of a photoactive layer (perovskite in this case) which is sandwiched between an electron transport layer (ETL) and a hole transport layer (HTL) with metal electrodes on bottom, such as ITO, and a top electrode, such as gold (Au).

Therefore, the architecture of a perovskite solar cell is divided into two categories, i.e. negative-intrinsic-positive (*n*-*i*-*p*) structure and positive-intrinsic-negative (*p*-*i*-*n*) device structures as shown in **Figure 1-12**.[75]

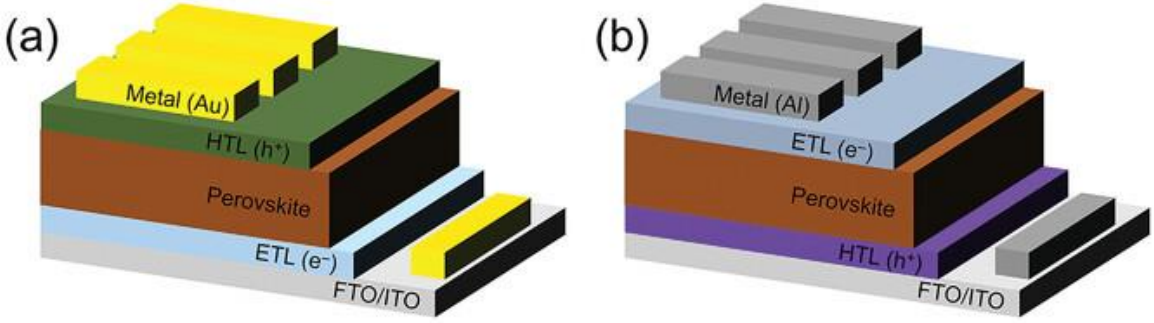

Figure 1-12. Two device structures of perovskite solar cells. (a) negative-intrinsic-positive (*n*-*i*-*p*) structure, (b) positive-intrinsic-negative (*p*-*i*-*n*, also called inverted structure) for fabrication of perovskite solar cells. The image is reproduced from ref.[75] under Creative Commons CC-BY license 4.0.

In a *n*-*i*-*p* device structure, ETL is coated on top of ITO followed by coating perovskite and HTL, whereas the structure is inverted in *p*-*i*-*n* devices where HTL is deposited first on top of ITO followed by deposition of perovskite and ETL and top metal electrodes.

1.8.1 Choice of perovskite composition

In 2009, when Kojima et al. reported PSCs for the first time, their efficiency was just about 3.8% and they used $MAPbI_3$ perovskite composition.[76] However, the performance of $MAPbI_3$ is fundamentally limited by its slightly wider bandgap (~1.55 eV) which cannot absorb most of the solar spectrum because of it being far from the ideal bandgap (S-Q limit). Secondly, it is unstable due to intrinsic hygroscopic and volatile nature of MA^+ cation which irreversibly goes into degradation and phase transition in ambient conditions.[77] Therefore, efforts were made to stabilize its photoactive phase, and Graetzel *et al.* reported the double A-site cation, a mixture of MA^+ and FA^+, to stabilize the photoactive phase of perovskite.[78] This advancement led to achieve the PCE of 25.7% in 2022 when I was in the early stages of my research program, and which is why it was the choice for my research in chapter 2 and chapter 3.Despite achieving relatively high PCEs, the stability of the mixed A-site cation was still a challenge, mostly because of volatility of MA^+. Therefore, the scientific community turned attention to pure $FAPbI_3$ perovskite solar cells. $FAPbI_3$ exhibits several advantages over pure $MAPbI_3$ and mixed A-site cation formulation. They are thermally stable at elevated temperatures, and more importantly, their bandgap (1.48 eV) is more closer to the S-Q limit (**Figure 1-13**).[79,80] Nonetheless, because of relatively large FA^+ size, their tolerance factor increases to >1 which results in hexagonal delta-phase of the $FAPbI_3$ films at room temperature. A tolerance factor (t) is a geometric parameter used to predict if a compound with ABX_3 formula can form a stable perovskite crystal structure. It is calculated using the equation:

$$t = \frac{r_A + r_x}{\sqrt{2}(r_B + r_x)}$$

where r_A, r_B and r_x represent ionic radii of A-site cation, B-site cation and X-site anions (halide), respectively. Furthermore, many important works have been done to stabilize the **α** -$FAPbI_3$ such as incorporating Cd into the precursor solution.[81–83]

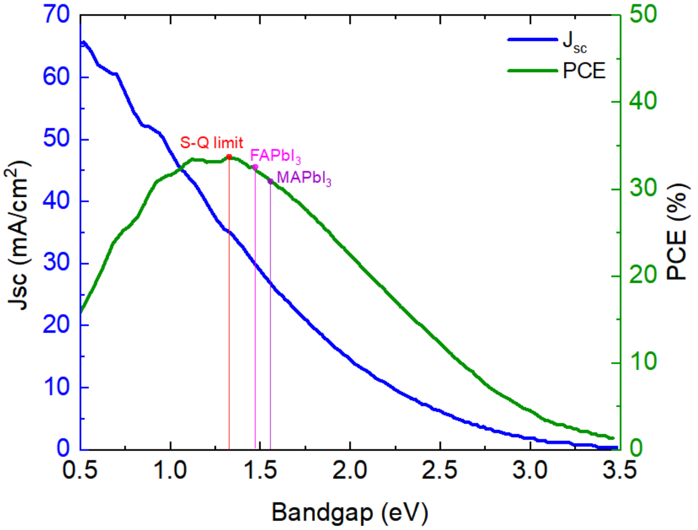

Figure 1-13. The theoretical PCEs and short-circuit current density (J_{SC}) of PSCs as a function of the bandgap. Reproduced from ref.[79] The data was extracted using WebPlotDigitizer [(Copyright 2010-2019 Ankit Rohatgi, https://automeris.io/WebPlotDigitizer)].

1.8.2 Charge transporting layers

In the fabrication of a PSC, the photoactive layer (perovskite) is sandwiched between two critical functional layers (**Figure 1-14**): the ETL and the HTL. As their names suggest, ETL is responsible for collecting and transporting electrons to the cathode, while HTL collects and transports holes to the anode. These charge transport layers (CTLs) layers play a vital role in ensuring efficient charge extraction and minimizing recombination losses, which are essential for achieving high-performance PSCs. The energy band diagram for a *n-i-p* perovskite solar cells is shown in **Figure 1-15**.[84]

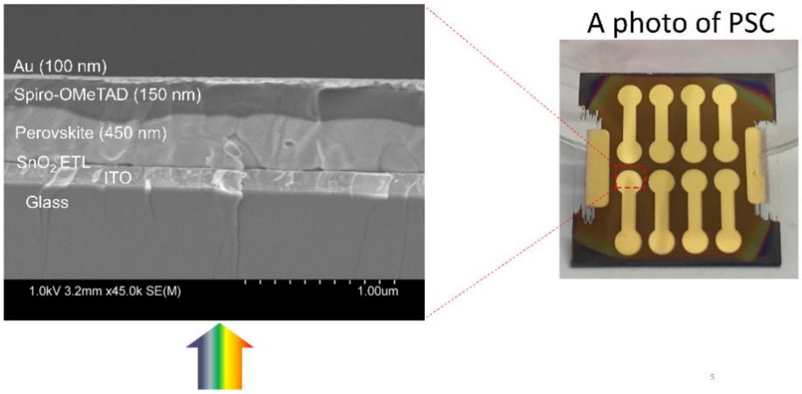

Figure 1-14. Perovskite solar cell is a stack of 5-8 different layers. On the right, it shows an image of perovskite solar cell and its corresponding cross-sectional SEM image on the left.

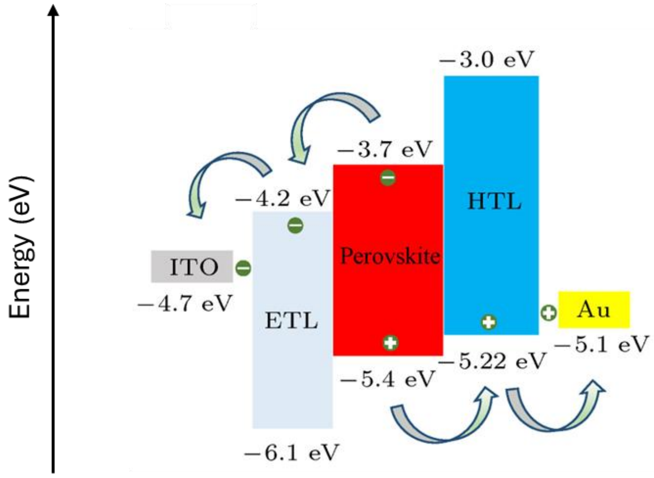

Figure 1-15. Energy band diagram of perovskite solar cell showing the transfer of charges to their respective transport layers. The image is reproduced from ref.[84]

1) Hole transport layer (HTL)

HTLs play a critical role in PSCs by ensuring efficient hole extraction to the electrode. Over time, various HTL materials have been investigated to enhance device performance and stability. In the conventional *n-i-p* architecture, 2,2′,7,7′-tetrakis[N,N-di(4-methoxyphenyl)amino]-9,9′-spirobifluorene (Spiro-OMeTAD) has been widely employed.

However, Spiro-OMeTAD suffers from a critical limitation: poor thermal stability at elevated temperatures. This leads to degradation of the HTL over time, adversely affecting both performance and device stability.[85] To overcome this challenge, ongoing research is focused on developing alternative HTL materials such as polymeric materials like poly[bis(4-phenyl)(2,4,6-trimethylphenyl)amine] (PTAA).[86]

Meanwhile, in the *p-i-n* configuration, alternative HTLs, and self-assembled monolayers (SAMs) including [2-(9H-carbazol-9-yl)ethyl]phosphonic acid (2PACz) and [2-(3,6-dimethoxy-9H-carbazol-9-yl)ethyl]phosphonic acid (MeO-2PACz), have shown promising results.[87,88]

Notably, HTLs such as PTAA and 2PACz have enabled PSCs to withstand harsh environmental conditions, successfully passing damp-heat tests for 1000 hours at 85 °C and 85% relative humidity (RH). Furthermore, devices using MeO-2PACz as the HTL have demonstrated remarkable stability, enduring 3,000 hours of temperature cycling between −60 and 80 °C.

Beyond these materials, a range of other organic HTLs—including small molecules containing diphenylamine and triphenylamine moieties—and conducting polymers such as poly(3,4-ethylenedioxythiophene): polystyrenesulfonate (PEDOT:PSS) and poly(N,N′-bis(4-butylphenyl)-N,N′-bis(phenyl)benzidine)—have been explored. Inorganic HTLs like nickel oxide (NiO_x) and copper thiocyanate (CuSCN) have also enabled PSCs to achieve PCEs exceeding 20%.

2) Electron transport layer (ETL)

In a PSC, a transparent ETL is deposited to facilitate the transportation of electrons to the electrode. ETL materials such as titanium oxide (TiO_2), zinc oxide (ZnO) and tin oxide (SnO_2) have been explored for their use as an ETL material. However, materials like TiO_2 are, although, transparent but their electron mobility (0.1- $4\ cm^2\ V^{-1}\ s^{-1}$) is less than perovskite.[89] Materials having electron mobility less than the perovskite means that they cannot transport the electrons to the electrodes efficiently and resulting in accumulation of electrons at the ETL/perovskite interface. This accumulation is detrimental for device efficiency and stability. Furthermore, TiO_2 also requires high annealing temperature which limits its application for development of flexible perovskite solar cells.

SnO_2 is currently the most widely used material for the ETL in PSCs. Its popularity is due to several advantageous properties:[89–91]

i. Wide bandgap: SnO_2's wide bandgap allows most of the incident light to pass through and be absorbed by the perovskite layer, maximizing light utilization.
ii. Low temperature processability: SnO_2 can be deposited at relatively low temperatures, making it compatible with flexible substrates and low-cost fabrication methods.

For optimal device performance, it is crucial to deposit SnO_2 as a smooth, dense, and uniform film. Any irregularities in the ETL can lead to poor charge extraction and increased recombination losses, significantly reducing the efficiency of the PSC.

The importance of SnO_2 and its impact on device performance are discussed in detail in Chapter 4 of this thesis.

1.8.3 Electrodes in perovskite solar cells

Perovskite solar cells require efficient charge extraction through both top and bottom electrodes, which also serve as electrical contacts to external circuits. These electrodes are typically fabricated from metals like gold (Au), silver (Ag), or copper (Cu), carbon-based materials, or transparent conducting oxides (TCOs) such as ITO and fluorine-doped tin oxide (FTO). The selection of electrode material significantly impacts device performance, stability, and processing compatibility, making it critical design consideration.

TCOs are particularly favored as front contacts in perovskite devices, due to their unique combination of high optical transparency and electrical conductivity. These properties minimize parasitic light absorption while ensuring efficient charge collection, which is essential for maintaining high device efficiency. Among TCOs, ITO is widely used because of its exceptional transparency (>90% in the visible spectrum) and low sheet resistance (<3 Ω/sq), outperforming FTO, which exhibits slightly lower transparency (80-90%) and higher sheet resistance (7-20 Ω/sq). Additionally, ITO's smoother surface morphology is advantageous for the subsequent deposition of high-quality perovskite films, as reduced roughness helps minimize defect formation and charge recombination.[92]

For the counter electrodes to the TCO, metal or carbon electrodes are deposited which constitutes the final step of device fabrication process. These metal electrodes are thermally deposited on the top of device. However, carbon electrodes have also been recently used and studied which serve as a cheaper alternative to the complex and expensive thermal deposition process. Nevertheless, the efficiency of carbon electrode-based devices still lags to those of conventional metal electrodes due to its low conductivity in n-i-p devices.

In this thesis, *n-i-p* device structure with ITO and gold electrodes are used unless otherwise specified. The reason behind choosing *n-i-p* device structure lies in better energy level alignment of ETL (such as SnO_2) with perovskite, and its promise for fabrication in the ambient air. In the *p-i-n* structure, HTL materials such as SAMs are highly sensitive to ambient air, thus, limiting the prospects for fabrication in ambient air.

1.9 Performance parameters of perovskite solar cells

Current-voltage *(JV)* is an important characterization method through which PCE or simply efficiency is determined. The *JV* curve is a relationship between voltage applied to an electronic device and current flowing through it. This curve is obtained by applying a range of voltage across the device and at each voltage the current flowing through device is measured. A typical measurement setup is shown in **Figure 1-16**.

Through this *JV* curve key performance parameters such as the short-circuit current density (J_{SC}) and open-circuit voltage (V_{OC}) are derived. When the device is held at zero voltage (short-circuit condition), the photogenerated current reaches its maximum value, defined as J_{SC}. This parameter is measured using an ammeter connected in series with the cell and is fundamentally governed by the material's ability to absorb sunlight and generate charge carriers. Due to the exceptionally high absorption coefficient of perovskite materials, J_{SC} values in these devices remain notably high. Importantly, J_{SC} exhibits an inverse relationship with the bandgap (E_g) of the photoactive layer—narrower bandgaps enable absorption over a broader range of the solar spectrum, thereby yielding higher photocurrents.

Figure 1-16. Newport Oriel sol-3A solar simulator, a source meter for providing electrical bias and a sample holder. (Picture was taken at Saidaminov Lab, University of Victoria).

Conversely, under open-circuit conditions (zero current), the device develops its maximum voltage, termed V_{OC}, which is measured using a voltmeter connected in parallel. In principle, V_{OC} is directly proportional to the bandgap of the absorber material; a larger bandgap should theoretically result in a higher V_{OC} due to the increased energy difference between the quasi-Fermi levels of electrons and holes. However, this does not necessarily translate to higher device efficiency, as widening the bandgap also reduces the spectral range of sunlight absorption, leading to a decline in J_{SC}. Thus, optimizing efficiency requires balancing these competing trends between V_{OC} and J_{SC}.

In practice, the experimentally observed V_{OC} is always lower than the theoretical maximum due to various loss mechanisms, including non-radiative recombination, shunt resistance losses, and interfacial band misalignment with CTLs. These factors collectively limit the achievable voltage, emphasizing the importance of defect passivation and interface engineering in perovskite solar cell development.

As discussed above, V_{OC} and J_{SC} represent the maximum voltage and current a solar cell can generate under no-load and short-circuit conditions respectively, however, there are another two important parameters as well, i.e. voltage at maximum power point (V_{MPP}) and current density at maximum power point (J_{MPP}) which denote the actual operating voltage and current respectively at which the cell delivers its maximum power output. These operating points are lower than their maxima due to internal resistances and real-world operating conditions. The maximum power (P_{max}) is calculated as the product of V_{MPP} and J_{MPP}, and this value directly determines the PCE of the solar cell when compared to the incident solar energy.

V_{MPP} and J_{MPP} are directly involved in calculating the fill factor (FF) of a solar cell, which refers to the ''squareness'' of the *JV* curve. It is derived from the ratio of product of V_{MP} and J_{MP} (P_{max}) to the product of V_{OC} and J_{SC}, calculated by the equation below, and indicates how closely the cell's *JV* curve approaches the ideal rectangular shape:

$$FF = \frac{J_{MPP} \times V_{MPP}}{J_{SC} \times V_{OC}}$$

Together, these parameters—V_{MPP}, J_{MPP}, V_{OC}, and J_{SC}—are critical for obtaining the PCE of a solar cell (a typical *JV* curve is shown in **Figure 1-17**), which is determined by the following equation:

$$PCE = \frac{P_{out}}{P_{in}} = \frac{J_{SC} \times V_{OC} \times FF}{P_{in}}$$

Where P_{in} is the power input (incident light) and P_{out} is the electrical power output.

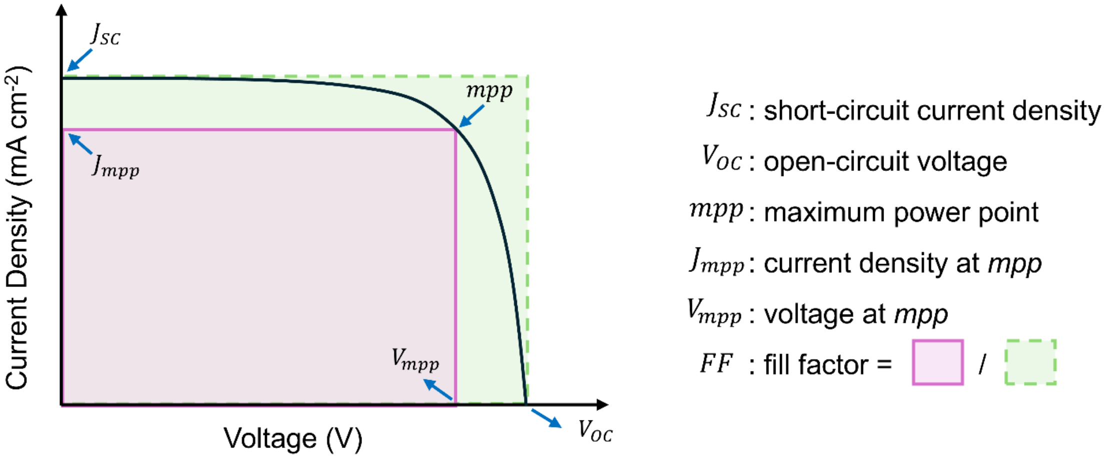

Figure 1-17. *JV* characteristics of a solar cell. The current at 0 V voltage is called short-circuit current (J_{SC}), and voltage at 0 A current is called open-circuit voltage (V_{OC}). The fill factor is the ratio between the maximum current and voltage product to the product of J_{SC} and V_{OC}.

Similarly, the operational stability of a solar cell is measured at its maximum power point tracking (MPPT). It is a condition where voltage and current of the device are maximum. For the standardization, the International Summit on Organic Photovoltaic Stability (ISOS-L-1I) protocols (light soaking intrinsic stability test) test is performed to evaluate the stability of the devices. In this test, an encapsulated device is stressed at MPPT until it reaches its T_{80} value (the time required for the efficiency to drop to 80% of its initial value).[70]

1.10 Pathway for improving device performance

Interface engineering: Perovskite solar cells (PSCs) have gained significant attention in recent years due to their outstanding optoelectronic properties and rapidly increasing PCEs.[93]

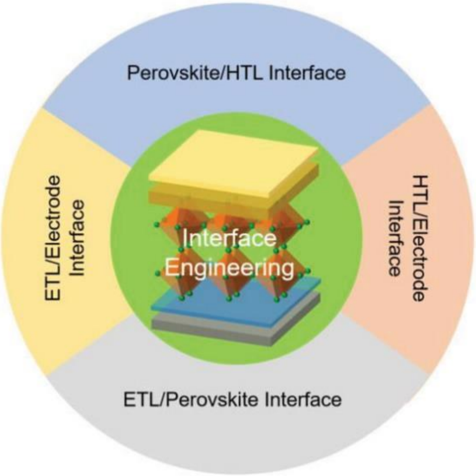

Figure 1-18. Schematic diagram illustrating different interfaces present in a stack of perovskite solar cells. The figure is adapted from ref.[93] with permission from Wiley, licensed under Creative Commons CC-BY-NC-ND.

However, challenges related to long-term operational stability and defect-induced non-radiative recombination remain critical barriers to commercialization. A major focus of recent research has been the stabilization of the perovskite crystal phase and the passivation of defects to suppress recombination losses. Since PSCs consist of multiple functional layers with several material interfaces, the role of interface engineering becomes paramount. Robust and well-optimized interfaces are essential for facilitating efficient charge transport and minimizing interfacial recombination losses. Interface engineering involves the application of tailored chemical or physical treatments at the interfaces to reduce trap states, align energy levels, and enhance interfacial contact quality, ultimately leading to improved device efficiency and stability.

1) Interfacial Charge Dynamics

The charge dynamics process existing in a PSC contains several important steps; photogenerated charges, i.e. electron-hole pair, transfer of charges, and their recombination (**Figure 1-19**). These all significantly impact the performance of PSCs, and an efficient charge extraction will improve the efficiency of PSCs.

Deep-level defect states tend to be present at the interfaces and may introduce carrier recombination causing adverse effects on the efficiency and loss in the V_{OC}. Therefore, low charge recombination at the interface is critical to reduce V_{OC} loss and ultimately improve the efficiency of PSCs.

2) Defect Passivation

Essentially, there are two major interfaces which significantly impact the overall device performance and stability. One is ETL/perovskite interface, and the other is perovskite/HTL interface. Generally, a thin layer of hydrophobic molecules is applied on a perovskite surface to passivate the defects and reduce the non-radiative recombination and increase the stability of the film in ambient conditions. Similarly, different inorganic salts such as potassium chloride (KCl) are applied on top of ETL to make better energy level alignment with the perovskite which results in better charge extraction and reduced V_{OC} deficit.

Therefore, making robust and passivated interfaces can lead to higher device performance and better stability. In this thesis, Chapter 3 deals with passivation of top interface (perovskite/HTL), and Chapter 4 deals with the interface engineering of bottom interface (ETL/perovskite).

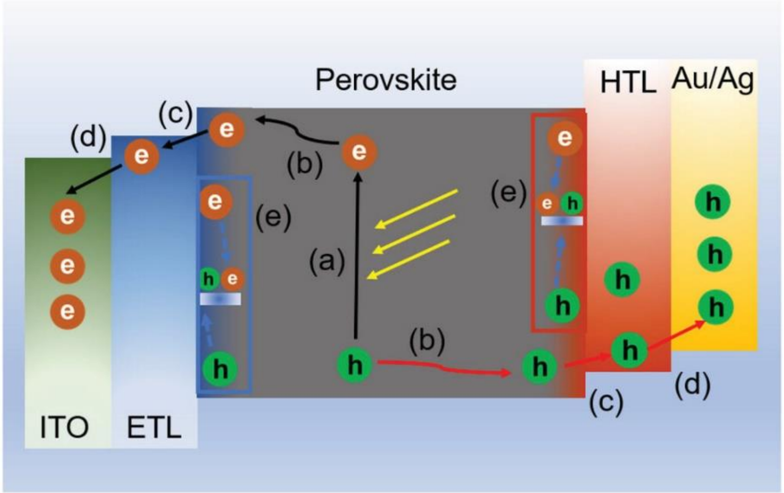

Figure 1-19. Charge transport diagram in a typical normal n-i-p perovskite solar cell: a) photogenerated excitons and dissociation, b) charge diffusion, c) charge extraction, d) charge transfer, and e) charge recombination induced by interface trap states. The image is adapted from ref.[93] with permission from Wiley, licensed under Creative Commons CC-BY-NC-ND.

1.11 Thesis goals

The main objective of this thesis is to first investigate the lab-scale manufacturing of perovskite solar cells in ambient air and then upscale them for commercialization, addressing both efficiency and stability.

The goal of 2nd chapter is to advance ambient-air fabrication of perovskite solar cells by developing stable compositional formulations of CsMAFA and MAFA (Cs: cesium; MA: methylammonium, $CH_3NH_3^+$; FA: formamidinium, $HC(NH_2)_2^+$) perovskites that overcome material degradation challenges, while establishing reliable processing protocols to achieve consistent efficiencies exceeding 20% under ambient conditions. A key focus involves creating robust encapsulation methods capable of sustaining stable operational stability test at maximum power point (MPP) for over 500 hours, supported by the development of an accelerated stability protocol using 120 °C thermal stress testing as a tool for predicting long-term stability test.

The goal of 3^{rd} chapter is to mitigate grain boundary-induced degradation in PSCs by developing targeted passivation strategies using biphenyl-based molecules. The work will focus on designing selective interfacial interactions where these moieties preferentially bind to PbI_2-rich defect sites on perovskite surface while preserving the perovskite crystal structure, with the dual objectives of extending radiative recombination lifetimes. A parallel goal involves leveraging the inherent hydrophobicity of aromatic systems to enhance moisture resistance by at least threefold compared to untreated films.

Chapter 4 aims to develop an optimized chemical bath deposition (CBD) process for uniform, conformal SnO_x electron transport layer that enables high-performance, scalable perovskite solar cells. The chapter will focus on controlling the reaction environment through $PbCl_2$ additive to regulate *pH* and prevent pre-mature precipitation of $Sn(OH)_2$. The work will establish fundamental principles for reaction control in CBD that bridge the gap between laboratory-scale achievements and commercial manufacturing requirements.

Chapter 2.

How To Make 20% Efficient Perovskite Solar Cells in Ambient Air and Encapsulate Them For 500 h Of Operational Stability

[Reproduced (adapted) with permission and alterations from: ‘’**Muhammad Awais**, Deepak T. G, Furui Tan, Makhsud I. Saidaminov. *How to make 20% efficient perovskite solar cells in ambient air and encapsulate them for 500 h of operational stability*. *Chemistry of Materials*. **2022**, 34, 18.“]

Contributions to research and writing

In this paper, I prepared all samples and developed methods for fabrication of solar cells, carried data collection and data analysis. I also wrote the first draft of the manuscript and led it through revision process until publication. The study was supervised by Dr. Makhsud I. Saidaminov.

Transition section

Fabrication of perovskite solar cells (PSCs) in ambient air is challenging because of humidity induced defects in the perovskite. In 2021, when I was in the early stages of my PhD research only a handful of reports would offer fabricating the PSCs in ambient air. Therefore, I chose to work on underlining comprehensive methods and protocols for fabricating reproducible, efficient and stable PSCs in ambient air. Therefore, this chapter of the thesis addresses these gaps by presenting a comprehensive, step-by-step methodology for fabricating 20%-efficient PSCs entirely in ambient air conditions, along with an encapsulation technique enabling stable MPP operation exceeding 500 hours. Significantly, a rapid encapsulation quality assessment protocol was introduced: devices that withstand after 5 minutes of 120°C thermal stress testing in ambient air will likely withstand long term MPP stability. These standardized procedures provide researchers with practical guidelines for ambient-air PSC development and reliable performance evaluation.

2.1 Introduction

Halide perovskites demonstrate strong light absorption and offer tunable bandgaps and long charge-carrier diffusion lengths,[65,76,94–107] making them one of the best photovoltaic materials. These properties have led them to unprecedented progress in photovoltaics. Perovskite solar cells (PSCs) can be fabricated at a low cost[108–116] and have recently surpassed a power conversion efficiency (PCE) of 25%, outshining other major thin-film photovoltaic technologies.[117,118]

A perovskite solar cell is a sandwich of at least five thin films, three of which are typically made from multi-component compositions. Fabrication conditions greatly affect the property of each component; therefore, despite the significant number of reports in this field, getting efficiency above 20% “psychological” barrier has been challenging. Saliba et al. reported a comprehensive, reproducible description of PSC fabrication protocols in 2018.[119] This work has made a significant contribution to the reproducibility of PSCs fabricated in an inert atmosphere across the research laboratories. At this moment of ongoing efforts in the commercialization of PSCs, it is of great importance to assemble the best fabrication protocols and practices that are less demanding and allow ambient air manufacturability, scalability, and reproducibility.[120]

Another important aspect of the commercialization of PSCs is their stability, which is best judged by maximum power point (MPP) tracking.[121–128] In a device stack, degradation can be induced by intrinsic (ion migration, polymorphism) or extrinsic (moisture, oxygen, heat, or UV light) factors.[129–135] Intrinsic factors are being addressed by engineering grain boundaries,[136–138] interfaces[139–143] and compositions.[144,145] Extrinsic factors are mainly addressed by developing encapsulation strategies to protect these devices from environmental harm.[146,147] To achieve stable MPP operation of perovskite solar cells, proper encapsulation is arguably key. Despite its apparent simplicity, a detailed and optimized encapsulation strategy is needed for the effective protection of solar cells.

Here we present comprehensive protocols for fabricating PSCs in ambient air, reaching 20% PCE.[148,149] We also report detailed encapsulation steps to achieve 500 hrs MPP operation of PSCs. Importantly, we also develop a simple encapsulation testing protocol – 120°C heat stress for 5 minutes in ambient air: we then show that an encapsulated device that withstands this rapid test will likely demonstrate multi-hundred-hours MPP operational stability.

2.2 Methods

2.2.1 Ambient air device fabrication protocol

We focus on the most common perovskite solar cell with an *n-i-p* architecture: indium tin oxide (ITO)-coated glass/tin oxide (SnO_2)/perovskite/spiro-OMeTAD/Gold (Au). All chemicals used in this work, their chemical abstracts service (CAS), producers, and catalog numbers are given in **Table 2-1**:

Table 2-1. CAS number, producers, and catalog number of chemicals for fabrication of perovskite solar cells.

Chemical	**Producer**	**CAS**	**Catalog number**
Tin(IV) oxide, 15% in H_2O colloidal dispersion	Alfa Aesar	18282-10-5	44592
$PbBr_2$	Millipore Sigma	10031-22-8	211141
PbI_2	TCI Chemicals	10101-63-0	L0279
FAI	GreatCell Solar	879643-71-7	MS150000
MABr	GreatCell Solar	6876-37-5	MS301000
MACl	GreatCell Solar	593-51-1	MS601000
CsI	Alfa Aesar	7789-17-5	10992
Spiro-OMeTAD	Xian Polymer Light Tech. Com.	207739-72-8	
Dimethylformamide (DMF)	Millipore Sigma	68-12-2	227056
Dimethyl sulfoxide (DMSO)	Millipore Sigma	67-68-5	276855
tBP	Millipore Sigma	3978-81-2	122379
Chlorobenzene	Millipore Sigma	108-90-7	284513
Li-TFSI	Millipore Sigma	90076-65-6	544094
Cobalt (III) TFSI salt	Millipore Sigma		805394

ITO-coated glass substrates (Ossila) with 25 mm × 25 mm dimensions are cleaned by sonication in deionized water, acetone, and isopropanol, each for 15 minutes, and then dried with N_2 gas gun and then subsequently ozone-treated for 15-20 minutes just before spin coating SnO_2 electron transport layer (**Figure 2-1**).

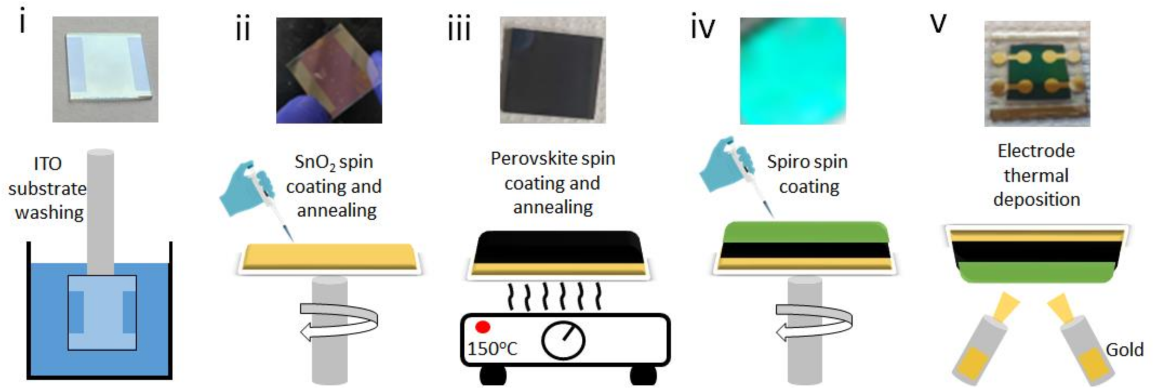

Figure 2-1. Step-by-step fabrication of perovskite solar cells. (i) Washing substrates in water, acetone and IPA; (ii) Deposition of SnO_2; (iii) Deposition of perovskite layer; (iv) Deposition of Spiro-OMeTAD by dynamic spin coating; (v) Deposition of gold by thermal evaporation

SnO_2 electron transporter layer is then deposited on ITO-coated glass from a solution of SnO_2 nanoparticles by spin coating in ambient air. A solution of SnO_2 is prepared by mixing deionized water and 15% SnO_2 colloidal dispersion nanoparticles in a 6:1 volumetric ratio, respectively. This mixture is then sonicated for 30 minutes and filtered with 0.45 micron PTFE syringe filter. Then, 0.15 ml of this solution is spin-coated on the ITO-coated glass at 3,000 rpm for 30 seconds, and annealed at 150ºC for 30 minutes, and then ozone-treated for 30 minutes in the ambient air. SnO_2 deposition is relatively straightforward, but occasional non-uniformity of the film occurs: this issue can be addressed by changing the pipette tip as it accumulates precipitated particles or air bubbles. SnO_2 film thickness should be about ~30-40 nm (**Figure 2-3c**) which bare eyes can roughly diagnose due to light interference: sky blue color with a yellowish substrate (high-conductive ITO) or yellowish color with a colorless substrate (low-conductivity ITO) indicates the right thickness of SnO_2. These SnO_2-coated substrates are again given ozone treatment for 20 minutes.

The SnO_2-coated substrates are treated under UV/Ozone for minutes. Perovskite is then deposited on ITO-coated glass/SnO_2 substrates. This step is arguably the most sensitive one to processing conditions. Many perovskite compositions are now developed, but two of them – $Cs_{0.05}FA_{0.8}MA_{0.15}PbI_{2.55}Br_{0.45}$ (CsMAFA) and $FA_{0.95}MA_{0.05}PbI_{2.85}Br_{0.15}$ (MAFA) (Cs: cesium; MA: methylammonium, $CH_3NH_3^+$; FA: formamidinium, $HC(NH_2)_2^+$) – are most reported compositions. MAFA and CsMAFA perovskite solutions are prepared by mixing appropriate amounts of components as shown in **Table 2-2**. 0.1 ml perovskite solution is then spin-coated in a three-step (**Figure 2-2a**) process on top of SnO_2-coated substrate and then thermally annealed at 150°C for 10 minutes for crystallization in ambient air. The three-step deposition process enables a controllable deposition of the perovskite layer: in the first step, the spinner speed is slow (500 rpm) to spread the ink (**Figure 2-2a**); the speed is then raised (1000 rpm) to control the thickness of the film; finally, in the last step, antisolvent (a solvent that is miscible with the solution, but has poor solubility of the solutes, diethyl ether (DEE) is used as an antisolvent in this work) is dropped to induce crystallization.[150] Note that the displayed temperature on the hotplate might differ from the real temperature of the surface of the plate; it is important to use a sensor to measure and calibrate actual surface temperature.

Table 2-2. Precursor solutions.

Chemical	**CsMAFA**	**MAFA**	**Spiro-OMeTAD**
$PbBr_2$, mg	77	7.1	

PbI_2, mg	548	582.7	
FAI, mg	194.4	217	
MABr, mg	22.3	7.1	
MACl, mg		22	
CsI, mg	18		
Dimethyformamide, ml	0.8	0.8	
Dimethyl sulfoxide, ml	0.1	0.1	
Spiro-OMeTAD, mg			100
tBP, ml			0.039
Chlorobenzene, ml			1.1
Li-TFSI (pre-dissolved in acetonitrile, 540 mg/ml), ml			0.025
Cobalt salt (pre-dissolved in acetonitrile, 376 mg/ml), ml			0.010

We prepared both CsMAFA and MAFA perovskite films in ambient air and found, by X-ray Diffraction (XRD), CsMAFA to be impure (**Figure 2-3a**), likely due to high hygroscopicity of Cs.[151,152] CsMAFA diffraction profile shows a peak at ~11.7° corresponding to the non-perovskite or delta phase of the material,[153] while the perovskite peak at ~14.1° is broad indicating of its low crystallinity. In contrast, sharp XRD perovskite peaks are observed for MAFA films (**Figure 2-3a**). We, therefore, chose MAFA as a protocol candidate for the ambient air fabrication of PSCs. We observed that the relative humidity (RH) should be less than 35% to prepare MAFA perovskite films reproducibly.

In perovskite fabrication, seemingly trivial details in antisolvent dropping are important to obtain uniform and smooth films generally featured with mirror-like surface due to high specular reflection (**Figure 2-2c**). The antisolvent flow should be continuous but not too thin or thick to avoid the 'coffee ring' effect (**Figure 2-2d**).[154,155] Cutting a pipette tip to make ~5 mm opening diameter (**Figure 2-2b**) ensures an optimal flow of antisolvent; to stop the spontaneous flow of the low-viscous DEE (the dynamic viscosity of DEE is ~4×

lower than water at room temperature) through this wide opening, the tip can be cooled by filling/emptying for several times.

The amount of antisolvent also plays a role in the formation of the high-quality film: no DEE or 200-400 µl DEE (**Figure 2-2e-h**) leads to unsmooth/non-reflective films. We observed that using a relatively large amount of DEE, ~1 ml, is essential for ambient air fabrication of mirror-like perovskite films (**Figure 2-2c**): DEE, as a low-boiling point (35°C) substance, rapidly evaporates during spin-coating creating an inert-like atmosphere during perovskite film formation.

We also observed that if there is high humidity and temperature (RH above 40% and temperature above 30°C), the anti-solvent should be dropped ~3 s before the end of 3rd step of spin-coating of perovskite film to avoid the formation of rough films due to rapid evaporation of solvents. And, if humidity and temperature (RH below 30%) are low, then the anti-solvent can be dropped ~5 s before the end of 3rd step of spin-coating.

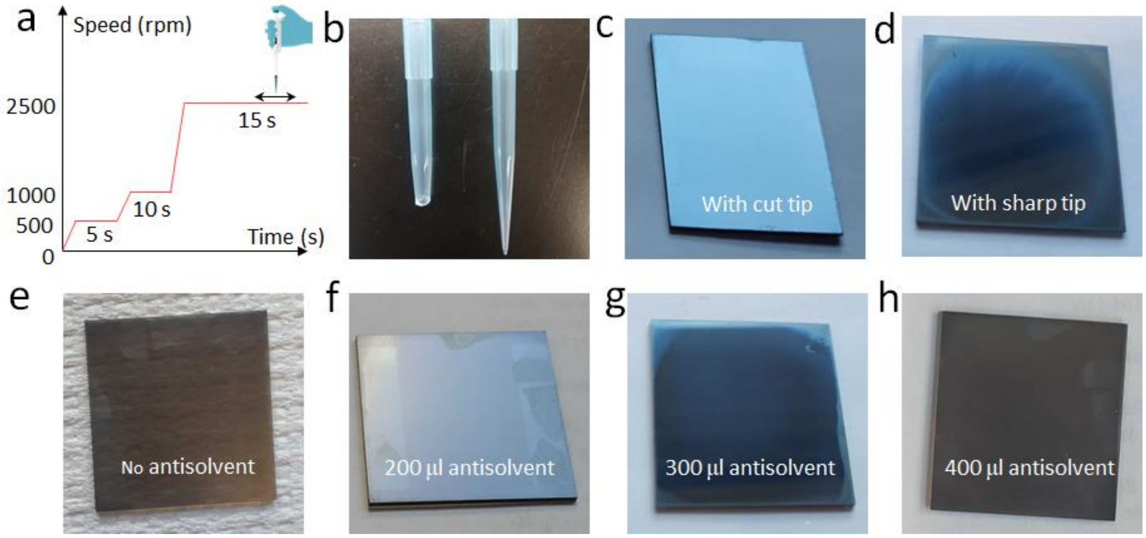

Figure 2-2. Perovskite film deposition details. (a) Spin-coating profile of perovskite film. (b) Pipette tips. (c-h) Pictures of perovskite films prepared with (c) 1 ml antisolvent and cut-pipette tip, (d) 1 ml antisolvent and regular pipette tip, and (e-h) various amounts of antisolvent.

Spiro-OMeTAD is then deposited on perovskite films by spin-coating. 0.075 ml of spiro-OMeTAD solution (**Table 2-2**) is deposited with a dynamic spin coating method at 2,000 rpm for 30 seconds. It is necessary to clean the walls of spin-coater if the perovskite film was deposited on the same spin-coater; otherwise, the residual solvents may etch the perovskite and spiro-OMeTAD films. The edges of the device are then cleaned for deposition of gold on ITO cathode for efficient collection of current.

Finally, ~80 nm layer of gold is deposited with three grading rates: 0.2 Å/s until 1 nm, 0.5 Å/s from 1 to 10 nm and 1.5 Å/s above 10 nm. Low-rate metal deposition at the start ensures that the films remain intact. The final step, high-rate metal deposition, should avoid over-heating the thermal deposition chamber; otherwise, the devices will degrade.

A well-controlled gold deposition is essential in achieving reproducible and efficient PSCs.[119] The devices are then kept overnight in a dark dry box to oxidize spiro-OMeTAD fully.

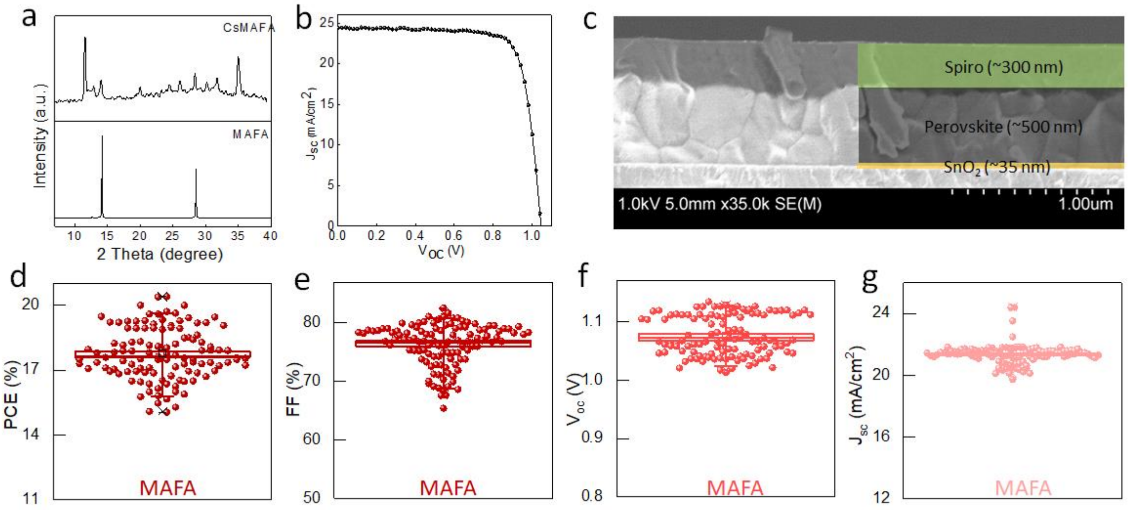

Figure 2-3. Characterization of perovskite films and solar cells. (a) XRD spectra of perovskite films; (b) *JV* curve of the champion cell; (c) Cross-sectional SEM image of the perovskite solar cell; (d) PCE, (e) fill factor (FF), (f) open-circuit voltage (V_{OC}) and (g) short-circuit current (J_{SC}) for over 100 perovskite solar cells fabricated in ambient air.

We fabricated 115 devices in ambient air following the protocols discussed above. The devices' figures-of-merit were measured with Ossila source meter and AAA class Newport solar simulator. The average PCE was 18% (**Figure 2-3d**), while ~25% of cells showed over 19% PCE with a champion cell surpassing 20% (**Figure 2-3b**). The average fill factor (FF) was 77% (**Figure 2-3e**) and the open-circuit voltage (V_{OC}) was consistently above 1 V (**Figure 2-3f**). The average short-circuit current (J_{SC}) was 21.5 mA/cm^2 (**Figure 2-3g**) and can be further increased by light management (e.g., minimizing reflection and parasitic absorption).

2.2.2 Encapsulation

Device encapsulation is essential for achieving the long-term operational stability of solar cells. Many materials are used to encapsulate PSCs.[156] Due to the vulnerability of PSCs to thermal stress, we excluded those methods that require hot pressing[157] (e.g., polyisobutylene (PIB),[158] polydimethylsiloxane (PDMS),[159] ionomers). Therefore, we tested the two most-reported encapsulation strategies that require no additional pieces of equipment, such as a laminator.

We first encapsulated our PSCs by sandwiching them between two glass covers and using butyl rubber tape as a sealant (**Figure 2-4a**). A copper tape was attached to the pixel to extract the current. This encapsulation is stable against water ingress when dipped in water. However, due to the fragility of copper tape, it was challenging to get a proper electrical connection for the current-voltage (*IV*) or stability measurements. To address this issue, we tried soldering the metals; however, due to the high temperatures required for this process, the gold (top contact of PSCs) peeled off. In addition, the second glass at the front layer increases light loss due to reflection.

We then attempted to encapsulate our devices with a cavity glass cover (AGM, Korea) (**Figure 2-4b-i**) and epoxy sealant (LUMTEC). Encapsulation must be done in an inert atmosphere to avoid air and moisture traps that degrade devices during operation. After deposition of spiro-OMeTAD, the film is etched from all four edges, and only the active area of the pixel is kept to avoid any contact of adhesive sealant with perovskite or other layers

(**Figure 2-4b-ii**). A clean glass cover with the size of the active area and epoxy sealant on its edges is then placed on the top of the device. The curing (a photochemical reaction that generates a crosslinked network of polymers) occurs under a 15 Watts UV lamp (Alonefire SV13 with 360 nm UV LED and 2800 mW luminous power) within 5 minutes at room temperature. The process of encapsulation, all the way from sealant positioning to its curing requires being extra cautious. First, both glass cover and tweezer should be clean to avoid any particles being sandwiched between the device and cover glass; otherwise, those particles may damage the solar cell. Second, the glass covers with epoxy sealant should be picked from the sides (**Figure 2-4b-iii & iv**). Placing the tweezer on top of the epoxy side disturbs the uniformity of the sealant and leaves a hole which then provides a pathway for air and moisture ingress.

Epoxy/glass-encapsulated PSCs were also stable against water ingress when dipped in water and kept for 30 min at an elevated temperature until 50^{o}C (**Figure 2-4c**). *JV* characteristics measured before and after submerging in water showed a surprising increase in performance from 16.5% to 17.9%. Understanding this phenomenon will remain a subject of our future studies.

2.2.3 Encapsulation testing

We then aimed to develop an accelerated aging test protocol to determine the effectiveness of encapsulation. For this, both encapsulated and unencapsulated devices were heated in ambient air at different temperatures for a short period. A temperature at which visual discoloration of the un-encapsulated device occurs, while the encapsulated device remains intact, is chosen as a condition for testing the effectiveness of encapsulation.

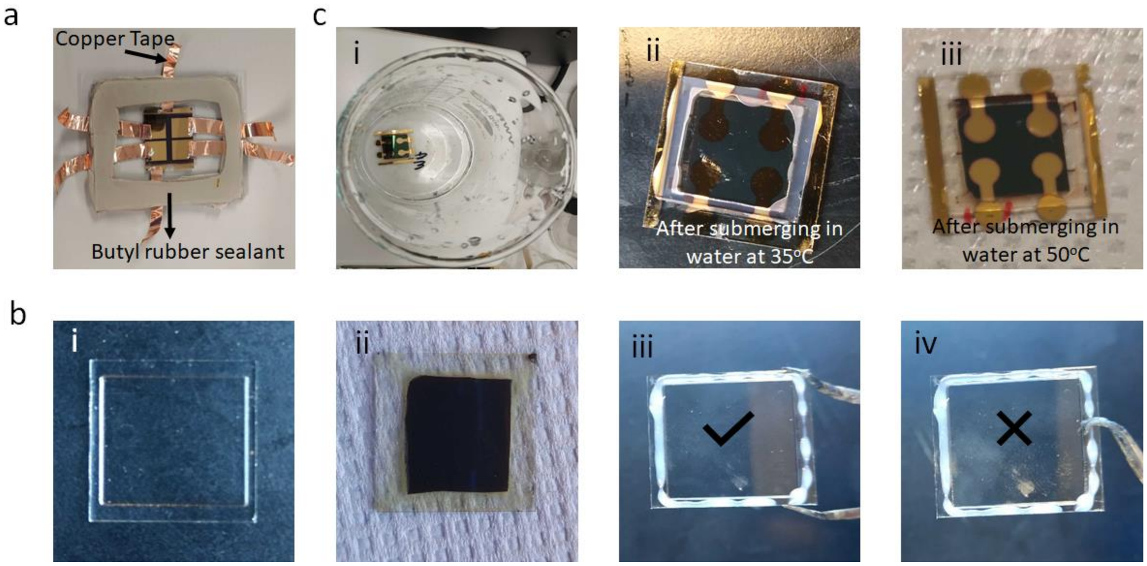

Figure 2-4. Encapsulation of perovskite solar cells. (a) Encapsulation of device sandwiched between two glass covers and sealed with a butyl sealant; (b) Images of (i) cavity glass cover, (ii) film etched from the edges, (iii, iv) handling cavity glass; (c) Water submerging tests (i) a device dipped in a beaker filled with water, (ii) device after submerging at 35°C (iii) and 50°C.

The results (**Figure 2-5**) suggest that the annealing of both encapsulated and unencapsulated devices at 100°C for 5 and 10 minutes did not lead to any visual degradation. However, when the temperature was increased to 120°C and the devices were kept for 5 minutes, the un-encapsulated device began to degrade. In contrast, the encapsulated device did not show any sign of degradation. Therefore, this condition (annealing at 120°C for 5 minutes) was chosen as a rapid protocol to test encapsulation effectiveness. Only those devices that withstand this test were then chosen for MPP.

2.2.4 Maximum power point operation

We then tested the stability of encapsulated devices under MPP conditions at room temperature and RH of 35%. We used a white LED as a light source because a Xe lamp, which provides a spectrum closer to AM 1.5G has a short lifetime that limits long-duration measurements. Though LED source has a limited near-infrared light portion, it can generate similar values of carrier concentration to Xe lamp and hence negligibly impacts the performance of solar cells. Therefore, LED sources are widely used in the community for long-term stability tests.[160] We used Ossila source meter to record MPP figures – it regularly measures *JV*, finds V_{MPP} at which maximum power is generated and keeps the devices at V_{MPP}.

Figure 2-6 shows the operational stability results of our device. To mimic sunlight intermittency, we periodically kept devices in dark for 12 hrs. Devices show burn-in period, i.e., loss of device performance until it stabilizes in 30 min. Formation of charged regions[161] under MPP conditions leads to degradation of photocurrent; however, these meta-stable states dissipate away upon dark storage, and the photocurrent (or the PCE) self-heals to its initial value.[161] Therefore, burn-in losses recover after each dark-resting cycle shown in Figure 14a. The device retained ~95% of its initial performance following over 500 hrs of operation at the MPP.

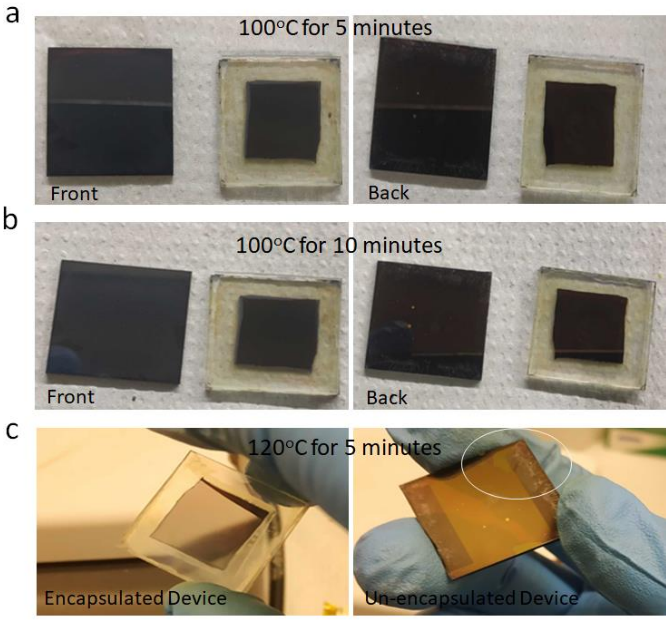

Figure 2-5. Encapsulation testing protocol. (a) 5 and (b) 10 minutes of thermal stress at 100°C; (c) 5 minutes of thermal stress at 120°C – no visible changes were observed for an encapsulated device, whereas the un-encapsulated device began to show some discoloration.

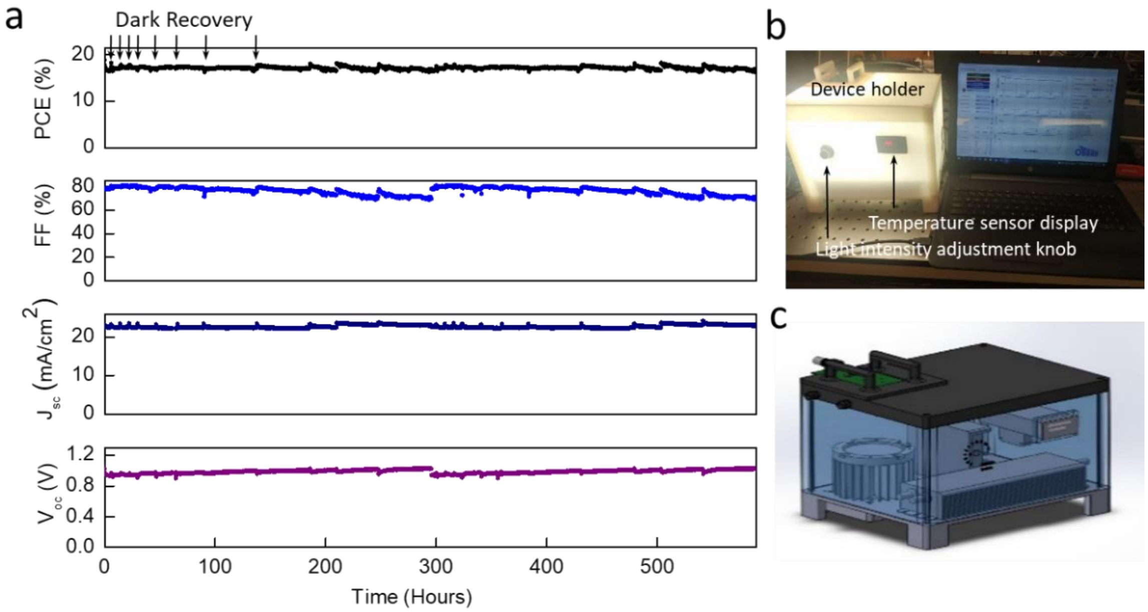

Figure 2-6. Maximum power point operational stability of perovskite solar cells. (a) Figures-of-merit as a function of time (arrows show 12 hours dark recovery cycles); (b) Photo and (c) schematic of the home-built stability testing station.

2.3 Conclusions

In conclusion, we reported detailed protocols for fabricating efficient perovskite solar cells in ambient air. We also showed a simple and robust encapsulation technique and complementary accelerated encapsulation testing protocol. We showed that an encapsulated device that stands 120^{o}C for 5 minutes will also stand long-term MPP condition, demonstrating over 500 hrs of stable operation at the maximum power point operation.

Chapter 3.

Selective Deactivation of Perovskite Grain Boundaries

[Reproduced (adapted) with alterations from: ''**Muhammad Awais**†, Soumya Kundu†, Dongyang Zhang, Vishal Yeddu, Mohammad Reza Kokaba, Yameen Ahmed, Furui Tan, Makhsud I. Saidaminov. *Selective Deactivation of Perovskite Grain Boundaries*. *Cell Reports Physical Science*, **2023**, 4, 1016634."]

Contributions to research and writing

In this paper, I prepared all samples and developed methods of fabrication of solar cells, carried data collection and data analysis. My co-first author Dr. Soumya Kundu synthesized the biphenyl halide molecules. I also wrote the first draft of the manuscript and led it through revision process until publication. The study was supervised by Dr. Makhsud I. Saidaminov.

Transition section

As discussed in previous chapters, perovskites suffer from different degradation mechanisms and among them grain boundaries are a major origin of degradation because of presence of high density of defects at grain boundaries. In this chapter, a selective grain boundary passivation strategy for perovskite solar cells using biphenyl-based ligands is demonstrated. The findings reveal that these ligands specifically interact with PbI_2-rich interfaces (which is present at the grain boundaries) while remaining inert toward the perovskite itself. This targeted passivation approach achieved two critical improvements: (1) extending radiative recombination lifetimes from 1 to 2.7 μs while maintaining efficient charge transport, and (2) enhancing moisture resistance through the hydrophobic benzene rings, which enhanced the material's stability in aqueous environments by a factor of 3. Fabricated entirely under ambient conditions, the resulting devices exhibited high reproducibility with efficiencies ranging from 17% to 21%, while achieving a high open-circuit voltage of 1.11 V.

3.1 Introduction

Perovskite solar cells (PSCs) surpassed 25% power conversion efficiency (PCE) in the lab and are now at the cusp of commercialization.[76,98–100,162–169] Perovskites provide a range of desirable optoelectronic properties, including bandgap tunability and long charge-carrier lifetime.[170–174] A major challenge in the development of PSCs has been their instability against moisture and oxygen, which can lead to the decay of their performance much faster than the stability standards demand for.[175–179]

Following gradual move from $MAPbI_3$ (MA stands for methylammonium, $CH_3NH_3^+$) to $FAPbI_3$ (FA stands for formamidinium, $HC(NH_2)_2^+$) as a light absorber layer, many important studies improved the stability of PSCs.[113,180–185] For example, Seok *et al.* demonstrated compositional engineering of PSCs and incorporated $MAPbBr_3$ into $FAPbI_3$ to stabilize the perovskite phase.[186,187] You *et al.* introduced organic halide salt, phenethylammonium iodide (PEAI), and Huang *et al.* introduced quaternary ammonium halides for defect passivation or interface engineering.[188,189] Grätzel *et al.* tailored the morphology and structure of the perovskite absorber layer by phosphonic acid ammonium additives which act as a cross-linker between neighboring grains.[190,191]

It is well established by now that grain boundaries (GBs) in perovskites are a major source of degradation in PSCs.[192] This is because GBs have a higher density of defects and impurities, and hence thermodynamically more reactive than the bulk. When PSCs are exposed to stressors such as moisture, light, bias, or high temperature, GBs break first and lead to the overall degradation of the device.[193,194] For example, water molecules easily deprotonate ammonium cations at interfaces.[195,196]

The conventional approach for surface passivation of perovskites is to incorporate a low-dimensional structures, predominantly with the aid of PEAI. While effective at time-zero, these low-dimensional perovskite tend to react with underlying perovskite under external stimuli. In addition, they are unselective to GBs only: they cover all surface, potentially impeding charge carrier collection from the grains. Therefore, there is a need for selectively passivating grain boundaries in PSCs is needed while keeping the surface of grains intact.[197]

Here we synthesize and apply biphenyl methylammonium halides and show that they selectively reside on defective sites at the surface, primarily targeting GBs. We attribute this behavior of biphenyl moieties to two benzene rings offering higher electron cloud density (and hence stronger tendency to passivation)[198] and higher hydrophobicity (and hence stronger stability against moisture) than PEAI.[199] This approach also increases charge-carrier lifetime by a factor of ~3, resulting in a PCE of 21%, all made in ambient air, with a significant extension of shelf-life and operational stabilities.

3.2 Results and discussion

3.2.1 Device structure

Following our ongoing interests in ambient-air fabrication of stable PSCs,[200] we turned our attention to surface passivation of perovskite. The effect of BiPhX passivation was studied on planar perovskite solar cells with an architecture of glass/ITO/SnO_2/perovskite ($FA_{0.95}MA_{0.05}PbI_{2.85}Br_{0.15}$)/BiPhX/spiro-OMeTAD/Au (**Figure 3-1a**), the fabrication of which we reported in detail in our previous work.[200]

3.2.2 Effect of BiPhX interlayer

We first studied the effect of different counter ions to biphenyl methylammonium cation on perovskite photovoltaic performance. We synthesized iodide, bromide and chloride (referred to as BiPhI, BiPhBr and BiPhCl, respectively) salts of BiPhX, dissolved in anhydrous 2-propanol in 2 mg ml^{-1} concentration, and spin-coated on top of perovskite films (all made in ambient air). We did not synthesize fluoride salt due to safety concerns as it requires the use of highly corrosive hydrofluoric acid (HF). Moreover, traces of HF residue can lead to rougher surfaces and may penetrate through thin films to damage electron transport layer (ETL) or ITO.[201]

We found that BiPhI-treated films had better photovoltaic performance than the control, BiPhBr- and BiPhCl-treated ones (**Figure 3-2**). X-ray diffraction (XRD) analysis revealed that BiPhCl and BiPhBr shifted perovskite diffraction peak indicative of halide exchange and/or of structural strain in perovskite after passivation.[202] But BiPhI–treated films showed no observable changes on perovskite diffraction pattern (**Figure 3-3**) indicating intact perovskite structure. Therefore, we chose BiPhI as a candidate for surface passivation.

We then varied the concentration of BiPhI in 2-propanol and found that 2 mg ml^{-1} as an optimum (**Figure 3-4**). At this optimized concentration, the deposited BiPhI layer on perovskite is thick enough to passivate surface defects, and thin enough to avoid disturbance of charge transport. A further increase in BiPhI concentration results in poor device performance (mainly fill factor) due to excessive accumulation of insulating phenyl moieties.[203]

Next, we studied the effect of post-annealing (after BiPhI deposition) on device performance. The results show that the un-annealed films after BiPhI deposition perform better than the annealed ones (**Figure 3-5**). This observation agrees with an earlier finding of enhanced stability of PSCs with two-dimensional perovskite layers formed at room temperature with oleylammonium iodide molecules.[204] The higher device efficiency of un-annealed devices could be attributed to better band alignment, resulting in efficient charge transfer at the perovskite-HTL interface (HTL stands for hole transport layer).

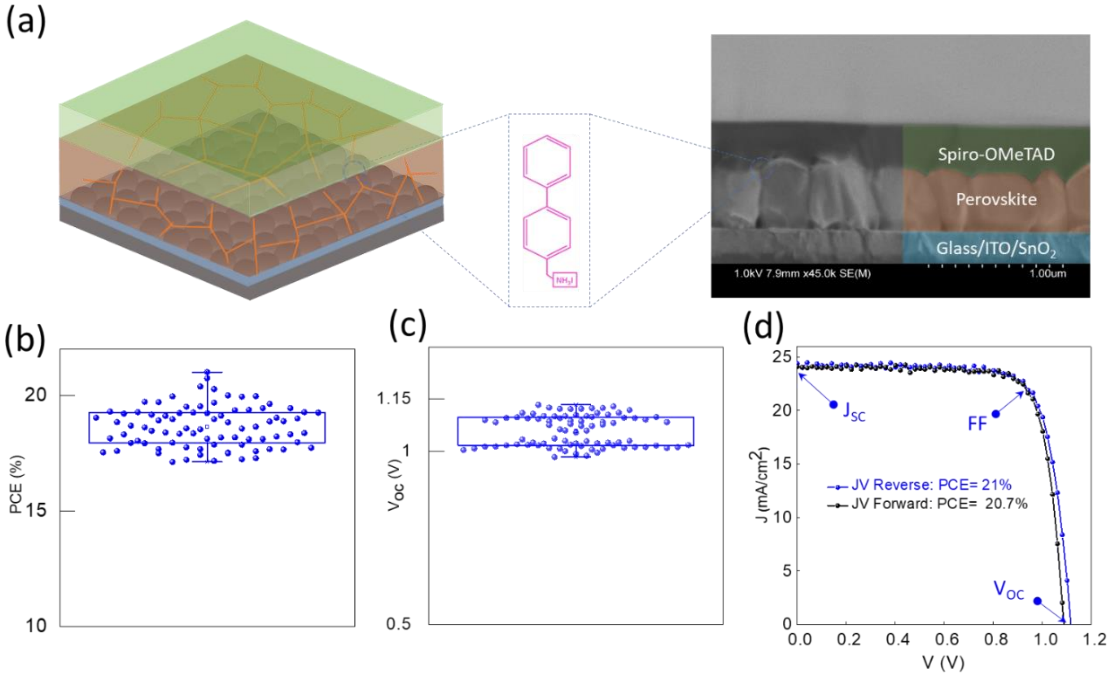

Figure 3-1. Perovskite solar cell structure and performance. (a) Schematic and cross-sectional SEM image of a typical cell with an architecture of glass/ITO/SnO_2/perovskite/BiPhI/Spiro-OMeTAD/Au (note that Au is not seen in this image). The middle panel shows the chemical structure of biphenyl methylammonium iodide. (b) Power conversion efficiency, (c) and open-circuit voltage (V_{OC}) of 84 independent perovskite solar cells with BiPhI passivation layer. The boxes indicate the 25th and 75th percentiles. The whiskers indicate the minimum and maximum values. The mean value is represented by an open square symbol. (d) Current-voltage characteristic of a champion target cell.

Figure 3-1b shows the statistical data of 84 fabricated devices modified with optimized parameters for BiPhI (2 mg ml^{-1} concentration and without post-annealing). The data show the reproducibility of the devices with mean efficiency of 19% and a consistently enhanced open-circuit voltage over 1 V (**Figure 3-1c**). **Figure 3-1d** exhibits the *JV* curve of the champion device with 21% PCE.

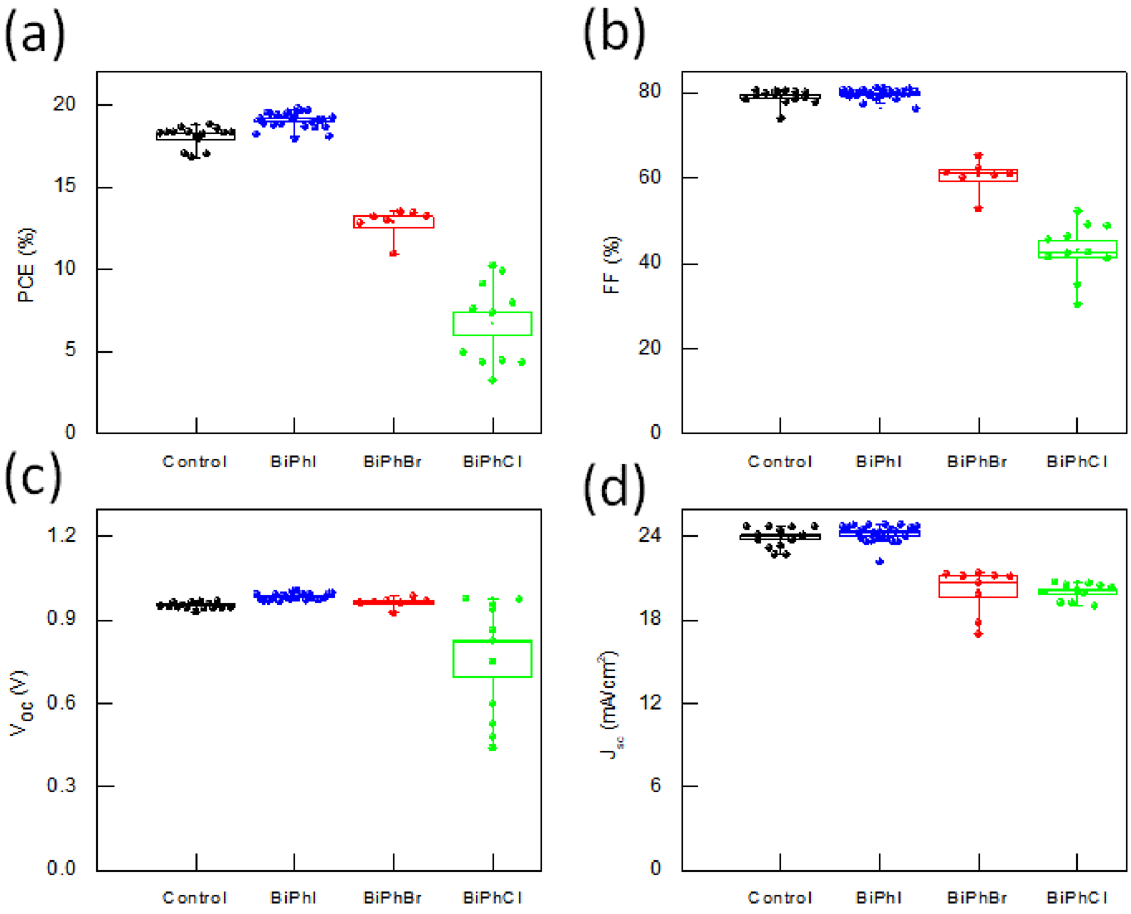

Figure 3-2. Optimization of devices based on different passivation molecules. (a) Power conversion efficiency (PCE), (b) Fill Factor (FF), (c) Open-circuit Voltage (V_{OC}) and (d) Short-circuit Current (J_{SC}). The BiPhX salts were dissolved in 2-propanol in 2 mg/ml concentration.

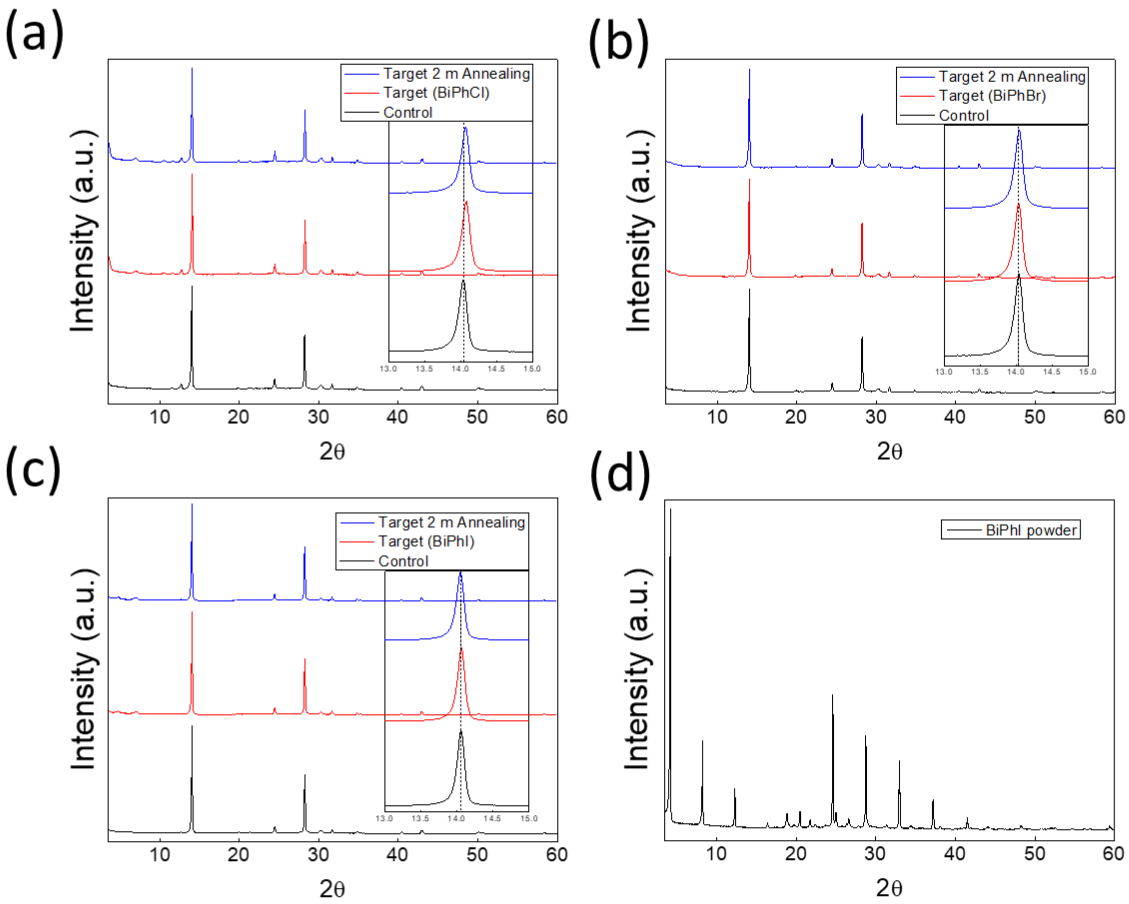

Figure 3-3. XRD patterns of (a) Control and BiPhCl treated films, (b) Control and BiPhBr treated films, (c) Control and BiPhI treated films, and (d) BiPhI powder.

To probe the presence of BiPhI on perovskite film, we carried out X-ray diffraction (XRD) of both control and target films (**Figure 3-8a**). We found that perovskite's sharp diffraction peak at ~14.1° is observed in both films. However, a new peak at a diffraction angle of 4.7° is observed in the XRD spectra of target film only which cannot be attributed to BiPhI (BiPhI shows a diffraction peak at 4.2°, **Figure 3-3d**). To understand the origin of the diffraction peak at 4.7° on perovskite, we carried out a control experiment: we prepared 1 M solution of BiPhI and PbI_2 in 2:1 ratio, respectively, in DMF, spin coated on a glass substrate. This product showed a diffraction angle of 4.7°, exact same location as we observed on perovskite film (**Figure 3-6**).

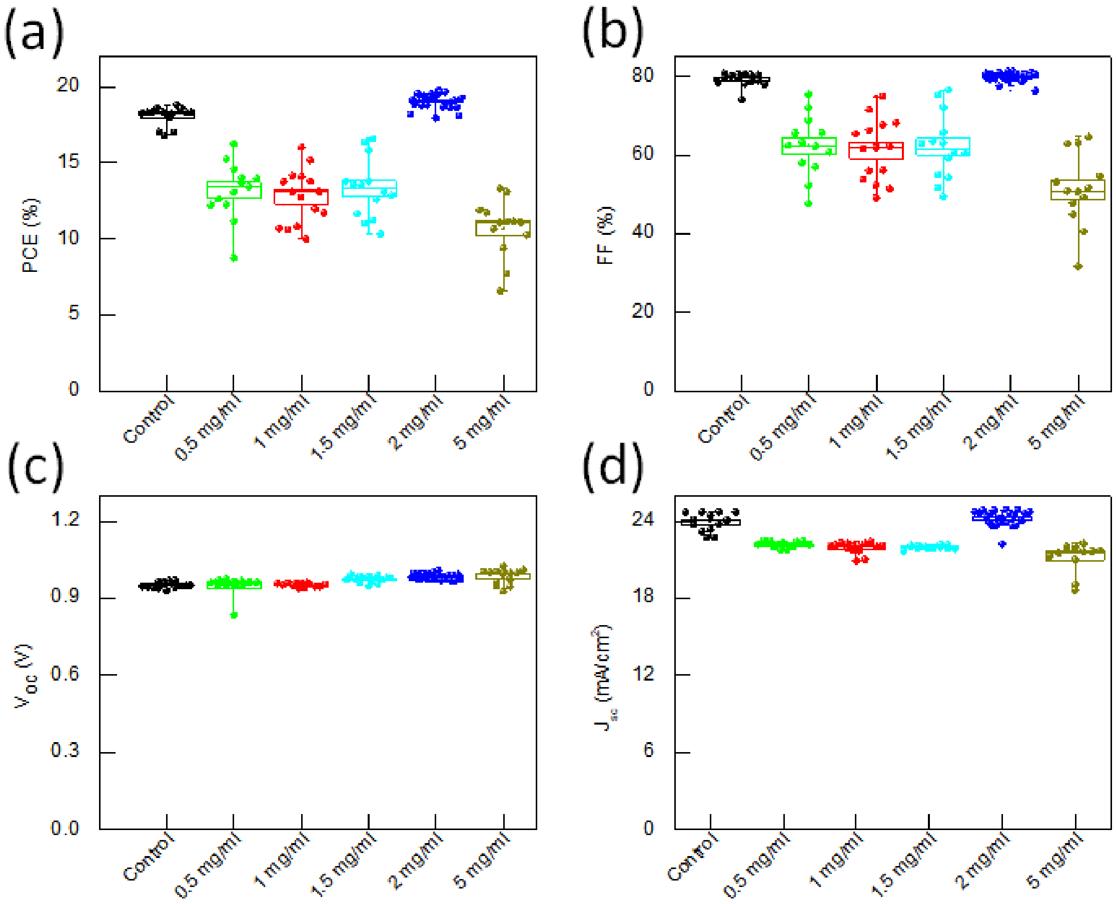

Figure 3-4. Optimization of devices based on varying concentration of BiPhI in 2-propanol. (a) Power conversion efficiency (PCE), (b) Fill Factor (FF), (c) Open-circuit Voltage (V_{OC}) and (d) Short-circuit Current (J_{SC}).

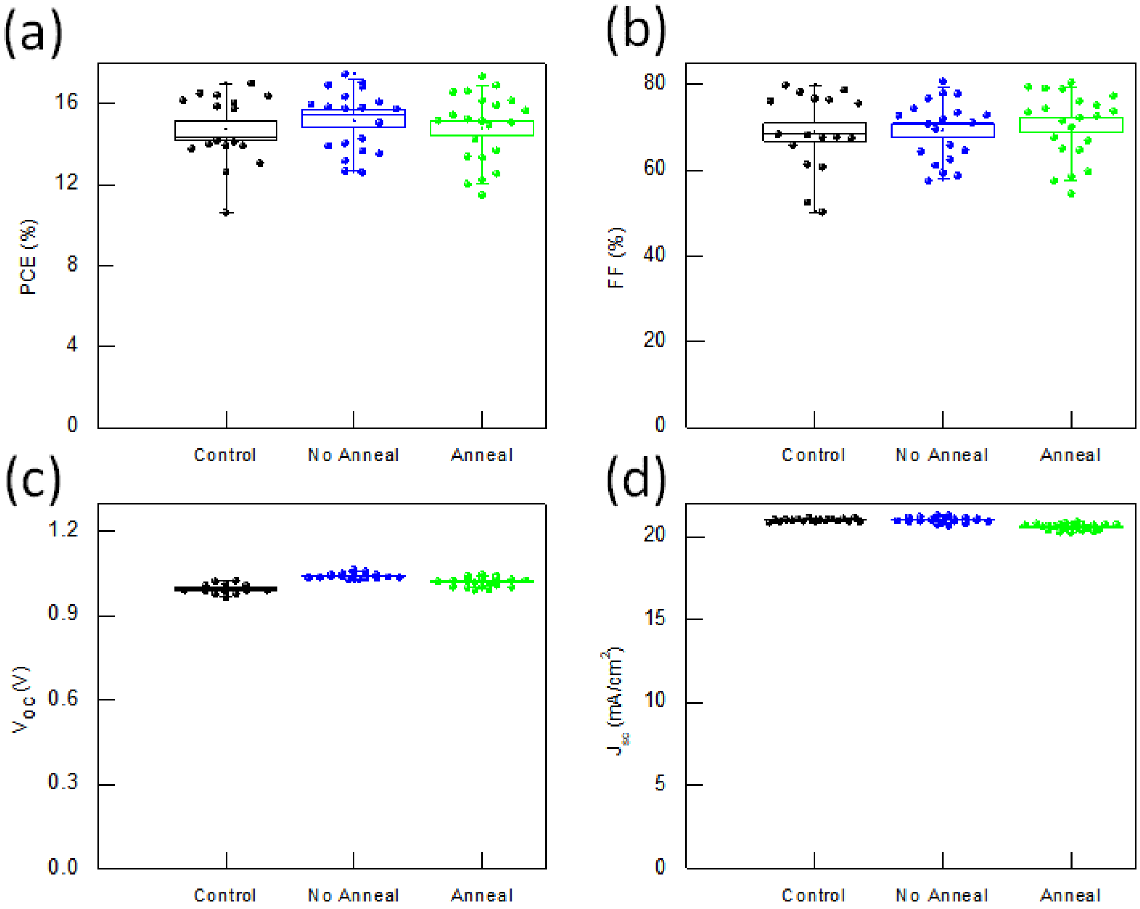

Figure 3-5. Optimization of devices based on annealing and no annealing of after depositing passivation material. (a) Power conversion efficiency (PCE), (b) Fill Factor (FF), (c) Open-circuit Voltage (V_{OC}) and (d) Short-circuit Current (J_{SC}).

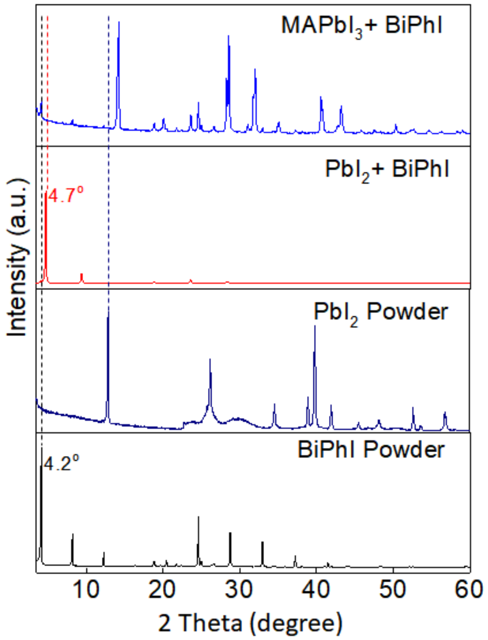

Figure 3-6. XRD patterns of BiPhI powder, PbI$_2$ powder, PbI$_2$ and BiPhI powder, MAPbI$_3$ and BiPhI powder.

We studied the morphology of the films with scanning electron microscope (**Figure 3-8d**). The control films show an obvious presence of unreacted PbI$_2$ (white grains). After passivation with BiPhI, we surprisingly observed that it majorly resides on the GBs, while keeping the surface of perovskite grains intact. To understand the origin of this selective behavior of BiPhI, we treated ground MAPbI$_3$ single crystal with BiPhI and observed no reaction between them (**Figure 3-6**). In contrast, we observed complete reaction between BiPhI and PbI$_2$ (**Figure 3-6**). We hence conclude that BiPhI selectively passivates GBs because it mainly reacts with PbI$_2$ which usually exists in GBs, while keeping the surface of perovskite grains intact for intimate connection with hole transporter layer.

To probe the origin of increase in the V_{OC}, we monitored the steady-state photoluminescence (PL) of both target and control perovskite films. We observed that the

PL intensity for the target film was nearly twice higher than the control film (**Figure 3-8b**). The PL lifetime of the perovskite film significantly increased from 1.0 μs to 2.7 μs after treatment with BiPhI (**Figure 3-8c**). This increase in PL intensity and radiative recombination lifetime indicates a significant reduction in the carrier losses, hence, increasing the V_{OC}.

3.2.3 Film and device stability

We investigated the stability of the control and target films against water. We first conducted the contact angle measurement: the control film showed a sharper angle to water droplet than the target film indicating the resistance of target's surface to water/moisture (**Figure 3-9a**).

To further confirm this, we directly put a droplet of water on both control and target films. We observed that the control film shows an obvious sign of degradation in less than a second; however, the target film shows resistance against water and degrades in at least 3× longer time (**Figure 3-9b**).

We then conducted humidity test of the films. Both control and target films were placed in a container having ~87% of relative humidity (RH): we observed significant discoloration of the control film after 6 days under these conditions, while the target film remained almost intact within this period (**Figure 3-9c**).

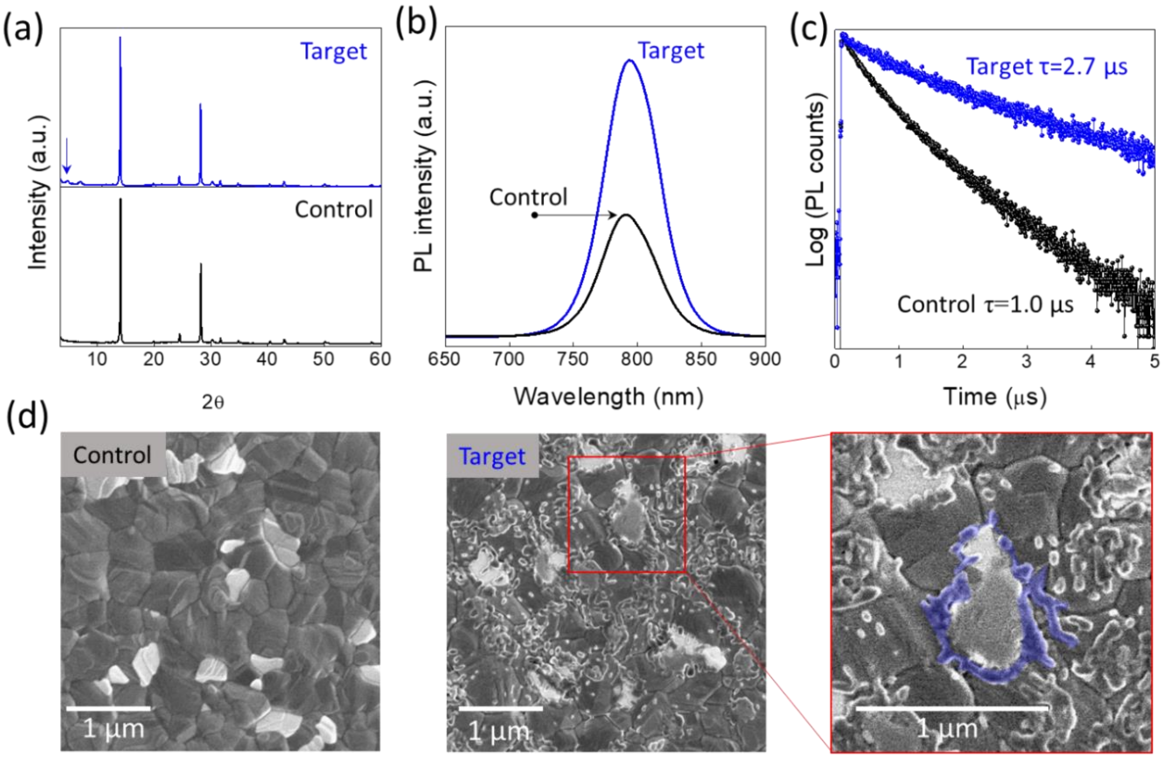

Figure 3-7. Characterization of films. (a) XRD pattern, (b) steady-state photoluminescence spectrum, (c) time-resolved photoluminescence decay at 790 nm, and (d) scanning electron microscope (SEM) images of control and target films showing selective passivation of grain boundaries. Blue-shaded area is a guide for eyes highlighting special distribution of passivating materials.

We also tested the stability of both the control and target encapsulated devices at maximum power point (MPP) operation (Figure 3-9D) at room temperature and RH of 25%–35%. The target device showed a gradual increase in device performance over time, indicating that the use of BiPhI creates a robust interface with the HTL. In contrast, the control device lost >30% of its initial efficiency in 25 h, while the target device remained stable for >300 h. This stability enhancement can be attributed to suppression of ion migration through the perovskite-HTL interface due to surface passivation[205] as well as chemical inertness of biphenyl methylammonium lead iodide, as we discuss below.

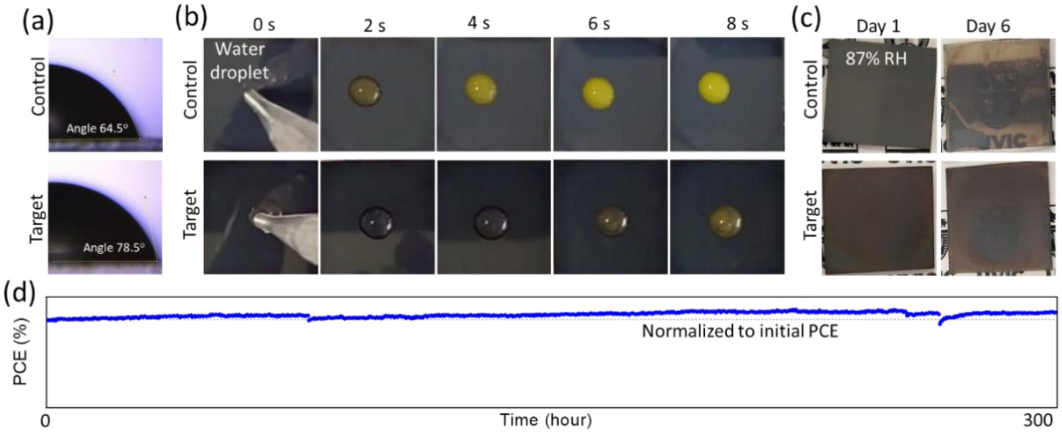

Figure 3-8. Moisture-tolerance testing of perovskite film and device operational stability. (a) Contact angle between water and perovskite film. (b) Perovskite film appearance under water droplet. (c) Perovskite film's appearance under water vapor. (d) Operational stability of encapsulated target perovskite solar cell.

To understand the origin of improved stability against moisture, we synthesized biphenyl methylammonium lead iodide single crystals from BiPhI and PbI_2 in hydroiodide acid solvent (see Methods section for details). The structures of the crystal was identified by single-crystal X-ray diffraction (crystallographic information files (CIFs) is attached and deposited in Cambridge Crystallographic Data Centre (CCDC) under deposition numbers 2260262). This compound crystallized in monoclinic symmetry, C1 2/c 1 space group, with a brutto-formula of $(C_6H_5\text{-}C_6H_4\text{-}CH_2\text{-}NH_3)_3Pb_2I_7{\cdot}H_2O$, in a two-dimensional pattern, with alternating organic and inorganic layers ((**Figure 3-9a**). The organic layer is made of C_6H_5-C_6H_4-CH_2-NH_3^+ ligands, resembling edge-to-face herringbone motif of benzene, indicating of in-layer π-π interaction (**Figure 3-9d**).[206] The inorganic layer is made of trimers of PbI_6 octahedra (face and edge-shared) connected through corners of PbI_6 (**Figure 3-9c**).

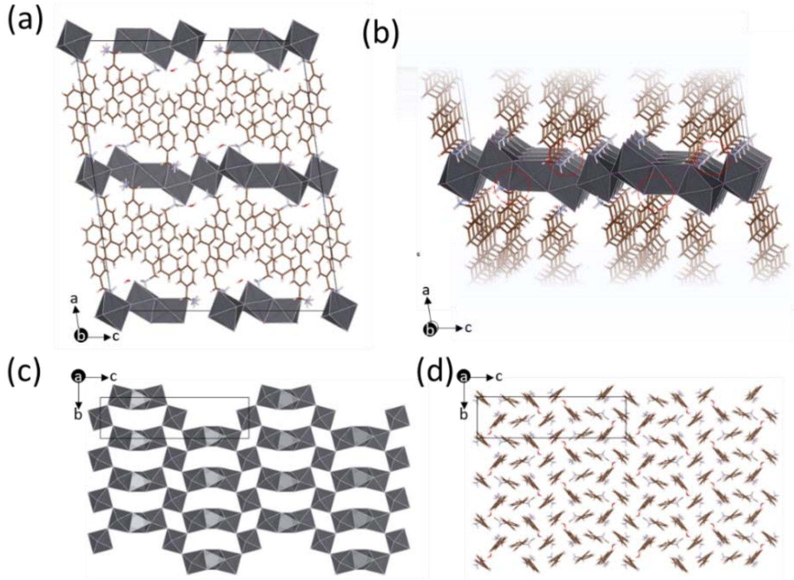

Figure 3-9. Crystal structure of $(C_6H_5\text{-}C_6H_4\text{-}CH_2\text{-}NH_3)_3Pb_2I_7{\cdot}H_2O$. (a) Projection of the crystal structure on ac crystallographic plane. (b) The same as (a) with a focus on interaction of organic and inorganic motifs. (c) Inorganic, and (d) organic sublattice of the crystal structure.

When zoomed in, one can clearly observe interpenetration of organic and inorganic sub-lattices (**Figure 3-9b**), indicating strong interaction between the two. This is different from conventional 2D perovskites (e.g., phenethylammonium lead iodide), in which the octahedra are only corner-shared and the two sub-lattices remain spatially separate and hence prone to disintegrate (i.e., decompose). The biphenylmethylammoinum lead iodide's π-π interaction within organic sub-lattice, and inter-penetrating nature of inorganic and organic sub-lattices explains it inertness against water. In another control experiment, we indeed found that the ground crystal of biphenylmethylammoinum lead iodide does not dissolve in water (**Figure 3-10**).

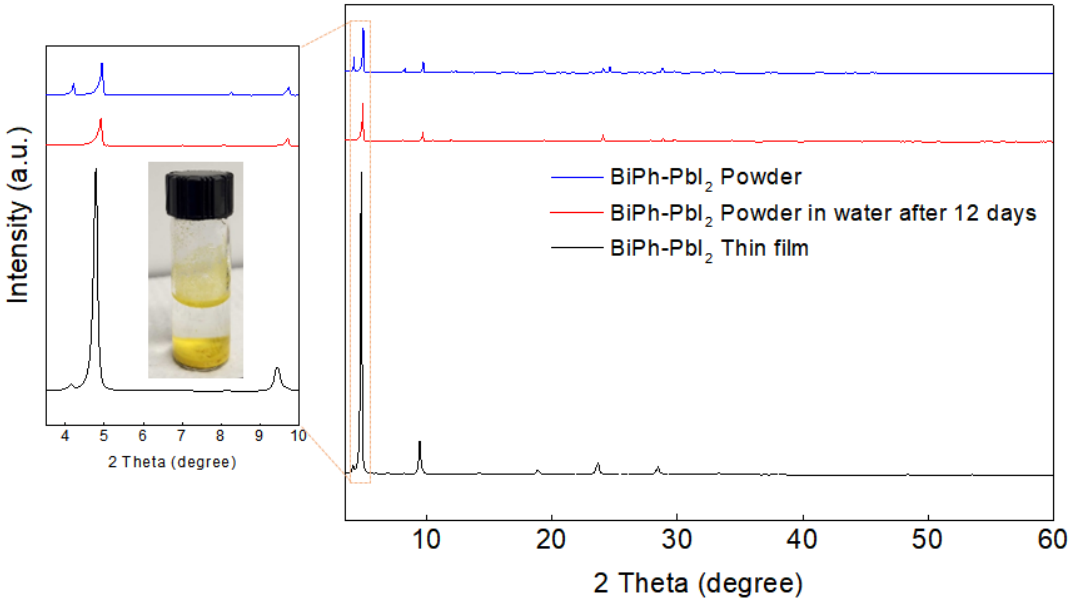

Figure 3-10. XRD patterns of BiPhI-PbI$_2$ powder, BiPhI-PbI$_2$ powder in water after 12 days and BiPhI-PbI$_2$ thin film.

3.3 Conclusions

In summary, we synthesized and employed a novel BiPhI ligand to selectively passivate perovskite GBs. The presence of double benzene rings in BiPhI enables strong passivation of the defects and increases hydrophobicity of the surfaces. PL lifetime results show the increased lifetime of treated perovskite films from 1.0 to 2.7 μs implying the suppression of non-radiative recombination resulting in increased V_{OC}. With this modification, the perovskite film was stable at 87% RH for 6 days and a PCE of 21% was achieved. Our work provides a roadmap for rationally synthesizing new passivation materials for increased stability of the PSCs.

3.3 Experimental

3.3.1 Materials

Indium tin oxide (ITO) coated glass substrates were purchased from Shang Yang Solar (X07-10A). Tin (IV) oxide (SnO_2) 15% in H_2O colloidal dispersion solution was purchased from the Alfa Aesar. Formamidinium iodide (FAI, >99.99%), methylammonium chloride (MACl, >99.99%), and methylammonium bromide (MABr, >99.99%) were purchased from Great Cell, lead (II) iodide (PbI_2, 99.99%) from TCI chemicals, and lead bromide ($PbBr_2$) was purchased from Alfa Aesar. N, N-dimethyl formamide (DMF, 99.5%), dimethylsulfoxide (DMSO, 99.5%), chlorobenzene (99.5%), and acetonitrile (ACN, ≥99.9%) were parched from Milipore Sigma. Sprio-OMeTAD was purchased from Xi'an Polymer Light Technology Co., Ltd. Bis(trifluoromethane)sulfonimide lithium salt (Li-TFSI 99.95%), 4-tert-Butylpyridine (tBP, 98%) and cobalt salt (FK 209 Co (III) TFSI) were purchased from Millipore Sigma.

3.3.2 Preparation of solutions

A 7 ml solution of SnO_2 was prepared by taking 6 ml of deionized (DI) water and 1 ml of SnO_2 15% in H_2O colloidal dispersion nanoparticles with a 6:1 volume ratio. It was sonicated for 30 minutes and filtered with 0.45 μm polyvinylidene difluoride (PVDF) syringe filter before deposition. Perovskite solution based on $FA_{0.95}MA_{0.05}PbI_{2.85}Br_{0.15}$ was prepared by dissolving 217 mg of FAI, 582.7 mg of PbI_2, 7.1 mg of $PbBr_2$, 22 mg of MACl, , and 23.3 mg of MABr in 0.8 ml of DMF and 0.1 ml of DMSO. BiPhI solution was prepared by dissolving it in anhydrous IPA for 2 mg/ml concentration. Spiro solution was prepared by dissolving 0.1 g of spiro-OMeTAD powder in 1.1 ml of chlorobenzene, 0.039 ml of tBP, 0.023 ml of Li-TFSI (pre-dissolved in acetonitrile, 540 mg/mL), and 0.01 ml of Co-complex (pre-dissolved in acetonitrile, 376 mg/mL) solution. All solutions, i.e., perovskite, biphenyliodide and spiro-OMeTAD were filtered with 0.22 µm polytetrafluoroethylene (PTFE) syringe filter.

3.3.3 Synthesis of BiPhX

BiPhI was synthesized as follows: 15 g of 4-Phenylbenzylamine and 50 mL 95% ethanol were added to a 250 mL round bottom flask and put in an ice bath. Then 7.4 mL of HI solution was added slowly over 30 minutes using a dripping funnel while under continuous stirring. After complete addition, the mixture was stirred for another 2 h to maximize the yield. The solvent was then evaporated, and the resulting solid was dissolved in a minimum amount of boiling ethanol. After complete dissolution, the solution was left undisturbed overnight for crystallization. The white BiPhMAI solid crystals were filtered out and washed with diethyl ether and dried under vacuum for more than 24 h. Same procedure was followed to prepare BiPhCl and BiPhBr except hydrochloric acid (HCl) and hydrobromic acid (HBr) were used respectively.

3.3.4 Control experiment

To study reaction between PbI_2 and BiPhI, the powders were mixed in 2:1 molar ratio and grinded together to get the XRD patterns. For the thin films, 1 M solution was prepared in DMF and spin coated on a glass substrate.

To prepare BiPh-PbI_2 single crystals, first we dissolved 4-Phenylbenzylamine in hot HI acid (on hotplate at ~140^oC) to make 1 mole solution and waited until it completely got dissolved. Then, in a 20 ml vial we took 1 M of lead acetate and dissolved in 5 ml of HI acid. We then added this solution to the precursor solution of 4-Phenylbenzylamine and stirred it until it was dissolved. We then slowly cooled the reaction system and observed crystals after ~24 h.

3.3.5 Device fabrication

Glass substrates were sonicated with deionized (DI) water, acetone, and isopropanol, respectively, for 15 minutes. Then, they were dried with N_2 gas gun and were given ozone treatment for ~15 minutes. 0.15 ml of already prepared SnO_2 solution was spin-coated at 3000 rpm for 30 seconds. All the films were then thermally annealed at 150^{o}C for 30 minutes and again given ozone treatment for 30 minutes. A perovskite solution of 75 µl was spin-coated in a three-step process on top of SnO_2 and thermally annealed for 10 minutes for crystallization assisted with dripping of diethyl ether in 3rd step. After that, 0.1 ml of BiPhI solution was spin coated on top of cooled perovskite film at 5000 rpm for 30 seconds. A 75 µl solution of spiro-OMeTAD was deposited with a dynamic spin coating method at 2000 rpm for 30 seconds. A thin layer of ~80 nm of gold was then evaporated on top of the film for front metal connections.

3.3.6 Characterization of thin films

X-ray diffraction (XRD) measurements were done with a PANalytical Empyrean system using a Cu (Kα, 1.5406 Å) source. Scanning electron microscopy (SEM) images were obtained with a Hitachi S-4800 FESEM. Photoluminescence (PL) spectroscopy was carried out by UV-Vis AVENTES spectrometer (AvaSpec-ULS2048CL-EVO-RS) in the reflection mode ranging from 500 to 780 nm in a dark room every 2s. TRPL measurements were performed on an Edinburgh Instruments OB920 Single Photon Counting system. The samples were excited using a 510 nm pulsed laser diode. Emission was collected at 780 nm using a 16 nm bandwidth monochromator.

3.3.7 Characterization of crystals

Single-crystal X-ray diffraction: a crystal was coated in paratone oil, mounted on a MiTeGen Micro Mount, and transferred to the cold stream (150 K) of the X-ray diffractometer. Data was collected on a Bruker Smart instrument equipped with an APEX II CCD area detector fixed at a distance of 5.0 cm from the crystal and a Cu Kα fine focus sealed tube (λ = 1.54178 nm) operated at 1.5 kW (50 kV, 30 mA), filtered with a graphite monochromator. Data was collected at 173 K; the temperature was regulated using an Oxford Cryosystems Cryostream 700.

Chapter 4.

Modified Chemical Bath Deposition of Tin Oxide for All-Scalable $FAPbI_3$ Perovskite Solar Modules

[Reproduced (adapted) with alteration from: ''**Muhammad Awais**, Wanlong Wang, Augusto Amaro, Yameen Ahmed, Mohammad Reza Kokaba, Vishal Yeddu, Dongyang Zhang, I Teng Cheong, Victor Marrugat-Arnal, Nicholas Sandor, Makhsud I. Saidaminov. *Modified Chemical Bath Deposition of Tin Oxide for All-Scalable $FAPbI_3$ Perovskite Solar Modules*. *Advanced Optical Materials*, **2025**, e01353.'']

Contributions to research and writing

In this manuscript, I prepared all samples and developed methods of fabrication of solar cells, carried data collection and data analysis. I also wrote the first draft of the manuscript. The study was supervised by Dr. Makhsud I. Saidaminov.

4.1 Introduction

Perovskite solar cells (PSCs) have received significant attention over the past decade, nearing power conversion efficiencies (PCEs) of 27%.[76,98,207,208] This milestone is attributed to advances in interface engineering,[188,190,209–211] film and ink formulations,[212–214] and design of electron and hole transport layers (ETLs and HTLs, respectively).[215–222] Among various ETL materials, tin oxide (SnO_x) stands out due to its low-temperature processability (~150°C), high bulk electron mobility (~250 $cm^2\ V^{-1}\ s^{-1}$), and suitable energy band alignment, which collectively improve PSC performance.[223,224]

Different SnO_x film fabrication methods have been explored, including deposition of pre-made SnO_x nanoparticles,[225,226] atomic layer deposition,[227,228] magnetron sputtering,[229,230] and chemical bath deposition (CBD).[231,232] Atomic layer deposition and magnetron sputtering are relatively complex and costly techniques.[233] Moreover, the high density of trap states in thus-made SnO_x ETLs adversely impacts the efficiency and stability of PSCs.[234–237] Therefore, CBD SnO_x is emerging as a preferred approach due to its cost-effective precursors and facile preparation instruments, as well as the ability to form dense, uniform, and conformal films.[215,224]

In the CBD of SnO_x, tin(II) chloride dihydrate ($SnCl_2{\cdot}2H_2O$) is typically used as a tin source dissolved in a solution containing water, urea, hydrochloric acid (HCl), and thioglycolic acid (TGA). Urea plays the role of precipitating agent through decomposition to ammonia (NH_3) and release of OH^-. The OH^- reacts with Sn^{2+} to form tin hydroxides, which then readily decompose into SnO_x. The acids act as stabilizers to prevent pre-mature precipitation of tin hydroxides. A precise control of OH^- concentration clearly is critical during the formation of SnO_X, as its sudden increase can trigger rapid hydrolysis and premature precipitation of tin hydroxides into thick, rough, and non-uniform films.[215,238]

$$Sn^{2+} \xrightarrow{[O]} Sn^{4+} \xrightarrow{OH^-} Sn(OH)_4 \xrightarrow{Sn^{2+}} SnO_x$$

Here, we investigated CBD of SnO_x film in the presence of lead chloride ($PbCl_2$) additive, which was selected for two reasons: (1) the added Cl^- will not interfere with the CBD process due to already high Cl^- concentration in the system, and (2) Pb and Sn both belong to Group 14 of the periodic table, which indicates analogous chemical properties.

We hypothesize that during CBD, Pb^{2+} ions from $PbCl_2$ and OH^- ions from urea will remain in solution due to $Pb(OH)_2$ higher solubility product constant (K_{sp} of 1.43×10^{-20}) in water compared to $Sn(OH)_2$ (K_{sp} of 5.45×10^{-27}).[239] This solubility difference allows Pb^{2+} to act as an OH^- scavenger, reducing free excess OH^- concentration and suppressing premature SnO_x precipitation. As a result, smooth, uniform SnO_x films can be formed. We then demonstrate the application of these films in PSCs fabricated under ambient air using scalable processes. Previously reported modified CBD SnO_x-based PSCs typically relied on spin-coating and glovebox fabrication, while our approach achieves efficient devices through a fully scalable, ambient-air fabrication process (**Table 4-1**).

Table 4-1. Performance of PSCs with modified chemical bath deposition of SnOx benchmarked in literature.

Device Structure	**Changes made in SnO_x fabrication**	**Fabrication method**	**PCE (%)**	**Ref.**
FTO/OA-SnO_2/KCl-H_2O_2/$(MAPbBr_3)_{0.008}(FAPbI_3)_{0.992}$/ Spiro-OMeTAD /Au	In-situ modification of CBD	Spin-coating, glovebox	24.60	[240]
FTO/Intermediate-controlled-CBD/$Cs_{0.05}(FA_{0.83}MA_{0.17})_{0.95}Pb(I_{0.83}Br_{0.17})_3$/Spiro-OMeTAD /Au	In-situ modification of CBD	Spin-coating	23.17	[241]
FTO/CBD-SnO_2/2D-3D PVK/ MOAI /Spiro-OMeTAD /Au	CBD duration optimization	Spin-coating	23.70	[242]
FTO/SnO_2-Li/$CsFAPbI_3$/Spiro-OMeTAD/Au	In-situ modification of CBD by Li	Spin-coating, glovebox	22.24	[243]
FTO/SnO_2-Co/$FAPbI_3$/Spiro-OMeTAD/Ag	In-situ modification of CBD by Co	Spin-coating, glovebox	24.20	[217]
FTO/SnO_2-$PbCl_2$/$FAPbI_3$/Spiro-OMeTAD/Au	In-situ modification of CBD by $PbCl_2$	All-scalable, ambient air	24.50	This work

4.2 Results and discussion

4.2.1 Investigation of tin oxide film formation and its properties

We prepared SnO_x films on indium doped tin oxide (ITO) by conventional CBD (C-SnO_x, where C stands for control sample) and CBD with $PbCl_2$ additive in the precursor solution (T-SnO_x, where T stands for target sample) (see Methods section for details). Freshly made CBD solutions were clear, which then turned turbid over time as SnO_x started to form (**Figure 4-1**). We did not observe significant differences in the turbidity of the control and target CBD solutions (**Figure 4-1**), as well as in the thickness of SnO_x films over time as determined by ellipsometry (**Figure 4-2**).

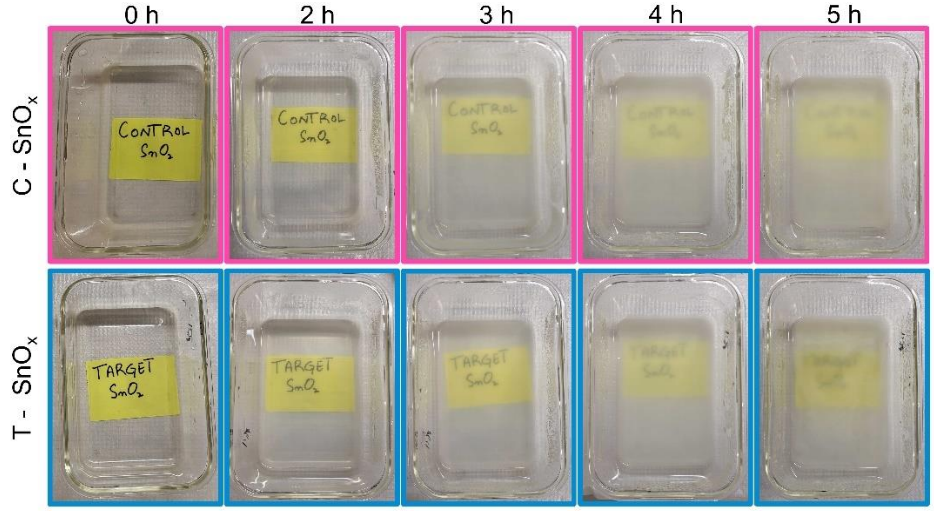

Figure 4-1. Snapshots of chemical bath deposition (CBD) of SnO_x films.

To investigate the role of $PbCl_2$ (20 mg/ml, see experimental section for details) in CBD, we measured the *pH* of both control and target CBD solutions (**Table 4-2**). The *pH* of as-made control CBD solution was 1.17, which dropped to 1.06 after 5 hours; in contrast, the *pH* of target CBD dropped only slightly (from 1.13 to 1.10) within the same period, indicating minimum CBD fluctuation conditions.

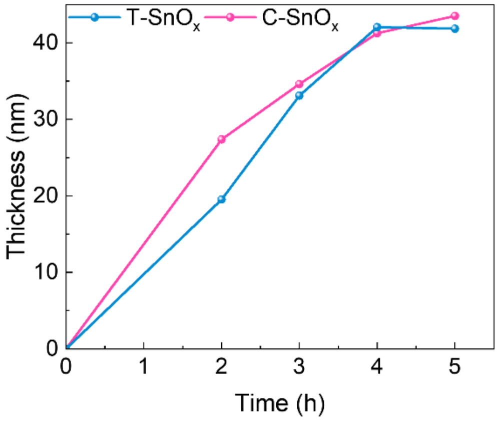

Figure 4-2. Thickness of tin oxide films as a function of time of CBD.

We also performed an additional experiment by adding only $PbCl_2$ to the CBD solution ($PbCl_2$, urea, stabilizing acids, *without* $SnCl_2 \cdot 2H_2O$). This solution showed a *pH* of 1.97 as made, and 1.88 after 5 hours, indicating over 6-fold ($10^{-(14\text{-pH\_PbCl2\_only})}/10^{-(14\text{-pH\_control\_CBD})}$) higher concentration of OH^- as compared to control CBD. Despite this high OH^- concentration, the $PbCl_2$-only solution did not show any sign of precipitation after 5 hours at 80 °C (while control and target CBD solutions turned turbid, as discussed above). This is because $Pb(OH)_2$ is nearly two orders of magnitude more soluble than $Sn(OH)_2$ counterparts, as discussed above.

Table 4-2. Measured *pH* of solutions at room temperature.

Sample	**As prepared**	**After 5 hours**
Control CBD (SnCl₂·2H₂O, urea, HCl, TGA)	1.17	1.06
Target CBD (+ PbCl₂)	1.13	1.10
PbCl₂-only (PbCl₂, urea, HCl, TGA; no SnCl₂·2H₂O)	1.97	1.88

Despite no noticeable visual differences were observed during film formation, we investigated the impact of $PbCl_2$ on tin oxide film composition using X-ray photoemission spectroscopy (XPS). The absence of characteristic Pb $4f_{7}/_{2}$ and $4f_{5}/_{2}$ peaks at 138.9 eV and 143.8 eV in the survey spectra suggests minimal incorporation of Pb into the films.[244] A broad feature near 140 eV, observed across all SnO_x samples—including those prepared without $PbCl_2$ — was attributed to the Sn 4s orbital rather than Pb (**Figure 4-3**). High-resolution Sn $3d_{5}/_{2}$ spectra revealed a shift to higher binding energy in T-SnO_x and C-SnO_x films compared to that conventionally blade-coated SnO_x nanoparticle (N-SnO_x), which indicates higher degree of Sn^{2+} oxidation in the CBD-derived films (**Figure 4-4A-C**).

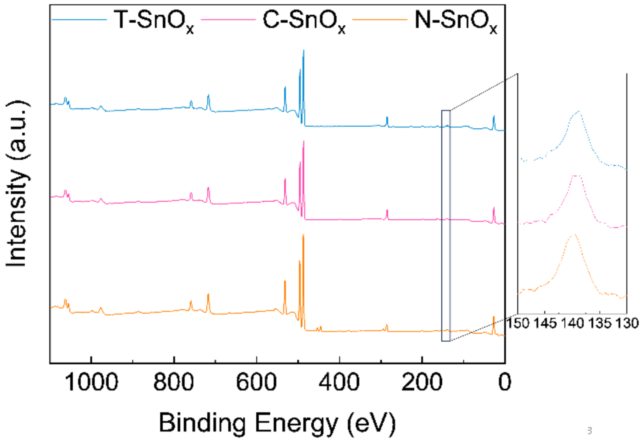

Figure 4-3. Survey XPS spectra of tin oxide films.

The XPS peak deconvolution and area analysis (**Table 4-3**) were used to quantify the relative amounts of Sn^{2+} and Sn^{4+}, allowing estimation of the films' brutto-formula. The T-SnO_x showed the highest level of Sn^{4+} with an estimated formula of $SnO_{1.55}$ ($[Sn(II)O]_{0.45}[Sn(IV)O_2]_{0.55}$), followed by C-$SnO_x$ ($SnO_{1.53}$ or $[Sn(II)O]_{0.47}[Sn(IV)O_2]_{0.53}$), and N-$SnO_x$ ($SnO_{1.41}$ or $[Sn(II)O]_{0.59}[Sn(IV)O_2]_{0.41}$). To quantify the relative contribution of adsorbed and lattice oxygen in the tin oxide films,[245] we deconvoluted O 1s XP spectra (**Figure 4-5**). The ratio of adsorbed oxygen O_x^- (O^- and O_2^-) to the lattice oxygen ($Sn^{2+}O$ and $Sn^{4+}O_2$) was 1.16 for C-SnO_x (**Table 4-4**), notably higher than that for T-SnO_x (0.94).[246,247]

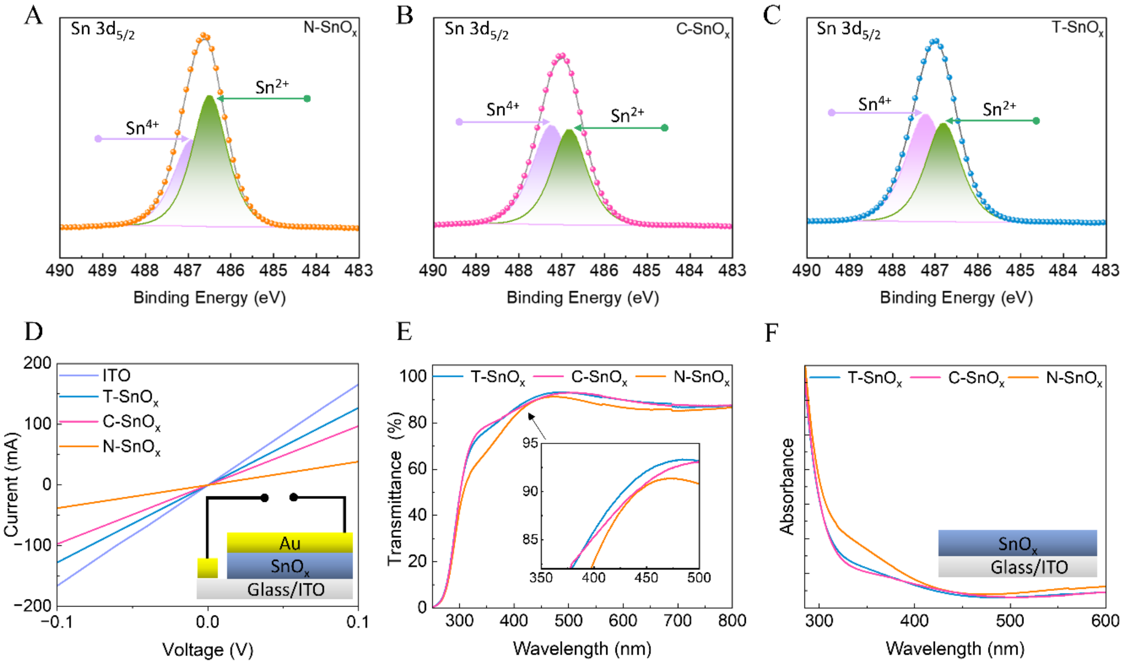

Figure 4-4. Characterization of tin oxide films. (A-C) XPS spectra of Sn $3d_{5/2}$. (D) Current-voltage characteristics of ITO/SnO_x/Au stacks after 30 days of aging. (E) light transmittance, and (F) light absorbance spectra.

Table 4-3. Portion of XPS Sn peak corresponding to Sn^{2+} and Sn^{4+} in tin oxide films.

Sample	**Sn^{2+}**	**Sn^{4+}**	**Chemical Composition**
N-SnO_x	59.2	40.7	$[Sn(II)O]_{0.59}[Sn(IV)O_2]_{0.41}$
C-SnO_x	46.53	53.46	$[Sn(II)O]_{0.47}[Sn(IV)O_2]_{0.53}$
T-SnO_x	45.34	54.65	$[Sn(II)O]_{0.45}[Sn(IV)O_2]_{0.55}$

This indicates a greater degree of oxygen deficiency in the control CBD sample; such oxygen vacancies are known to introduce energy states in bandgap that can impact their electronic properties for device applications.[248,249] The reduced oxygen vacancy concentration in T-SnO_2 can be attributed to the controlled hydrolysis enabled by $PbCl_2$ in the CBD process as discussed above, which results in smooth and uniform films, effectively suppressing the oxygen vacancies.[250]

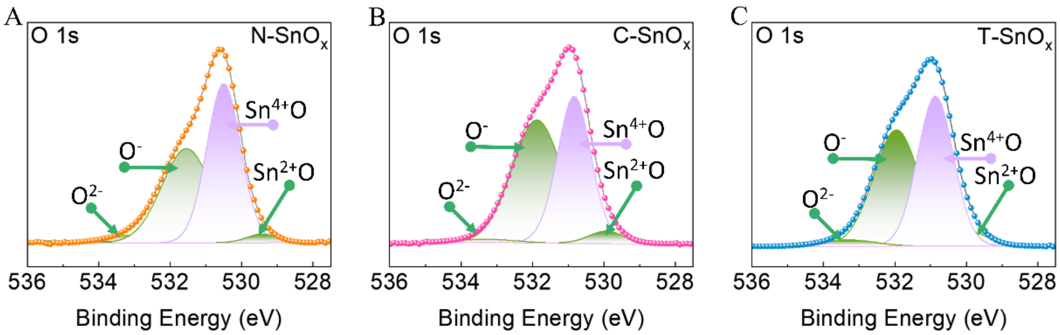

Figure 4-5. XPS spectra of O 1s for tin oxide films. (A) N-SnO_x, (B) C-SnO_x, (C) T-SnO_x.

Table 4-4. Summary of XPS peak area corresponding to adsorbed and lattice oxygen.

Sample	$Sn^{2+}O$	$Sn^{4+}O_2$	O^-	O^{2-}	Peak area ratio $(O^-+O^{2-})/(Sn^{2+}O+Sn^{4+}O)$
N-SnO_x	515.4	10573.6	9116.4	1023.4	0.91
C-SnO_x	612.6	6860.7	8454.3	253.5	1.16
T-SnO_x	881.7	7422.4	7353	493.4	0.94

To study the films' electrical properties, we fabricated ITO/SnO_x/Au stacks and measured their current-voltage (*IV*) characteristics at dark. All SnO_x showed the same electrical resistivity (**Figure 4-6**); however, the resistivity of N-SnO_x increased over time (**Figure 4-4D**) likely due to moisture absorption given its inherent porous nature.[251,252]

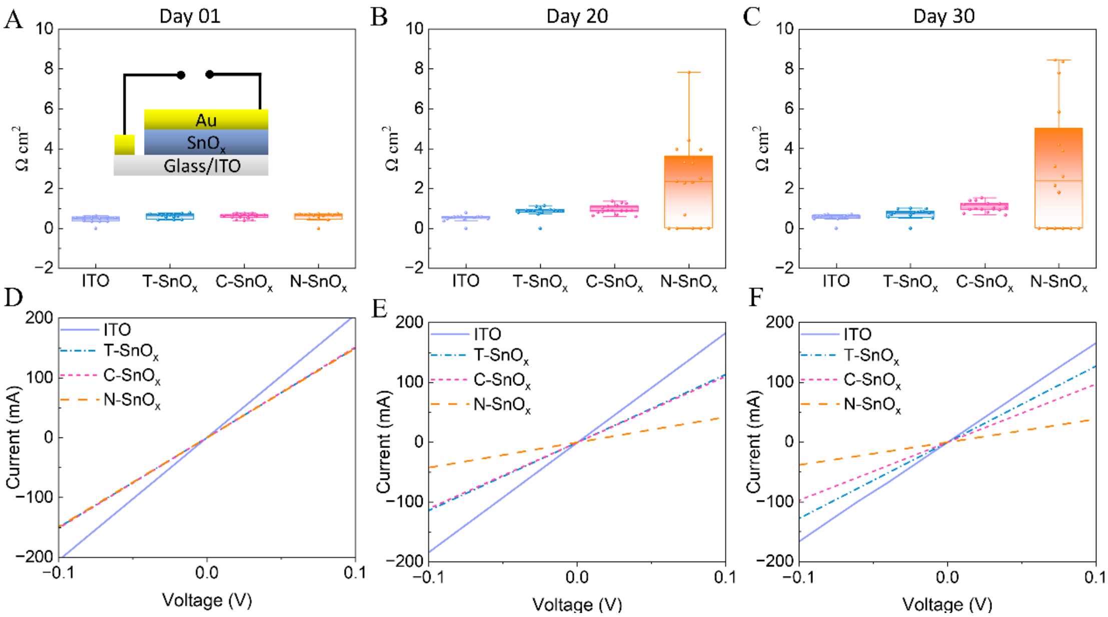

Figure 4-6. Electrical resistivity of the samples measured over time for tin oxide films: (A) Day 1, (B) Day 20, (C) Day 30, and current-voltage characteristics of ITO/SnO$_x$/Au stacks (D) Day 1, (E) Day 20, (F) Day 30.

We then measured the films' surface morphology with atomic force microscopy (AFM). The AFM images showed low roughness of N-SnO$_x$ (average RMS of ~1.6 nm) compared to ~20.4 nm for C-SnO$_x$ and ~11 nm of T-SnO$_x$ (**Figure 4-7**).

Next, we studied the optical properties of the films. The light transmittance spectra show that CBD-made SnO$_x$ films transmit more light, particularly between 370 – 500 nm wavelengths (**Figure 4-4E**), which was further supported by UV-Vis absorption spectra (**Figure 4-4F**).

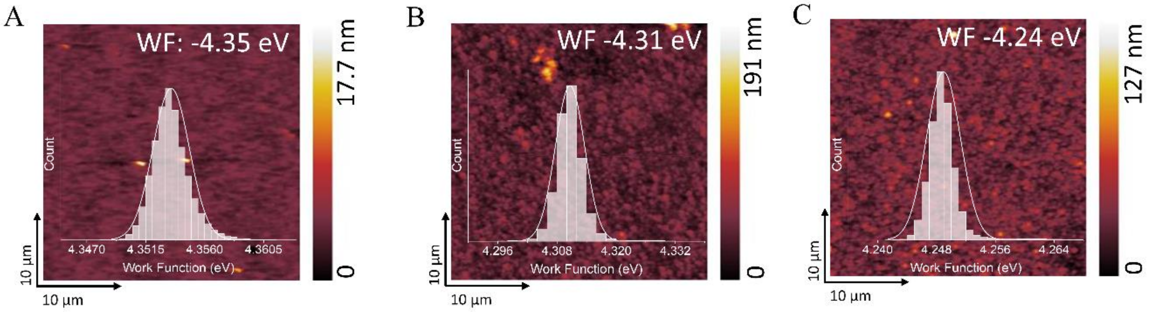

Figure 4-7. AFM images and work function distribution of (A) N-SnO_x, (B) C- SnO_x, (C) T-SnO_x. The inset in each image shows the respective work function distribution.

Taken together, we conclude that the $PbCl_2$ in SnO_x CBD solution acts as a controllable source of OH^-, enabling moderate increase of its concentration; in the meantime, Pb^{2+} can prevent premature over-generation of OH^- through the formation of $Pb(OH)_2$, which will remain in solution due its high solubility. This leads to T-SnO_x film with higher degree of Sn^{4+} content, and concurrently reduced density of oxygen vacancies.

4.2.2 Investigation of half-cells (perovskite/tin oxide stacks)

We then fabricated half-cells by depositing formamidinium lead iodide ($FAPbI_3$, where FA stands for $CH(NH_2)_2^+$) perovskite on ITO/SnO_x; the perovskite films were blade coated in ambient air following our recent work.[82] The stacks were then subjected to heat stress at 85 °C in ambient air at 40-50% relative humidity (RH): the perovskite film deposited on T-SnO_x remained black after 140 hours, while perovskite films on C-SnO_x and N-SnO_x showed discoloration (**Figure 4-8A**).

To understand the origin of improved stability of perovskite films on T-SnO_x, we performed scanning electron microscopy (SEM) (**Figure 4-8B-D**) on fresh perovskite films fabricated in ambient air. Grain boundaries are known to induce perovskite film degradation; hence boundaries must be minimized by increasing grain size. The grain size histogram of all the three perovskite films, as extracted from SEM, showed that the perovskite on T-SnO$_x$ was made of large grains of 1.96 µm on average compared to 1.52 µm on N-SnO$_x$ (**Figure 4-9**). In addition, N-SnO$_x$ film showed large pinholes on the film surface (**Figure 4-8A**), which are detrimental to the stability and performance of perovskite films.

We then investigated the photophysical properties of perovskite films on SnO$_x$ films by assessing their radiative recombination decay via steady state and time resolved photoluminescence (TRPL) spectroscopy (**Figure 4-8E, F**). We observed a fast TRPL decay for perovskite on T-SnO$_x$ ($\tau_{ave} = 19.7\, ns$), significantly faster than those for perovskite films on C-SnO$_x$ ($\tau_{ave} = 47.8\, ns$) and N-SnO$_x$ ($\tau_{ave} = 94.8\, ns$). Steady-state photoluminescence spectra also showed significant quenching of perovskite emission on T-SnO$_x$ compared to those on N-SnO$_x$ and C-SnO$_x$. These results indicate improved extraction of excited charge carriers and reduced detrimental interfacial trap states by the T-SnO$_x$.

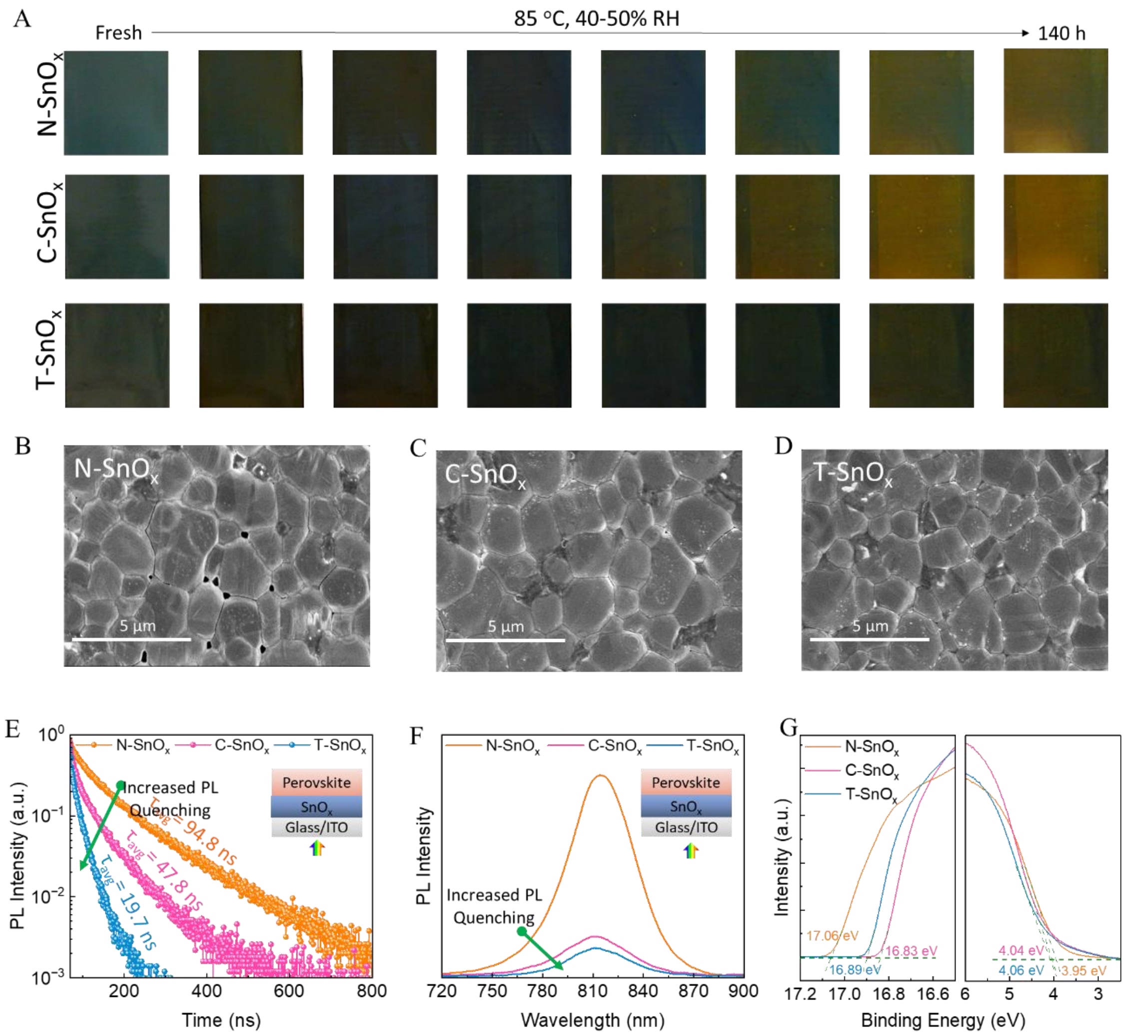

Figure 4-8. Characterization of ITO/SnO_x/$FAPbI_3$ stacks. (A) Digital photography images of the stacks before and after heat stress at 85 °C and 40-50% RH in ambient air. (B-D) Scanning electron microscope (SEM) images of fresh perovskite films on N-SnO_x, C-SnO_x, and T-SnO_x. (E) TRPL decay, and (F) PL spectra of stacks. (G) UPS spectra of ITO/SnO_x films stack.

To assess energy band alignment of SnO_x films with perovskite, we performed ultraviolet photoelectron spectroscopy (UPS) of tin oxide films (**Figure 4-8G**). The results showed that both C- SnO_x and T-SnO_x exhibit deeper conduction band minima (CBM) compared to N-SnO$_x$, which can provide a stronger driving force for electron extraction from the overlying perovskite absorber (**Figure 4-10**). Notably, T-SnO$_x$ demonstrated a CBM position that is better aligned with that of the perovskite, which is expected to contribute to enhanced photovoltage. This improved alignment is likely due to the lower concentration of oxygen vacancies in T-SnO$_x$, which reduces defect-induced band bending and brings its CBM closer to that of the perovskite.[253,254]

Interestingly, the work functions (WFs) measured by UPS and kelvin probe force microscopy (KPFM) for films made by CBD (C-SnO$_x$ and T-SnO$_x$) are consistent, suggesting stable surface properties. In contrast, the film made from nanoparticles (N-SnO$_x$) shows a higher WF when measured by KPFM, likely due to adsorption of water and oxygen during the ambient-air measurement.[255,256]

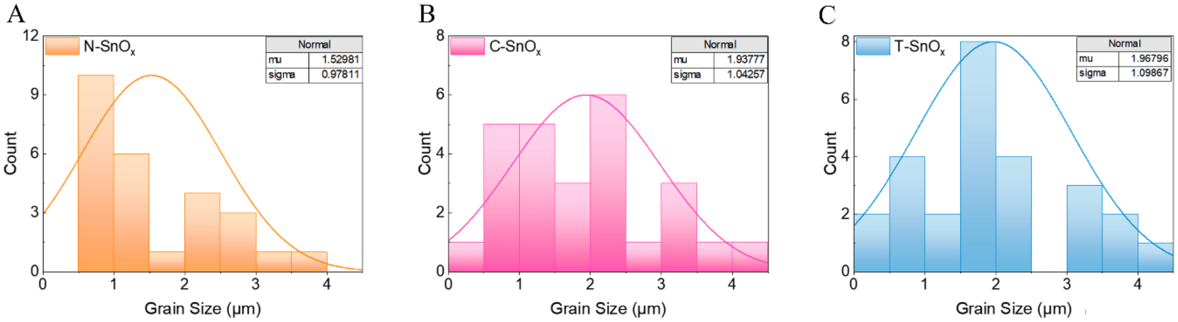

Figure 4-9. Histogram of grain size of FAPbI$_3$ films on tin oxide films, (A) N-SnO$_x$, (B) C-SnO$_x$, (C) T-SnO$_x$.

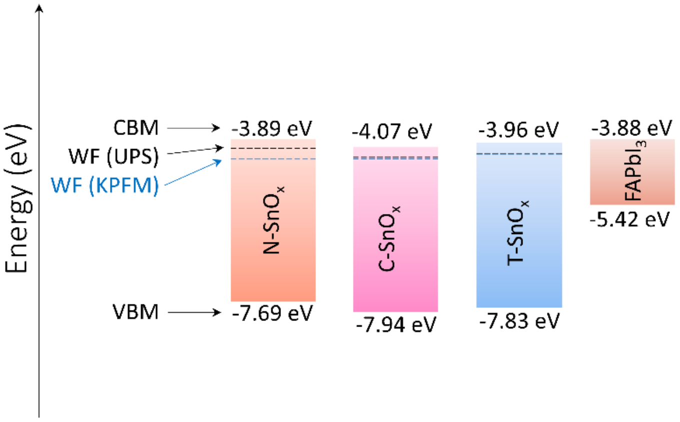

Figure 4-10. Energy band diagram of tin oxide films determined from UPS results.

We then measured the dark current-voltage characteristics of the electron only devices (ITO/SnO$_x$/ FAPbI$_3$/[6,6]-phenyl-C(61)-butyric acid methyl ester (PCBM)/Au) (**Figure 4-11**) and calculated their trap density using space charge limited current (SCLC) method.[257]

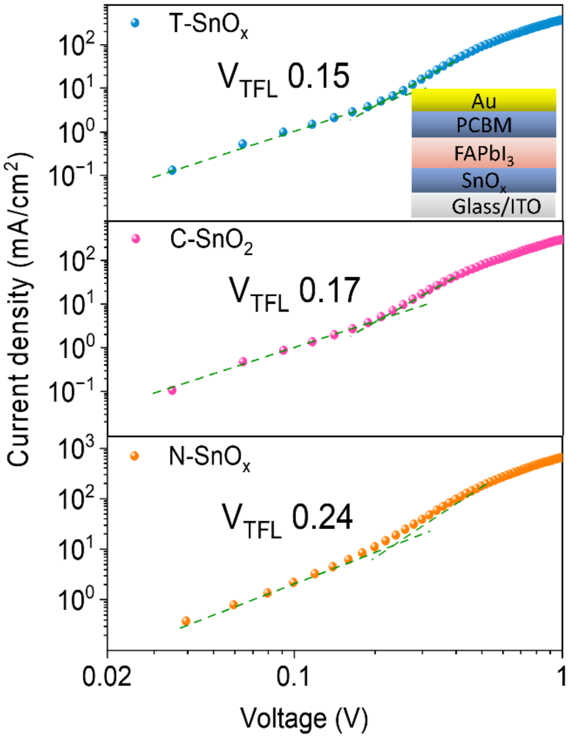

Figure 4-11. Current-voltage characteristics of electron-only stack (ITO/SnO$_x$/FAPbI$_3$/PCBM/Au).

The current injection increased sharply with the bias voltage, indicating the onset of trap-filling regime. The point, also known as trap-filling limit voltage (V_{TFL}), allowed us to estimate trap density (N_d) in the stacks following this relation: $v_{TFL} = \frac{eN_dL^2}{2\varepsilon\varepsilon_0}$, where e presents the elementary charge, L is the thickness of the perovskite films, ε stands for the relative dielectric constant (46.9 for $FAPbI_3$)[258] and ε_0 is the vacuum permittivity (8.85 × 10^{-12} $F\ m^{-1}$). The electron trap density was thus calculated to be 2.59 × 10^{15} cm^{-3} for T-SnO_x, 2.94 × 10^{15} cm^{-3} for C-SnO_x, and 4.15 × 10^{15} cm^{-3} for N-SnO_x stacks. The reduced trap density of stacks with T-SnO_x can be attributed to improved SnO_x/perovskite interface, likely due to formation of an intimate contact with T-SnO_x, which we found to be more hydrophilic than the other tin oxide films (**Figure 4-12**).

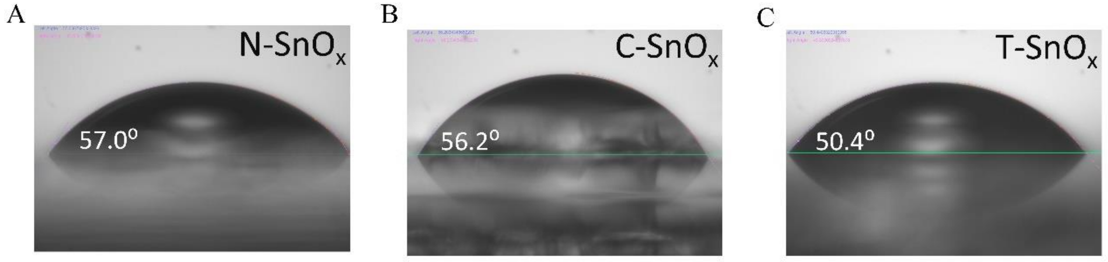

Figure 4-12. Water droplet/tin oxide film contact angle measurements, (A) N-SnO_x, (B) C-SnO_x, (C) T-SnO_x.

4.2.3 Perovskite solar cells

Next, we fabricated PSCs and modules with these SnO_x films via blade coating perovskite and HTLs in ambient air, and physical vapor deposition of counter electrode. The PSCs fabricated on T-SnO_x (see experimental section for preparation method, and **Figure 4-13** for optimization of $PbCl_2$ concentration) demonstrated champion PCE of 24.5%

compared to 22.3% for C-SnO$_x$ (**Figure 4-14A**) for 0.049 cm^2 device active area. The J$_{SC}$ values extracted from current-voltage characteristic and external quantum efficiency (EQE) spectrum of T-SnO$_x$-based PSC aligned well (**Figure 4-15**).

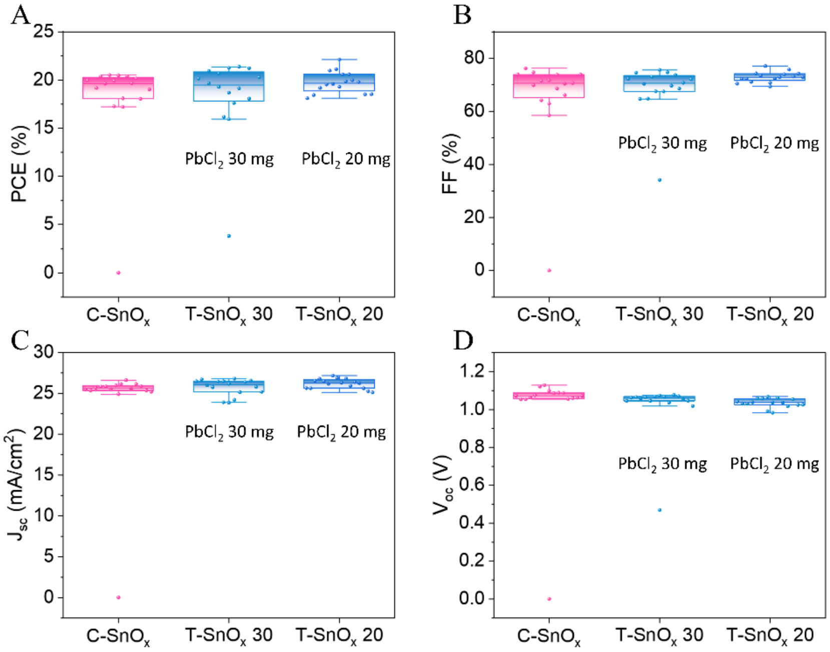

Figure 4-13. Optimization of PbCl$_2$ concentration. Here C-SnO$_x$ (without PbCl$_2$) is compared with addition of 30 mg (T-SnO$_x$ 30) and 20 mg (T-SnO$_x$ 20) PbCl$_2$ into respective precursor solutions to optimize the concentration of PbCl$_2$. A) PCE, B) FF, C) J$_{SC}$, and D) V$_{OC}$.

The statistical analysis of PSCs fabricated on T-SnO$_x$ showed higher average PCE of 22.0% than its counterpart (C-SnO$_x$) with an average PCE of 19.7% (**Figure 4-14B**). The main contribution for the increase in PCE originated from open circuit voltage (V$_{OC}$) and fill factor (FF) which we attribute to decreased non-radiative recombination and intimate T-SnO$_x$/perovskite interface as discussed above. The V$_{OC}$ x FF product shows that the T-SnO$_x$ achieved 83.4% of its Shockley-Quiesser limit for a 1.5 bandgap perovskite (**Figure 4-14C**).

The efficiency distribution across a substrate of 75×32.5 mm with 16 cells (0.049 cm^2 active cell area) was uniform and homogenous (**Figure 4-16**) with a median of 22.09% and a standard deviation of 1.96% for T-SnO_x (**Figure 4-17**). Inspired by this, we pursued to fabricate perovskite mini modules of 10.23 cm^2 size, which showed a PCE of 17.8% (**Figure 4-14D**).

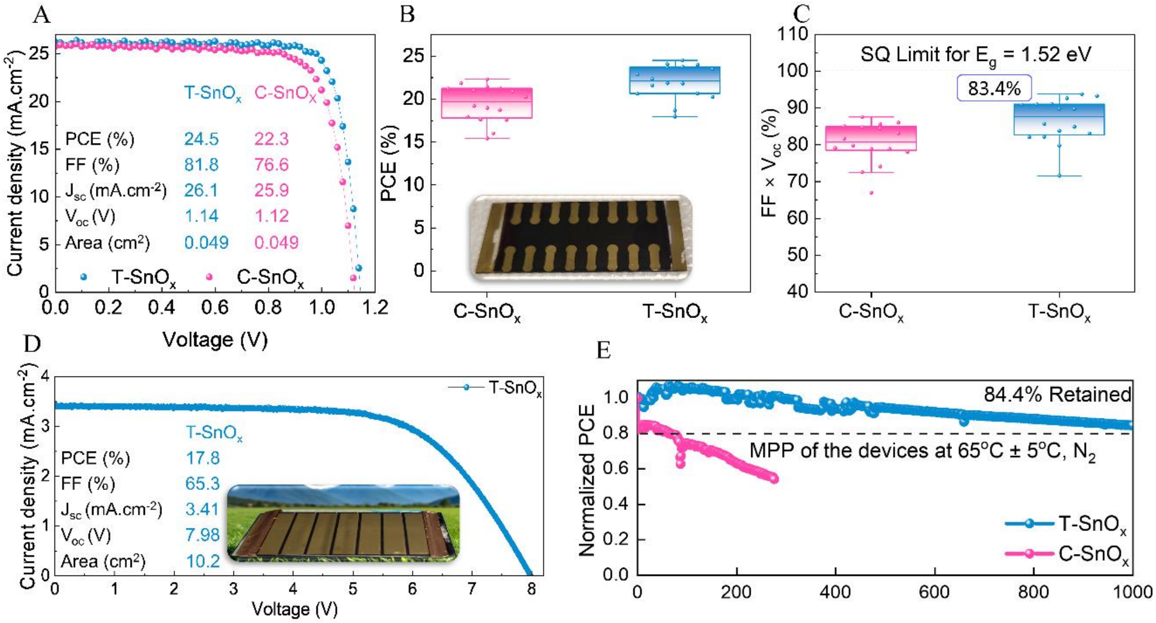

Figure 4-14. Characterization of perovskite solar cells**.** (A) Current-voltage characteristics of champion sells. The inset table shows the photovoltaic parameters of each device. (B,C) Whisker box plots of the devices showing statistical PCE and V_{OC} x FF product. (D) Current-voltage curve of perovskite solar mini module. The inset shows the photovoltaic parameters of the module and its image. (E) Stability of PSCs at MPPT fabricated on both T-SnO_x and C-SnO_x with PTAA as a hole transport layer.

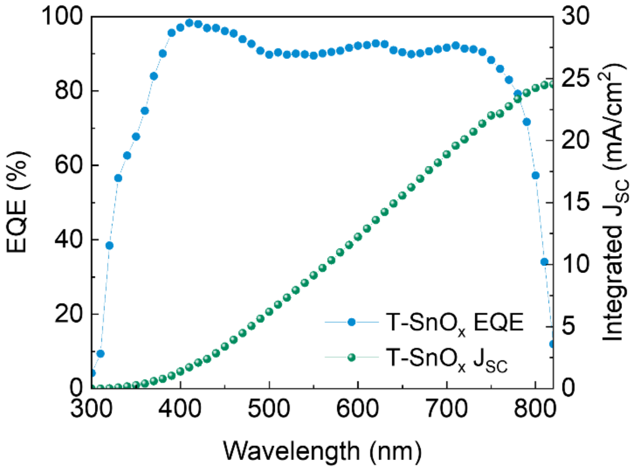

Figure 4-15. EQE of a PSC with T-SnO$_x$.

To study the stability of PSCs, we performed maximum power point tracking (MPPT) of an encapsulated device. We note that for the MPPT and stability tests at elevated temperatures, the 2,2',7,7'-Tetrakis[N,N-di(4-methoxyphenyl)amino]-9,9'-spirobifluorene (spiro-OMeTAD) was replaced with poly(triaryl amine) (PTAA) as an HTL, as the former is known to degrade under external stressors.[259–262] The encapsulated devices were measured at ~65±5 ˚C showing an initial PCE increase likely due to temperature healing of interfaces. The T-SnO$_x$-based device retained 84.4% of its initial PCE after 1,000 hours under MPPT conditions, demonstrating excellent operational stability. In contrast, the C-SnO$_x$-based device exhibited rapid degradation, retaining only 54% of its initial PCE after just 138 hours (**Figure 4-14E**).

Furthermore, the devices were subjected to thermal stress at 85 °C and their PCE was tracked over time. The T-SnO$_x$-based solar cell retained 87.9% of its initial efficiency after >800 hours of the thermal stress compared to 64.7% for the C-SnO_x-based and 68.3% for N-SnO_x-based devices (**Figure 4-18**).

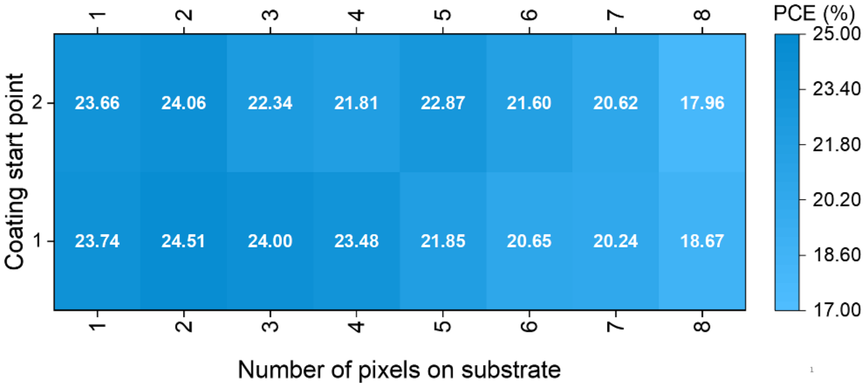

Figure 4-16. PCE distribution across the 75*32.5 mm device with 16 pixels fabricated on T-SnO_x.

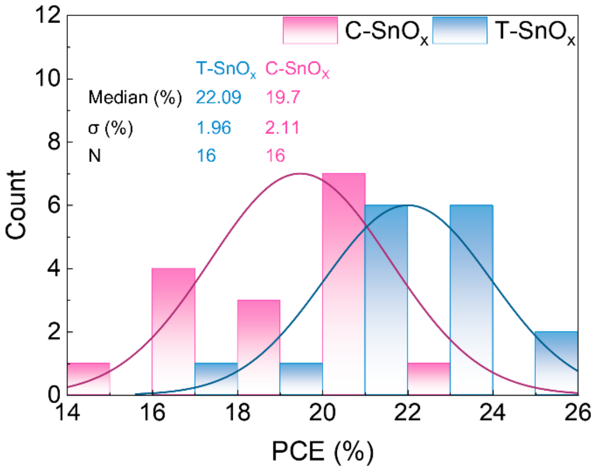

Figure 4-17. Histogram of PCE distribution across 75×32.5 mm devices with 16 cells (σ, N stand for standard deviation and number of samples, respectively).

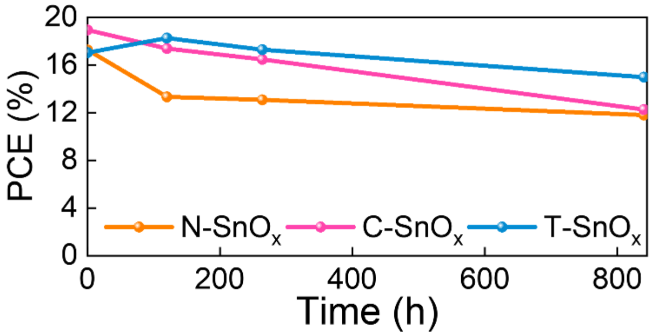

Figure 4-18. Stability of the devices at 85 °C measured for over 800 h with PTAA as HTL in N_2.

4.3 Conclusions

In conclusion, we studied CBD of SnO_x, finding that the presence of $PbCl_2$ can scavenge the excess OH^- supply and ensure a smooth and conformal deposition of SnO_x. The SnO_x film exhibited high degree of conversion of Sn(II) to Sn(IV), reduced concentration of oxygen vacancies, as well as high optical transparency and electrical conductivity. Perovskite film deposited on the SnO_x showed resilience against harsh environmental conditions (85 °C and 40-50% relative humidity), pinhole-free morphology, reduced trap density and fast charge extraction dynamics. PSCs based on the SnO_x achieved a PCE of 24.5%, along with excellent stability for over 1,000 hours under MPP tracking conditions. This study underscores the importance of controlling the CBD reaction environment to produce uniform SnO_x films critical for the fabrication of efficient, stable, and scalable perovskite solar modules.

4.4 Experimental

4.4.1 Materials and facilities

Indium doped tin oxide (ITO) coated glass substrates were purchased from Shang Yang Solar (X07-10A). Formamidinium iodide (FAI, > 99.99%), and methylammonium chloride (MACl, >99.9%) were purchased from Greatcell Solar. Tin (IV) oxide, 15% in H_2O colloidal dispersion nanoparticles were purchased from Thermo Fisher Scientific. 2-Methoxyethanol (2-ME, anhydrous, >99.8%), anhydrous chlorobenzene (CB), *N*-Methyl-2-pyridone (NMP, ≥ 99%) and tin (II) dihydrate ($SnCl_2.2H_2O$, >99.97 %), thioglycolic acid (98%), hydrochloric acid (≥ 37% concentrated), urea (≥ 99%), potassium chloride (KCL, 99.99%), bis(trifluoromethane)sulfonimide lithium salt (Li-TFSI 99.95%), 4-tert-Butylpyridine (tBP, 98%), N-octylammonium iodide (OAI) and cobalt salt (FK 209 Co (III) TFSI) were purchased from Millipore Sigma. PbI_2 (> 99.99%) was purchased from TCI (Tokyo Chemical Industry). Spiro-OMeTAD was purchased from Xi'an Polymer light technology Corp. All chemicals were used without any purification.

4.4.2 $FAPbI_3$ crystal growth

$FAPbI_3$ single crystals were grown by Inverse Temperature Crystallization.[263] FAI and the appropriate ratio of PbI_2 (1:1) was dissolved in 2ME solvent to prepare a 0.8 M $FAPbI_3$ solution. 3 ml of the precursor solution was filtered through a 0.2 µm polytetrafluoroethylene (PTFE) syringe filter and transferred to a 4-dram glass vial. The solution was then heated at 120 °C until it has visibly converted to black single crystals (usually 3-4 hours). After the single crystal formation, the crystals were removed from the solution and quickly dried using Kimwipes. To ensure the complete removal of 2ME from the surface, the crystals were annealed at 150 °C for 30 min and further dried under the vacuum overnight. The obtained crystals were further milled using a clean pestle and mortar before use. The obtained crystals were stored in a vacuum sealed bag over the period of usage.

4.4.3 Preparation of solutions

1 M $FAPbI_3$ solution was prepared by dissolving $FAPbI_3$ single crystals with MACl (30 mol% rel. to FAPI) in 2ME, L-α-phosphatidylcholine (2.5 mg/ml in 2ME) and NMP (50 mol% rel. to Pb) were added to the precursor before use to improve the uniformity and coverage. For all films, extra 5 mol% of PbI_2 was added to the precursor. OAI as a passivation solution was prepared by dissolving it in anhydrous IPA for 2 mg/ml concentration. Spiro-OMeTAD solution was prepared by dissolving 0.1 g of spiro-OMeTAD powder in 1.1 ml of chlorobenzene, 0.039 ml of tBP, 0.023 ml of Li-TFSI (pre-dissolved in acetonitrile, 540 mg/mL), and 0.01 ml of Co-complex (pre-dissolved in acetonitrile, 376 mg/mL) solution. PTAA solution was prepared by dissolving 30 mg PTAA in 1 ml chlorobenzene with 3 mg TPFB additive. All solutions, i.e., perovskite, OAI and spiro-OMeTAD were filtered with 0.22 µm PTFE syringe filter before use. A 7 mL solution of SnO_x nanoparticle was prepared by taking 6 mL of deionized (DI) water and 1 mL of SnO_x 15% in H_2O colloidal dispersion nanoparticles with a 6:1 volume ratio. It was sonicated for 30 min and filtered with 0.45 µm polyvinylidene difluoride (PVDF) syringe filter before deposition.

4.4.4 Chemical bath deposition (CBD) of SnO_x layer

The ITO substrates were wiped with Berkshire microfiber polyester and isopropyl alcohol. The CBD solution was prepared by mixing 750 mg of urea, 750 µL of HCl, 15 µL of TGA, and 164 mg of $SnCl_2·2H_2O$ per 60 mL of DI water. For the target CBD, we added 20 mg of $PbCl_2$ (per 60 mL water) in the precursor solution in addition to the above chemicals. We deposited SnO_x on a whole substrate as well as taped edges of the ITO substrate with a Kapton tape to prevent deposition of SnO_x on the edges. We did not notice any significant difference in device performance and continued depositing the ITO substrates without covering edges. Eight ITO (32.5*75 mm) substrates were cleaned and dipped horizontally into CBD solution without UV-ozone treatment and reacted at 80 °C until the solution turns murky which approximately took 5 hours. The pH was measured with SevenCompact pH meter by Mettler Toledo. After the reaction is complete, the SnO_x deposited ITO substrates were removed from the reaction bath and cleaned via sonication with ethanol for 5 min. After cleaning, the substrates were annealed at 150 ℃ for 1 hour.

4.4.5 Device fabrication

The ITO/SnO_x coated substrates were UV-ozone treated for 15 mins. The KCl layer was coated on top of ITO/SnO_x coated substrate by blade coating (ZAA 2300 ZEHNTNER GmbH Testing Instrument) with a gap height of 350 µm at 70 °C base heat and a speed of 5 mm/s. The perovskite layer was blade coated and dried with an air knife blowing N_2 at room temperature. The gap height between the substrates and applicator was set as 200 µm with a speed of 10 mm/s. The perovskite films were annealed at 150 °C for 30 mins after coating. After that, OAI as a passivation layer was deposited on top of perovskite films with the gap height of 275 µm at 60 °C base heat and a speed of 30 mm/s and were annealed at 100 ℃ for 10 mins. The obtained films were cooled down to the room temperature and the spiro-OMeTAD layer was deposited on top of films by blade coating method at 50 °C at a speed of 30 mm/s. For stability tests, spiro-OMeTAD was replaced with PTAA: PTAA solution was blade coated at a speed of 30 mm/s, with a gap height of 150 µm, using a base heat of 57.2 ˚C, as detailed elsewhere.[264] Finally, 80 nm gold was deposited by thermal evaporation (Angstrom Engineering Inc.) to assemble an *n*-*i*-*p* configuration device.

4.4.6 Module fabrication

P1 scribing was performed by Shang Yang Solar using a pulsed laser with a 1,064 nm wavelength, 50 nanosecond pulse duration, speed of 300 mm/s, power of 6.7 watts, 50 kHz frequency and a cut width of 50 µm. For P2 scribing, a Trotec Speedy 360 CO_2 laser emitting a 10 µm wavelength beam was utilized. The scribing parameters for P2 included a speed of 17.75 cm/s, power of 7.8 Watts, pulse per inch (PPI) of 1000, and a width of 200 µm. Finally, P3 involved depositing a 80 nm thick gold electrode with a width of 1 mm using a deposition mask in a vacuum thermal evaporation system by Angstrom Engineering Inc. under a vacuum of 10^{-6} Torr.

4.4.7 Characterization and measurements

SEM images were collected by a Hitachi S-4800 field scanning electron microscope. The thickness and growth rate of the CBD SnO_x films were determined using spectroscopic ellipsometry (Alpha-SE, J.A. Woollam Co.). A modified Cauchy model, based on the equipment's library model, was applied to fit the optical data obtained for the SnO_x films. This approach allowed precise extraction of film thickness and optical constants while accounting for the material's dispersion behavior in the measured wavelength range. X-ray photoelectron spectroscopy (XPS) was performed in nanoFAB (University of Alberta) on a Kratos Axis Ultra X-ray Photoelectron Spectrometer with a monochromatic Al Kα source under high vacuum (10^{-10} mbar). X-ray diffraction patterns were carried out using a PANalytical Empyrean system with Cu Kα radiation (1.5406 Å). Absorption spectra were measured using an ultraviolet/visible spectrometer (Lambda 1050, PerkinElmer). Time-resolved photoluminescence (TRPL) was conducted using an Edinburgh OB920 system with 405 nm pulsed excitation. Photovoltaic parameters were measured with a Newport Oriel sol-3A (class AAA) solar simulator under Air Mass (AM) 1.5G illumination and an Ossila Source Measure Unit. Ultraviolet photoelectron spectroscopy (UPS) was performed by an AXIS SUPRA system. Atomic Force Microscopy was carried out using a Cr/Pt coated tip to analyze topography, and surface roughness using the MFP-3D SPM equipment by Asylum Research. External quantum efficiency (EQE) was measured using PTS-1-SR (Sciencetech Inc.). A Thorlabs S401C thermal power sensor was used to calibrate the EQE setup by measuring the incident light power at each wavelength. A correction factor was calculated as the average ratio of calibrated to nominal EQE and applied uniformly to both the nominal EQE spectrum and the corresponding integrated photocurrent.

The operational stability at maximum power point was tested in a glove box filled with nitrogen by using a white LED as a light source because the Xe lamp, which provides a closer spectrum to AM 1.5G, has a short lifetime. The MPP figures were recorded by the Ossila source meter at an open voltage, which gives the maximum power.

Chapter 5.

Conclusions and Outlook

5.1 Conclusions

Perovskite solar cells (PSCs) have achieved remarkable progress in just over a decade, positioning themselves on the verge of commercialization. From a modest 3.8% power conversion efficiency (PCE) in 2009 to an impressive 27% (single junction) in 2025, their rapid advancement has captured significant attention from the research community. Today, the key challenges lie in achieving high efficiencies in large-area devices and ensuring long-term stability—ideally exceeding 25 years—to meet commercial viability.

To propel PSCs toward industrialization, three critical strategies must be prioritized. First, optimizing the perovskite composition to achieve an ideal bandgap, as dictated by the Shockley-Queisser (S-Q) limit, is essential for maximizing PCE. Second, overcoming material stability issues is fundamental to guaranteeing durable performance under real-world conditions. Finally, developing scalable thin-film deposition techniques and enhancing efficiency in ambient environments are crucial steps for industrial-scale production. By addressing these challenges, the gap between laboratory breakthroughs and mass manufacturing can be effectively bridged, accelerating the transition of perovskite solar cells from promising technology to mainstream renewable energy solution.

In this thesis, we first developed lab-scale methods and protocols to fabricate them in ambient air and developed a method name as ‘’Sanity Check’’ to ensure the robustness of device encapsulation. We then moved to upscale the fabrication of PSCs for which we made all-scalable and all in ambient air PSCs. The key findings of this work are summarized as follows:

In Chapter 2, we examined the careful optimization of device fabrication processes and material compositions. While most studies emphasize fabrication protocols conducted in an inert atmosphere, only a limited number provide reproducible methods for preparing PSCs in ambient air. Even fewer report stable maximum power point (MPP) operations under such conditions.

This chapter details step-by-step procedures for fabricating 20%-efficient PSCs in ambient air and encapsulate them to achieve stable MPP operation for over 500 hours. Additionally, we introduce a straightforward encapsulation testing method: our findings indicate that if an encapsulated device can endure 120 °C heat stress for 5 minutes in ambient air, it is likely to maintain long-term stability under MPP conditions.

In the 3rd chapter, we discussed that grain boundaries in PSCs are a key contributor to device degradation. In this chapter, we present a strategy for selectively passivating these grain boundaries using biphenyl-based molecules. Our findings reveal that biphenyl ligands specifically interact with PbI_2-rich interfaces while remaining inert toward the perovskite bulk. This targeted passivation extends the radiative recombination lifetime from 1 μs to 2.7 μs while maintaining efficient charge transport across grain boundaries. Additionally, the hydrophobic benzene rings in biphenyl enhance moisture resistance, improving perovskite stability by a factor of 3 in direct water exposure tests. All devices were fabricated in ambient air, demonstrating high reproducibility with efficiencies ranging from 17% to 21% and an increased open-circuit voltage of 1.11 V. This work establishes a design principle for selective grain boundary passivation and chemical stabilization in hybrid perovskite structures.

In the 4th chapter, we explored that high-performance PSCs require an electron transport layer (ETL) with superior light-trapping properties, minimal defects, and long charge-carrier lifetimes. Among ETL candidates, SnO_x stands out due to its compatibility with efficient PSCs. While various deposition methods exist, chemical bath deposition (CBD) offers a promising balance of high efficiency and scalability. However, the reaction environment in CBD remains poorly controlled, often leading to non-uniform films.

In this study, we introduced $PbCl_2$ as an additive in the conventional CBD process. The choice of $PbCl_2$ is based on its Cl content—compatible with the precursor solution—and the chemical similarity between Pb and Sn. We found that $PbCl_2$ stabilizes the solution's *pH*, ensuring controlled OH^- availability for uniform SnO_x deposition. Without $PbCl_2$, the *pH* shifted from 1.17 to 1.06 after 5 hours, resulting in SnO_x agglomeration. In contrast, with $PbCl_2$, the *pH* remained stable (1.13 to 1.10), yielding a smooth and dense SnO_x film. Using this optimized method, we fabricated fully scalable PSCs in ambient air, achieving a champion efficiency of 24.5%, with FF × V_{OC} reaching 83.4% of the S-Q limit (1.52 eV bandgap). Our devices show >84% retention of initial PCE after 1000+ hours under maximum power point tracking (MPPT). And lastly, a 17.8% PCE in ambient-air-processed perovskite mini-modules (active area: 10.23 cm^2) was also fabricated.

Figure 5-1 represents my progress during the PhD program:

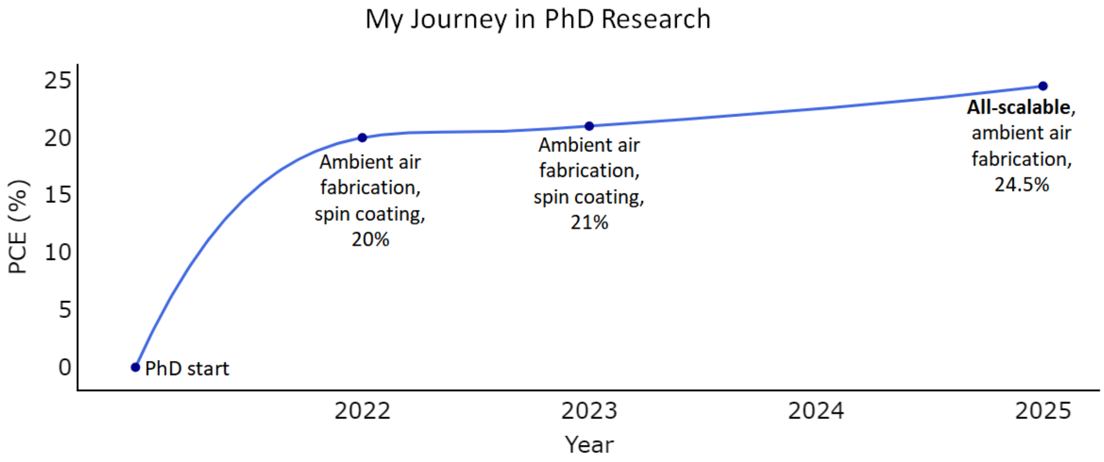

Figure 5-1. A graph depicting the PCE increase over the time and fabrication methods developed during my PhD program.

5.2 Outlook

While significant progress has been made in transitioning from small-area lab-scale devices to scalable modules with competitive efficiency under ambient conditions, their performance still falls short of spin-coated devices fabricated in controlled nitrogen environments. To bridge this gap, future research must systematically address the challenges inherent to ambient processing and blade-coating techniques. Additionally, developing tailored passivation strategies and stabilizing additives for $FAPbI_3$-based perovskites will be critical to enhancing both efficiency and stability in industrially viable production.

The following are some potential directions that aim at achieving higher performance all blade coating perovskite solar cells fabricated in ambient air:

(1) Surface and interface passivation to enhance device performance: Due to the soft lattice nature of perovskite materials, their performance is influenced not only by surface and interface defects but also by external factors such as humidity, temperature, and light exposure. Therefore, surface and interface passivation layers play a crucial role in improving device performance. Common passivation strategies include:

(i) Introducing 2D interface passivation layers on 3D perovskite surfaces reduces non-radiative recombination and enhances charge extraction.[265]

(ii) Molecular passivation with functional groups effectively passivates surface defects by increasing their formation energy while simultaneously neutralizing surface charges and improving carrier extraction through work function modification.[266,267]

(iii) Depositing thin inorganic films (e.g., Al_2O_3, TiO_2) to physically shield the perovskite from moisture and oxygen while minimizing interfacial recombination.[268]

(2) One step fabrication process in large-area blade-coated films: Current multi-layer deposition methods require separate preparation and processing of each functional layer, increasing complexity, cost, and material waste. A streamlined one-step fabrication process could significantly simplify large-scale production by enabling the simultaneous formation of multiple layers—reducing processing steps, minimizing solvent use, and cutting overall manufacturing costs.[269]

Key strategies include, exploring electron and hole selective materials which can be simultaneously dissolved and prepared with perovskite ink and adjusting the concentration, solution viscosity and annealing temperatures to form three layers in a single step.

By merging deposition into a single step, this approach eliminates the need for multiple solutions, reduces solvent consumption, and mitigates interfacial defects—paving the way for more efficient, scalable, and cost-effective perovskite solar cell manufacturing.

(3) Lead (Pb) toxicity in PSCs: It has gained increasing attention for the environmental concerns. As a highly toxic heavy metal, Pb poses serious risks of environmental contamination through potential leaching into soil and water systems. This critical issue has driven substantial research efforts to develop Pb-free perovskite alternatives that maintain the exceptional optoelectronic properties of lead-based perovskites while eliminating toxicity concerns. Among potential substitutes, tin (Sn) has emerged as the most promising candidate due to its similar electronic configuration and comparable physicochemical properties to Pb. However, a fundamental challenge arises from the tendency of Sn^{2+} to oxidize to Sn^{4+} in ambient conditions, leading to the formation of defects that significantly degrade photovoltaic performance.

At the start of my PhD program, I wrote a review paper highlighting this challenge through careful consideration of redox thermodynamics, particularly by Frost-Ebsworth diagrams.[162] These diagrams clearly demonstrate that the +2 oxidation state represents a thermodynamic minimum for both Pb and Sn, indicating its inherent stability (**Figure 5-2 A,B**). This thermodynamic framework explains the observed comproportionation reaction where Sn^{4+} can be reduced back to Sn^{2+} through reaction with metallic Sn, a phenomenon that has been successfully employed to improve device performance by adding Sn powder to precursor solutions. Building on these fundamental insights, future research must focus on developing robust strategies to kinetically stabilize the Sn^{2}+ oxidation state, potentially through chemical additives, lattice engineering, or advanced encapsulation techniques.

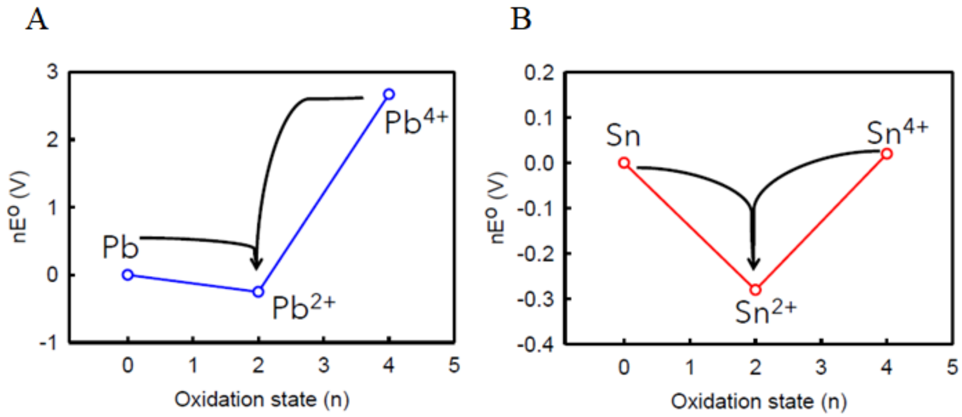

Figure 5-2. Frost diagram for (A) Pb and (B) Sn in standard conditions, where a Frost diagram is used to express the stability of an element at its different oxidation states, relative to its free element. In the Frost diagram, x-axis represent the oxidation state and the y-axis represent relative free energy Reprinted (adapted) with permission from ref.[162] Copyright 2021 American Chemical Society.

By systematically addressing the oxidation stability challenge while leveraging Sn's favorable electronic properties, we can pave the way for high-performance, environmentally sustainable PSCs that maintain the remarkable efficiency of Pb-based systems while eliminating their toxicological concerns. This represents a crucial step forward in the development of commercially viable and environmentally responsible perovskite technologies.

(4) **Scaling up perovskite solar modules (PSMs)** to square-meter (m^2) sizes: It presents significant challenges, particularly in depositing high-quality perovskite photoactive layers over large areas. One of the most pressing issues is the decline in PCE as the module size increases. This efficiency loss stems from multiple interconnected factors, including non-uniform film coverage and thickness variations across the substrate, higher

defect densities in the perovskite layer, and increased series resistance caused by the limited conductivity of large-area transparent conducting electrodes (TCEs).[270,271]

Film inhomogeneity and thickness variations can lead to a wide distribution of PCE values across the module, while elevated defect densities hinder charge carrier extraction and transport. Additionally, the sheet resistance of TCEs rises with area, further reducing the fill factor and overall performance. To address these challenges, researchers are exploring advanced deposition techniques like roll-to-roll (R2R) processing, which can improve film uniformity, and modular designs that connect smaller sub-cells in series to minimize resistive losses.[272]

However, the most critical hurdle remains reducing defect densities in perovskite films on scale. Recent studies suggest that incorporating high-quality passivation molecules—such as Lewis bases, or halogen-rich additives—can effectively suppress defect states by chemically interacting with undercoordinated Pb^{2+} or halide vacancies.[273–275] These passivation strategies not only enhance carrier lifetimes but also improve phase stability, ultimately leading to higher PCEs in large-area PSMs. Moving forward, optimizing these defect mitigation approaches while maintaining compatibility with scalable fabrication methods will be essential for bridging the efficiency gap between lab-scale cells and commercial m^2-sized modules.

References

(1) *Renewable capacity statistics 2025*. https://www.irena.org/Publications/2025/Mar/Renewable-capacity-statistics-2025 (accessed 2025-04-17).

(2) Ritchie, H.; Rosado, P.; Roser, M. Energy Production and Consumption. *Our World Data* **2020**.

(3) Ritchie, H.; Rosado, P. Electricity Mix. *Our World Data* **2020**.

(4) Ritchie, H.; Rosado, P.; Roser, M. CO_2 and Greenhouse Gas Emissions. *Our World Data* **2023**.

(5) Karmaker, A. K.; Rahman, Md. M.; Hossain, Md. A.; Ahmed, Md. R. Exploration and Corrective Measures of Greenhouse Gas Emission from Fossil Fuel Power Stations for Bangladesh. *J. Clean. Prod.* **2020**, *244*, 118645. https://doi.org/10.1016/j.jclepro.2019.118645.

(6) Tubiello, F. N.; Salvatore, M.; Rossi, S.; Ferrara, A.; Fitton, N.; Smith, P. The FAOSTAT Database of Greenhouse Gas Emissions from Agriculture. *Environ. Res. Lett.* **2013**, *8* (1), 015009. https://doi.org/10.1088/1748-9326/8/1/015009.

(7) Staples, M. D.; Malina, R.; Barrett, S. R. H. The Limits of Bioenergy for Mitigating Global Life-Cycle Greenhouse Gas Emissions from Fossil Fuels. *Nat. Energy* **2017**, *2* (2), 1–8. https://doi.org/10.1038/nenergy.2016.202.

(8) Bilgen, S. Structure and Environmental Impact of Global Energy Consumption. *Renew. Sustain. Energy Rev.* **2014**, *38*, 890–902. https://doi.org/10.1016/j.rser.2014.07.004.

(9) Hasanuzzaman, M.; Zubir, U. S.; Ilham, N. I.; Seng Che, H. Global Electricity Demand, Generation, Grid System, and Renewable Energy Polices: A Review. *WIREs Energy Environ.* **2017**, *6* (3), e222. https://doi.org/10.1002/wene.222.

(10) Valentine, S. V. Emerging Symbiosis: Renewable Energy and Energy Security. *Renew. Sustain. Energy Rev.* **2011**, *15* (9), 4572–4578. https://doi.org/10.1016/j.rser.2011.07.095.

(11) Asif, M.; Muneer, T. Energy Supply, Its Demand and Security Issues for Developed and Emerging Economies. *Renew. Sustain. Energy Rev.* **2007**, *11* (7), 1388–1413. https://doi.org/10.1016/j.rser.2005.12.004.

(12) Petter Jelle, B.; Breivik, C.; Drolsum Røkenes, H. Building Integrated Photovoltaic Products: A State-of-the-Art Review and Future Research Opportunities. *Sol. Energy Mater. Sol. Cells* **2012**, *100*, 69–96. https://doi.org/10.1016/j.solmat.2011.12.016.

(13) *Renewables can reduce CO2 emissions by 70% by 2050 - Climate Action*. https://www.climateaction.org/news/renewables_can_reduce_co2_emission_by_70_by_2050 (accessed 2025-04-17).

(14) Hoegh-Guldberg, O.; Jacob, D.; Taylor, M.; Guillén Bolaños, T.; Bindi, M.; Brown, S.; Camilloni, I. A.; Diedhiou, A.; Djalante, R.; Ebi, K.; Engelbrecht, F.; Guiot, J.; Hijioka, Y.; Mehrotra, S.; Hope, C. W.; Payne, A. J.; Pörtner, H.-O.; Seneviratne, S. I.; Thomas, A.; Warren, R.; Zhou, G. The Human Imperative of Stabilizing Global Climate Change at 1.5°C. *Science* **2019**, *365* (6459), eaaw6974. https://doi.org/10.1126/science.aaw6974.

(15) Dhillon, R. S.; von Wuehlisch, G. Mitigation of Global Warming through Renewable Biomass. *Biomass Bioenergy* **2013**, *48*, 75–89. https://doi.org/10.1016/j.biombioe.2012.11.005.

(16) Martínez, J.; Mboup, G.; Sliuzas, R.; Stein, A. Trends in Urban and Slum Indicators across Developing World Cities, 1990–2003. *Habitat Int.* **2008**, *32* (1), 86–108. https://doi.org/10.1016/j.habitatint.2007.08.018.

(17) Perez, M.; Perez, R. Update 2022 – A Fundamental Look at Supply Side Energy Reserves for the Planet. *Sol. Energy Adv.* **2022**, *2*, 100014. https://doi.org/10.1016/j.seja.2022.100014.

(18) Green, M. A. Photovoltaics: Coming of Age. In *IEEE Conference on Photovoltaic Specialists*; 1990; pp 1–8 vol.1. https://doi.org/10.1109/PVSC.1990.111582.

(19) *Best Research-Cell Efficiency Chart | Photovoltaic Research | NREL*. https://www2.nrel.gov/pv/cell-efficiency (accessed 2025-04-17).

(20) Katz, E. A. Perovskite: Name Puzzle and German-Russian Odyssey of Discovery. *Helv. Chim. Acta* **2020**, *103* (6), e2000061. https://doi.org/10.1002/hlca.202000061.

(21) Christy, M.; Choi, S.; Kwon, J.; Jeong, J.; Paik, U.; Song, T. The Perfect Imperfections of Perovskite Oxide Catalysts in the Aspect of Defect Equilibria. *Small Sci.* **2025**, *5* (1), 2400386. https://doi.org/10.1002/smsc.202400386.

(22) Qian, J.; Xu, B.; Tian, W. A Comprehensive Theoretical Study of Halide Perovskites ABX3. *Org. Electron.* **2016**, *37*, 61–73. https://doi.org/10.1016/j.orgel.2016.05.046.

(23) Mitzi, D. B. Introduction: Perovskites. *Chem. Rev.* **2019**, *119* (5), 3033–3035. https://doi.org/10.1021/acs.chemrev.8b00800.

(24) Singh, A.; Mitzi, D. B. Emergence of Melt and Glass States of Halide Perovskite Semiconductors. *Nat. Rev. Mater.* **2025**, *10* (3), 211–227. https://doi.org/10.1038/s41578-024-00759-x.

(25) Saparov, B.; Mitzi, D. B. Organic–Inorganic Perovskites: Structural Versatility for Functional Materials Design. *Chem. Rev.* **2016**, *116* (7), 4558–4596. https://doi.org/10.1021/acs.chemrev.5b00715.

(26) Grätzel, M. The Rise of Highly Efficient and Stable Perovskite Solar Cells. *Acc. Chem. Res.* **2017**, *50* (3), 487–491. https://doi.org/10.1021/acs.accounts.6b00492.

(27) Chen, Q.; De Marco, N.; Yang, Y. (Michael); Song, T.-B.; Chen, C.-C.; Zhao, H.; Hong, Z.; Zhou, H.; Yang, Y. Under the Spotlight: The Organic–Inorganic Hybrid Halide Perovskite for Optoelectronic Applications. *Nano Today* **2015**, *10* (3), 355–396. https://doi.org/10.1016/j.nantod.2015.04.009.

(28) Zhao, Y.; Zhu, K. Organic–Inorganic Hybrid Lead Halide Perovskites for Optoelectronic and Electronic Applications. *Chem. Soc. Rev.* **2016**, *45* (3), 655–689. https://doi.org/10.1039/C4CS00458B.

(29) Fakharuddin, A.; Shabbir, U.; Qiu, W.; Iqbal, T.; Sultan, M.; Heremans, P.; Schmidt-Mende, L. Inorganic and Layered Perovskites for Optoelectronic Devices. *Adv. Mater.* **2019**, *31* (47), 1807095. https://doi.org/10.1002/adma.201807095.

(30) Li, Z.; Klein, T. R.; Kim, D. H.; Yang, M.; Berry, J. J.; van Hest, M. F. A. M.; Zhu, K. Scalable Fabrication of Perovskite Solar Cells. *Nat. Rev. Mater.* **2018**, *3* (4), 1–20. https://doi.org/10.1038/natrevmats.2018.17.

(31) Wang, P.; Wu, Y.; Cai, B.; Ma, Q.; Zheng, X.; Zhang, W.-H. Solution-Processable Perovskite Solar Cells toward Commercialization: Progress and Challenges. *Adv. Funct. Mater.* **2019**, *29* (47), 1807661. https://doi.org/10.1002/adfm.201807661.

(32) Pasquarelli, R. M.; Ginley, D. S.; O'Hayre, R. Solution Processing of Transparent Conductors: From Flask to Film. *Chem. Soc. Rev.* **2011**, *40* (11), 5406–5441. https://doi.org/10.1039/C1CS15065K.

(33) Ranjan, S.; Balaji, S.; Panella, R. A.; Ydstie, B. E. Silicon Solar Cell Production. *Comput. Chem. Eng.* **2011**, *35* (8), 1439–1453. https://doi.org/10.1016/j.compchemeng.2011.04.017.

(34) Pizzini, S. Towards Solar Grade Silicon: Challenges and Benefits for Low Cost Photovoltaics. *Sol. Energy Mater. Sol. Cells* **2010**, *94* (9), 1528–1533. https://doi.org/10.1016/j.solmat.2010.01.016.

(35) Zulehner, W. Czochralski Growth of Silicon. *J. Cryst. Growth* **1983**, *65* (1), 189–213. https://doi.org/10.1016/0022-0248(83)90051-9.

(36) Dornberger, E.; Tomzig, E.; Seidl, A.; Schmitt, S.; Leister, H.-J.; Schmitt, Ch.; Müller, G. Thermal Simulation of the Czochralski Silicon Growth Process by Three Different Models and Comparison with Experimental Results. *J. Cryst. Growth* **1997**, *180* (3), 461–467. https://doi.org/10.1016/S0022-0248(97)00241-8.

(37) Arif, M.; Rahman, M.; San, W. Y. A State-of-the-Art Review of Ductile Cutting of Silicon Wafers for Semiconductor and Microelectronics Industries. *Int. J. Adv. Manuf. Technol.* **2012**, *63* (5), 481–504. https://doi.org/10.1007/s00170-012-3937-2.

(38) Yang, H. L.; Liu, I. T.; Liu, C. E.; Hsu, H. P.; Lan, C. W. Recycling and Reuse of Kerf-Loss Silicon from Diamond Wire Sawing for Photovoltaic Industry. *Waste Manag.* **2019**, *84*, 204–210. https://doi.org/10.1016/j.wasman.2018.11.045.

(39) Liu, X.; R. Coxon, P.; Peters, M.; Hoex, B.; M. Cole, J.; J. Fray, D. Black Silicon: Fabrication Methods, Properties and Solar Energy Applications. *Energy Environ. Sci.* **2014**, *7* (10), 3223–3263. https://doi.org/10.1039/C4EE01152J.

(40) Louwen, A.; van Sark, W.; Schropp, R.; Faaij, A. A Cost Roadmap for Silicon Heterojunction Solar Cells. *Sol. Energy Mater. Sol. Cells* **2016**, *147*, 295–314. https://doi.org/10.1016/j.solmat.2015.12.026.

(41) Lin, S.; Zhang, T.; Yang, H.; Li, Y. Progress and Perspectives of Solar Cells: A Critical Review. *Energy Fuels* **2024**, *38* (2), 761–788. https://doi.org/10.1021/acs.energyfuels.3c02908.

(42) Yang, C.; Hu, W.; Liu, J.; Han, C.; Gao, Q.; Mei, A.; Zhou, Y.; Guo, F.; Han, H. Achievements, Challenges, and Future Prospects for Industrialization of Perovskite Solar Cells. *Light Sci. Appl.* **2024**, *13* (1), 227. https://doi.org/10.1038/s41377-024-01461-x.

(43) Liu, C.; Cheng, Y.-B.; Ge, Z. Understanding of Perovskite Crystal Growth and Film Formation in Scalable Deposition Processes. *Chem. Soc. Rev.* **2020**, *49* (6), 1653–1687. https://doi.org/10.1039/C9CS00711C.

(44) Huang, F.; Li, M.; Siffalovic, P.; Cao, G.; Tian, J. From Scalable Solution Fabrication of Perovskite Films towards Commercialization of Solar Cells. *Energy Environ. Sci.* **2019**, *12* (2), 518–549. https://doi.org/10.1039/C8EE03025A.

(45) Howard, I. A.; Abzieher, T.; Hossain, I. M.; Eggers, H.; Schackmar, F.; Ternes, S.; Richards, B. S.; Lemmer, U.; Paetzold, U. W. Coated and Printed Perovskites for Photovoltaic Applications. *Adv. Mater.* **2019**, *31* (26), 1806702. https://doi.org/10.1002/adma.201806702.

(46) Liu, J.; Ye, T.; Yu, D.; Liu, S. (Frank); Yang, D. Recoverable Flexible Perovskite Solar Cells for Next-Generation Portable Power Sources. *Angew. Chem. Int. Ed.* **2023**, *62* (40), e202307225. https://doi.org/10.1002/anie.202307225.

(47) Rong, Y.; Hu, Y.; Mei, A.; Tan, H.; Saidaminov, M. I.; Seok, S. I.; McGehee, M. D.; Sargent, E. H.; Han, H. Challenges for Commercializing Perovskite Solar Cells. *Science* **2018**, *361* (6408), eaat8235. https://doi.org/10.1126/science.aat8235.

(48) Park, N.-G. Research Direction toward Scalable, Stable, and High Efficiency Perovskite Solar Cells. *Adv. Energy Mater.* **2020**, *10* (13), 1903106. https://doi.org/10.1002/aenm.201903106.

(49) Li, N.; Niu, X.; Chen, Q.; Zhou, H. Towards Commercialization: The Operational Stability of Perovskite Solar Cells. *Chem. Soc. Rev.* **2020**, *49* (22), 8235–8286. https://doi.org/10.1039/D0CS00573H.

(50) Park, N.-G.; Zhu, K. Scalable Fabrication and Coating Methods for Perovskite Solar Cells and Solar Modules. *Nat. Rev. Mater.* **2020**, *5* (5), 333–350. https://doi.org/10.1038/s41578-019-0176-2.

(51) Saliba, M.; Correa-Baena, J.-P.; Grätzel, M.; Hagfeldt, A.; Abate, A. Perovskite Solar Cells: From the Atomic Level to Film Quality and Device Performance. *Angew. Chem. Int. Ed.* **2018**, *57* (10), 2554–2569. https://doi.org/10.1002/anie.201703226.

(52) Lin, R.; Xu, J.; Wei, M.; Wang, Y.; Qin, Z.; Liu, Z.; Wu, J.; Xiao, K.; Chen, B.; Park, S. M.; Chen, G.; Atapattu, H. R.; Graham, K. R.; Xu, J.; Zhu, J.; Li, L.; Zhang, C.; Sargent, E. H.; Tan, H. All-Perovskite Tandem Solar Cells with Improved Grain Surface Passivation. *Nature* **2022**, *603* (7899), 73–78. https://doi.org/10.1038/s41586-021-04372-8.

(53) Lin, R.; Wang, Y.; Lu, Q.; Tang, B.; Li, J.; Gao, H.; Gao, Y.; Li, H.; Ding, C.; Wen, J.; Wu, P.; Liu, C.; Zhao, S.; Xiao, K.; Liu, Z.; Ma, C.; Deng, Y.; Li, L.; Fan, F.; Tan, H. All-Perovskite Tandem Solar Cells with 3D/3D Bilayer Perovskite Heterojunction. *Nature* **2023**, *620* (7976), 994–1000. https://doi.org/10.1038/s41586-023-06278-z.

(54) Eperon, G. E.; Leijtens, T.; Bush, K. A.; Prasanna, R.; Green, T.; Wang, J. T.-W.; McMeekin, D. P.; Volonakis, G.; Milot, R. L.; May, R.; Palmstrom, A.; Slotcavage, D. J.; Belisle, R. A.; Patel, J. B.; Parrott, E. S.; Sutton, R. J.; Ma, W.; Moghadam, F.; Conings, B.; Babayigit, A.; Boyen, H.-G.; Bent, S.; Giustino, F.; Herz, L. M.; Johnston, M. B.; McGehee, M. D.; Snaith, H. J. Perovskite-Perovskite Tandem Photovoltaics with Optimized Band Gaps. *Science* **2016**, *354* (6314), 861–865. https://doi.org/10.1126/science.aaf9717.

(55) Li, H.; Zhang, W. Perovskite Tandem Solar Cells: From Fundamentals to Commercial Deployment. *Chem. Rev.* **2020**, *120* (18), 9835–9950. https://doi.org/10.1021/acs.chemrev.9b00780.

(56) Lal, N. N.; Dkhissi, Y.; Li, W.; Hou, Q.; Cheng, Y.-B.; Bach, U. Perovskite Tandem Solar Cells. *Adv. Energy Mater.* **2017**, *7* (18), 1602761. https://doi.org/10.1002/aenm.201602761.

(57) Mohamad Noh, M. F.; Arzaee, N. A.; Fat, C. C.; Sieh Kiong, T.; Mat Teridi, M. A.; Mahmood Zuhdi, A. W. Perovskite/CIGS Tandem Solar Cells: Progressive Advances from Technical Perspectives. *Mater. Today Energy* **2024**, *39*, 101473. https://doi.org/10.1016/j.mtener.2023.101473.

(58) Xiao, K.; Lin, Y.-H.; Zhang, M.; Oliver, R. D. J.; Wang, X.; Liu, Z.; Luo, X.; Li, J.; Lai, D.; Luo, H.; Lin, R.; Xu, J.; Hou, Y.; Snaith, H. J.; Tan, H. Scalable Processing for Realizing 21.7%-Efficient All-Perovskite Tandem Solar Modules. *Science* **2022**, *376* (6594), 762–767. https://doi.org/10.1126/science.abn7696.

(59) Jošt, M.; Köhnen, E.; Al-Ashouri, A.; Bertram, T.; Tomšič, Š.; Magomedov, A.; Kasparavicius, E.; Kodalle, T.; Lipovšek, B.; Getautis, V.; Schlatmann, R.; Kaufmann, C. A.; Albrecht, S.; Topič, M. Perovskite/CIGS Tandem Solar Cells: From Certified 24.2% toward 30% and Beyond. *ACS Energy Lett.* **2022**, *7* (4), 1298–1307. https://doi.org/10.1021/acsenergylett.2c00274.

(60) Rajagopal, A.; Yang, Z.; Jo, S. B.; Braly, I. L.; Liang, P.-W.; Hillhouse, H. W.; Jen, A. K.-Y. Highly Efficient Perovskite–Perovskite Tandem Solar Cells Reaching 80% of the Theoretical Limit in Photovoltage. *Adv. Mater.* **2017**, *29* (34), 1702140. https://doi.org/10.1002/adma.201702140.

(61) Ugur, E.; Said, A. A.; Dally, P.; Zhang, S.; Petoukhoff, C. E.; Rosas-Villalva, D.; Zhumagali, S.; Yildirim, B. K.; Razzaq, A.; Sarwade, S.; Yazmaciyan, A.; Baran, D.; Laquai, F.; Deger, C.; Yavuz, I.; Allen, T. G.; Aydin, E.; De Wolf, S. Enhanced Cation Interaction in Perovskites for Efficient Tandem Solar Cells with Silicon. *Science* **2024**, *385* (6708), 533–538. https://doi.org/10.1126/science.adp1621.

(62) De Roo, J.; Ibáñez, M.; Geiregat, P.; Nedelcu, G.; Walravens, W.; Maes, J.; Martins, J. C.; Van Driessche, I.; Kovalenko, M. V.; Hens, Z. Highly Dynamic Ligand Binding and Light Absorption Coefficient of Cesium Lead Bromide Perovskite Nanocrystals. *ACS Nano* **2016**, *10* (2), 2071–2081. https://doi.org/10.1021/acsnano.5b06295.

(63) M. Ball, J.; D. Stranks, S.; T. Hörantner, M.; Hüttner, S.; Zhang, W.; W. Crossland, E. J.; Ramirez, I.; Riede, M.; B. Johnston, M.; H. Friend, R.; J. Snaith, H. Optical Properties and Limiting Photocurrent of Thin-Film Perovskite Solar Cells. *Energy Environ. Sci.* **2015**, *8* (2), 602–609. https://doi.org/10.1039/C4EE03224A.

(64) Richter, A.; Benick, J.; Feldmann, F.; Fell, A.; Hermle, M.; Glunz, S. W. N-Type Si Solar Cells with Passivating Electron Contact: Identifying Sources for Efficiency Limitations by Wafer Thickness and Resistivity Variation. *Sol. Energy Mater. Sol. Cells* **2017**, *173*, 96–105. https://doi.org/10.1016/j.solmat.2017.05.042.

(65) Davies, C. L.; Filip, M. R.; Patel, J. B.; Crothers, T. W.; Verdi, C.; Wright, A. D.; Milot, R. L.; Giustino, F.; Johnston, M. B.; Herz, L. M. Bimolecular Recombination in Methylammonium Lead Triiodide Perovskite Is an Inverse Absorption Process. *Nat. Commun.* **2018**, *9* (1), 293. https://doi.org/10.1038/s41467-017-02670-2.

(66) Yeddu, V.; Seo, G.; Bamidele, M.; Jung, H.; Yu, H.; Lee, J. W.; Lee, J.; Kim, D. Y. High-Detectivity UV–Vis–NIR Broadband Perovskite Photodetector Using a Mixed Pb–Sn Narrow-Band-Gap Absorber and a NiOx Electron Blocker. *ACS Appl. Electron. Mater.* **2022**, *4* (3), 1206–1213. https://doi.org/10.1021/acsaelm.1c01264.

(67) Sum, T. C.; Chen, S.; Xing, G.; Liu, X.; Wu, B. Energetics and Dynamics in Organic–Inorganic Halide Perovskite Photovoltaics and Light Emitters. *Nanotechnology* **2015**, *26* (34), 342001. https://doi.org/10.1088/0957-4484/26/34/342001.

(68) Jin, H.; Debroye, E.; Keshavarz, M.; Scheblykin, I. G.; Roeffaers, M. B. J.; Hofkens, J.; Steele, J. A. It's a Trap! On the Nature of Localised States and Charge Trapping in Lead Halide Perovskites. *Mater. Horiz.* **2020**, *7* (2), 397–410. https://doi.org/10.1039/C9MH00500E.

(69) Kim, Y. Y.; Yang, T.-Y.; Suhonen, R.; Kemppainen, A.; Hwang, K.; Jeon, N. J.; Seo, J. Roll-to-Roll Gravure-Printed Flexible Perovskite Solar Cells Using Eco-Friendly Antisolvent Bathing with Wide Processing Window. *Nat. Commun.* **2020**, *11* (1), 5146. https://doi.org/10.1038/s41467-020-18940-5.

(70) Motta, C.; El-Mellouhi, F.; Sanvito, S. Charge Carrier Mobility in Hybrid Halide Perovskites. *Sci. Rep.* **2015**, *5* (1), 12746. https://doi.org/10.1038/srep12746.

(71) Shi, D.; Adinolfi, V.; Comin, R.; Yuan, M.; Alarousu, E.; Buin, A.; Chen, Y.; Hoogland, S.; Rothenberger, A.; Katsiev, K.; Losovyj, Y.; Zhang, X.; Dowben, P. A.; Mohammed, O. F.; Sargent, E. H.; Bakr, O. M. Low Trap-State Density and Long Carrier Diffusion in Organolead Trihalide Perovskite Single Crystals. *Science* **2015**, *347* (6221), 519–522. https://doi.org/10.1126/science.aaa2725.

(72) Castillo-Seoane, J.; Contreras-Bernal, L.; Rojas, T. C.; Espinós, J. P.; Castro-Méndez, A.-F.; Correa-Baena, J.-P.; Barranco, A.; Sanchez-Valencia, J. R.; Borras, A. Highly Stable Photoluminescence in Vacuum-Processed Halide Perovskite Core–Shell 1D Nanostructures. *Adv. Funct. Mater.* **2024**, *34* (40), 2403763. https://doi.org/10.1002/adfm.202403763.

(73) Shockley, W.; Queisser, H. J. Detailed Balance Limit of Efficiency of P-n Junction Solar Cells. *J. Appl. Phys.* **1961**, *32* (3), 510–519. https://doi.org/10.1063/1.1736034.

(74) Tiedje, T.; Yablonovitch, E.; Cody, G. D.; Brooks, B. G. Limiting Efficiency of Silicon Solar Cells. *IEEE Trans. Electron Devices* **1984**, *31* (5), 711–716. https://doi.org/10.1109/T-ED.1984.21594.

(75) Suragtkhuu, S.; Sunderiya, S.; Myagmarsereejid, P.; Purevdorj, S.; Bati, A. S. R.; Bold, B.; Zhong, Y. L.; Davaasambuu, S.; Batmunkh, M. Graphene-Like Monoelemental 2D Materials for Perovskite Solar Cells. *Adv. Energy Mater.* **2023**, *13* (12), 2204074. https://doi.org/10.1002/aenm.202204074.

(76) Kojima, A.; Teshima, K.; Shirai, Y.; Miyasaka, T. Organometal Halide Perovskites as Visible-Light Sensitizers for Photovoltaic Cells. *J. Am. Chem. Soc.* **2009**, *131* (17), 6050–6051. https://doi.org/10.1021/JA809598R/SUPPL_FILE/JA809598R_SI_001.PDF.

(77) Smecca, E.; Numata, Y.; Deretzis, I.; Pellegrino, G.; Boninelli, S.; Miyasaka, T.; Magna, A. L.; Alberti, A. Stability of Solution-Processed MAPbI 3 and FAPbI 3 Layers. *Phys. Chem. Chem. Phys.* **2016**, *18* (19), 13413–13422. https://doi.org/10.1039/C6CP00721J.

(78) Pellet, N.; Gao, P.; Gregori, G.; Yang, T.-Y.; Nazeeruddin, M. K.; Maier, J.; Grätzel, M. Mixed-Organic-Cation Perovskite Photovoltaics for Enhanced Solar-Light Harvesting. *Angew. Chem. Int. Ed.* **2014**, *53* (12), 3151–3157. https://doi.org/10.1002/anie.201309361.

(79) Miller, O. D.; Yablonovitch, E.; Kurtz, S. R. Strong Internal and External Luminescence as Solar Cells Approach the Shockley–Queisser Limit. *IEEE J. Photovolt.* **2012**, *2* (3), 303–311. https://doi.org/10.1109/JPHOTOV.2012.2198434.

(80) Lu, H.; Liu, Y.; Ahlawat, P.; Mishra, A.; Tress, W. R.; Eickemeyer, F. T.; Yang, Y.; Fu, F.; Wang, Z.; Avalos, C. E.; Carlsen, B. I.; Agarwalla, A.; Zhang, X.; Li, X.; Zhan, Y.; Zakeeruddin, S. M.; Emsley, L.; Rothlisberger, U.; Zheng, L.; Hagfeldt, A.; Grätzel, M. Vapor-Assisted Deposition of Highly Efficient, Stable Black-Phase FAPbI3 Perovskite Solar Cells. *Science* **2020**, *370* (6512), eabb8985. https://doi.org/10.1126/science.abb8985.

(81) Cui, X.; Jin, J.; Tai, Q.; Yan, F. Recent Progress on the Phase Stabilization of FAPbI3 for High-Performance Perovskite Solar Cells. *Sol. RRL* **2022**, *6* (10), 2200497. https://doi.org/10.1002/solr.202200497.

(82) Zhang, D.; Khasnabis, S.; Wang, W.; Yeddu, V.; Moradi, S.; Awais, M.; Nguyen, H.-D.; Reinecke, S. B.; Haruta, Y.; Godin, R.; Tan, F.; Saidaminov, M. I. Cadmium-Doping Slows Trap Emptying in Ambient-Air Blade-Coated Formamidinium Lead Iodide Perovskite Solar Cells. *Adv. Energy Mater.* **2024**, *14* (17), 2303858. https://doi.org/10.1002/aenm.202303858.

(83) Fan, Y.; Meng, H.; Wang, L.; Pang, S. Review of Stability Enhancement for Formamidinium-Based Perovskites. *Sol. RRL* **2019**, *3* (9), 1900215. https://doi.org/10.1002/solr.201900215.

(84) Yong-Liang C.; Ya-Wen T.; Pei-Run C.; Li Z.; Qi L.; Ying Z.; Qian H.; Xiao-Dan Z. Progress in perovskite solar cells based on different buffer layer materials. 物理学报 **2020**, *69* (13), 138401–138412. https://doi.org/10.7498/aps.69.20200543.

(85) M. Rombach, F.; A. Haque, S.; J. Macdonald, T. Lessons Learned from Spiro-OMeTAD and PTAA in Perovskite Solar Cells. *Energy Environ. Sci.* **2021**, *14* (10), 5161–5190. https://doi.org/10.1039/D1EE02095A.

(86) Wang, Y.; Duan, L.; Zhang, M.; Hameiri, Z.; Liu, X.; Bai, Y.; Hao, X. PTAA as Efficient Hole Transport Materials in Perovskite Solar Cells: A Review. *Sol. RRL* **2022**, *6* (8), 2200234. https://doi.org/10.1002/solr.202200234.

(87) Kim, S. Y.; Cho, S. J.; Byeon, S. E.; He, X.; Yoon, H. J. Self-Assembled Monolayers as Interface Engineering Nanomaterials in Perovskite Solar Cells. *Adv. Energy Mater.* **2020**, *10* (44), 2002606. https://doi.org/10.1002/aenm.202002606.

(88) Ali, F.; Roldán-Carmona, C.; Sohail, M.; Nazeeruddin, M. K. Applications of Self-Assembled Monolayers for Perovskite Solar Cells Interface Engineering to Address Efficiency and Stability. *Adv. Energy Mater.* **2020**, *10* (48), 2002989. https://doi.org/10.1002/aenm.202002989.

(89) Lv, Y.; Cai, B.; Yuan, R.; Wu, Y.; Qiao, Q.; Zhang, W.-H. Toward High-Efficiency Perovskite Solar Cells with One-Dimensional Oriented Nanostructured Electron Transport Materials. *J. Energy Chem.* **2023**, *82*, 66–87. https://doi.org/10.1016/j.jechem.2023.01.066.

(90) Muthukrishnan, A. P.; Lee, J.; Kim, J.; Kim, C. S.; Jo, S. Low-Temperature Solution-Processed SnO2 Electron Transport Layer Modified by Oxygen Plasma for Planar Perovskite Solar Cells. *RSC Adv.* **2022**, *12* (8), 4883–4890. https://doi.org/10.1039/D1RA08946C.

(91) Jiang, Q.; Zhang, X.; You, J. SnO2: A Wonderful Electron Transport Layer for Perovskite Solar Cells. *Small* **2018**, *14* (31), 1801154. https://doi.org/10.1002/smll.201801154.

(92) Príncipe, J.; Duarte, V. C. M.; Mendes, A.; Andrade, L. Influence of the Transparent Conductive Oxide Type on the Performance of Inverted Perovskite Solar Cells. *ACS Appl. Energy Mater.* **2023**, *6* (24), 12442–12451. https://doi.org/10.1021/acsaem.3c02292.

(93) Li, Y.; Xie, H.; Lim, E. L.; Hagfeldt, A.; Bi, D. Recent Progress of Critical Interface Engineering for Highly Efficient and Stable Perovskite Solar Cells. *Adv. Energy Mater.* **2022**, *12* (5), 2102730. https://doi.org/10.1002/aenm.202102730.

(94) Saliba, M.; Matsui, T.; Seo, J. Y.; Domanski, K.; Correa-Baena, J. P.; Nazeeruddin, M. K.; Zakeeruddin, S. M.; Tress, W.; Abate, A.; Hagfeldt, A.; Grätzel, M. Cesium-Containing Triple Cation Perovskite Solar Cells: Improved Stability, Reproducibility and High Efficiency. *Energy Environ. Sci.* **2016**, *9* (6), 1989–1997. https://doi.org/10.1039/C5EE03874J.

(95) Guo, Z.; Wan, Y.; Yang, M.; Snaider, J.; Zhu, K.; Huang, L. Long-Range Hot-Carrier Transport in Hybrid Perovskites Visualized by Ultrafast Microscopy. *Science* **2017**, *356* (6333), 59–62. https://doi.org/10.1126/SCIENCE.AAM7744/SUPPL_FILE/GUO-SM.PDF.

(96) DeQuilettes, D. W.; Vorpahl, S. M.; Stranks, S. D.; Nagaoka, H.; Eperon, G. E.; Ziffer, M. E.; Snaith, H. J.; Ginger, D. S. Impact of Microstructure on Local Carrier Lifetime in Perovskite Solar Cells. *Science* **2015**, *348* (6235), 683–686. https://doi.org/10.1126/SCIENCE.AAA5333/SUPPL_FILE/AAA5333-DEQUILETTES-SM.PDF.

(97) Saidaminov, M. I.; Spanopoulos, I.; Abed, J.; Ke, W.; Wicks, J.; Kanatzidis, M. G.; Sargent, E. H. Conventional Solvent Oxidizes Sn(II) in Perovskite Inks. *ACS Energy Lett.* **2020**, *5* (4), 1153–1155. https://doi.org/10.1021/ACSENERGYLETT.0C00402/SUPPL_FILE/NZ0C00402_SI_001.PDF.

(98) Lee, M. M.; Teuscher, J.; Miyasaka, T.; Murakami, T. N.; Snaith, H. J. Efficient Hybrid Solar Cells Based on Meso-Superstructured Organometal Halide Perovskites. *Science* **2012**, *338* (6107), 643–647. https://doi.org/10.1126/SCIENCE.1228604/SUPPL_FILE/LEE.SM.PDF.

(99) Burschka, J.; Pellet, N.; Moon, S.-J.; Humphry-Baker, R.; Gao, P.; Nazeeruddin, M. K.; Grätzel, M. Sequential Deposition as a Route to High-Performance Perovskite-Sensitized Solar Cells. *Nature* **2013**, *499* (7458), 316–319. https://doi.org/10.1038/nature12340.

(100) Im, J. H.; Lee, C. R.; Lee, J. W.; Park, S. W.; Park, N. G. 6.5% Efficient Perovskite Quantum-Dot-Sensitized Solar Cell. *Nanoscale* **2011**, *3* (10), 4088–4093. https://doi.org/10.1039/C1NR10867K.

(101) Kim, H. S.; Lee, C. R.; Im, J. H.; Lee, K. B.; Moehl, T.; Marchioro, A.; Moon, S. J.; Humphry-Baker, R.; Yum, J. H.; Moser, J. E.; Grätzel, M.; Park, N. G. Lead Iodide Perovskite Sensitized All-Solid-State Submicron Thin Film Mesoscopic Solar Cell with

Efficiency Exceeding 9%. *Sci. Rep. 2012 21* **2012**, *2* (1), 1–7. https://doi.org/10.1038/srep00591.

(102) Awais, M.; Kirsch, R. L.; Yeddu, V.; Saidaminov, M. I. Tin Halide Perovskites Going Forward: Frost Diagrams Offer Hints. *ACS Mater. Lett.* **2021**, *3* (3), 299–307. https://doi.org/10.1021/ACSMATERIALSLETT.0C00571.

(103) Younis, A.; Lin, C.-H.; Guan, X.; Shahrokhi, S.; Huang, C.-Y.; Wang, Y.; He, T.; Singh, S.; Hu, L.; Ramon Duran Retamal, J.; He, J.-H.; Wu, T.; Younis, A.; Lin, C.; Guan, X.; Shahrokhi, S.; Huang, C.; Wang, Y.; He, T.; Singh, S.; Hu, L.; Wu, T.; D Retamal, J. R.; He, J. Halide Perovskites: A New Era of Solution-Processed Electronics. *Adv. Mater.* **2021**, *33* (23), 2005000. https://doi.org/10.1002/ADMA.202005000.

(104) Jacobsson, T. J.; Hultqvist, A.; García-Fernández, A.; Anand, A.; Al-Ashouri, A.; Hagfeldt, A.; Crovetto, A.; Abate, A.; Ricciardulli, A. G.; Vijayan, A.; Kulkarni, A.; Anderson, A. Y.; Darwich, B. P.; Yang, B.; Coles, B. L.; Perini, C. A. R.; Rehermann, C.; Ramirez, D.; Fairen-Jimenez, D.; Di Girolamo, D.; Jia, D.; Avila, E.; Juarez-Perez, E. J.; Baumann, F.; Mathies, F.; González, G. S. A.; Boschloo, G.; Nasti, G.; Paramasivam, G.; Martínez-Denegri, G.; Näsström, H.; Michaels, H.; Köbler, H.; Wu, H.; Benesperi, I.; Dar, M. I.; Bayrak Pehlivan, I.; Gould, I. E.; Vagott, J. N.; Dagar, J.; Kettle, J.; Yang, J.; Li, J.; Smith, J. A.; Pascual, J.; Jerónimo-Rendón, J. J.; Montoya, J. F.; Correa-Baena, J. P.; Qiu, J.; Wang, J.; Sveinbjörnsson, K.; Hirselandt, K.; Dey, K.; Frohna, K.; Mathies, L.; Castriotta, L. A.; Aldamasy, M. H.; Vasquez-Montoya, M.; Ruiz-Preciado, M. A.; Flatken, M. A.; Khenkin, M. V.; Grischek, M.; Kedia, M.; Saliba, M.; Anaya, M.; Veldhoen, M.; Arora, N.; Shargaieva, O.; Maus, O.; Game, O. S.; Yudilevich, O.; Fassl, P.; Zhou, Q.; Betancur, R.; Munir, R.; Patidar, R.; Stranks, S. D.; Alam, S.; Kar, S.; Unold, T.; Abzieher, T.; Edvinsson, T.; David, T. W.; Paetzold, U. W.; Zia, W.; Fu, W.; Zuo, W.; Schröder, V. R. F.; Tress, W.; Zhang, X.; Chiang, Y. H.; Iqbal, Z.; Xie, Z.; Unger, E. An Open-Access Database and Analysis Tool for Perovskite Solar Cells Based on the FAIR Data Principles. *Nat. Energy 2021 71* **2021**, *7* (1), 107–115. https://doi.org/10.1038/s41560-021-00941-3.

(105) Liang, H.; Yuan, F.; Johnston, A.; Gao, C.; Choubisa, H.; Gao, Y.; Wang, Y. K.; Sagar, L. K.; Sun, B.; Li, P.; Bappi, G.; Chen, B.; Li, J.; Wang, Y.; Dong, Y.; Ma, D.; Gao, Y.; Liu, Y.; Yuan, M.; Saidaminov, M. I.; Hoogland, S.; Lu, Z. H.; Sargent, E. H. High Color Purity Lead-Free Perovskite Light-Emitting Diodes via Sn Stabilization. *Adv. Sci.* **2020**, *7* (8), 1903213. https://doi.org/10.1002/ADVS.201903213.

(106) Moloney, E. G.; Yeddu, V.; Saidaminov, M. I. Strain Engineering in Halide Perovskites. *ACS Mater. Lett.* **2020**, *2* (11), 1495–1508. https://doi.org/10.1021/ACSMATERIALSLETT.0C00308/ASSET/IMAGES/ACSMATERIALSLETT.0C00308.SOCIAL.JPEG_V03.

(107) Tailor, N. K.; Kar, S.; Mishra, P.; These, A.; Kupfer, C.; Hu, H.; Awais, M.; Saidaminov, M.; Dar, M. I.; Brabec, C.; Satapathi, S. Advances in Lead-Free Perovskite Single Crystals: Fundamentals and Applications. *ACS Mater. Lett.* **2021**, *3*, 1025–1080. https://doi.org/10.1021/ACSMATERIALSLETT.1C00242/ASSET/IMAGES/MEDIUM/TZ1C00242_0041.GIF.

(108) Yang, M.; Li, Z.; Reese, M. O.; Reid, O. G.; Kim, D. H.; Siol, S.; Klein, T. R.; Yan, Y.; Berry, J. J.; Van Hest, M. F. A. M.; Zhu, K. Perovskite Ink with Wide Processing Window for

Scalable High-Efficiency Solar Cells. *Nat. Energy 2017 25* **2017**, *2* (5), 1–9. https://doi.org/10.1038/nenergy.2017.38.

(109) Deng, Y.; Zheng, X.; Bai, Y.; Wang, Q.; Zhao, J.; Huang, J. Surfactant-Controlled Ink Drying Enables High-Speed Deposition of Perovskite Films for Efficient Photovoltaic Modules. *Nat. Energy 2018 37* **2018**, *3* (7), 560–566. https://doi.org/10.1038/s41560-018-0153-9.

(110) Kim, Y. Y.; Yang, T. Y.; Suhonen, R.; Kemppainen, A.; Hwang, K.; Jeon, N. J.; Seo, J. Roll-to-Roll Gravure-Printed Flexible Perovskite Solar Cells Using Eco-Friendly Antisolvent Bathing with Wide Processing Window. *Nat. Commun. 2020 111* **2020**, *11* (1), 1–11. https://doi.org/10.1038/s41467-020-18940-5.

(111) Stoumpos, C. C.; Kanatzidis, M. G.; Stoumpos, C. C.; Kanatzidis, M. G. Halide Perovskites: Poor Man's High-Performance Semiconductors. *Adv. Mater.* **2016**, *28* (28), 5778–5793. https://doi.org/10.1002/ADMA.201600265.

(112) Dou, B.; Whitaker, J. B.; Bruening, K.; Moore, D. T.; Wheeler, L. M.; Ryter, J.; Breslin, N. J.; Berry, J. J.; Garner, S. M.; Barnes, F. S.; Shaheen, S. E.; Tassone, C. J.; Zhu, K.; Van Hest, M. F. A. M. Roll-to-Roll Printing of Perovskite Solar Cells. *ACS Energy Lett.* **2018**, *3* (10), 2558–2565. https://doi.org/10.1021/ACSENERGYLETT.8B01556/SUPPL_FILE/NZ8B01556_SI_002.AVI.

(113) Hou, Y.; Du, X.; Scheiner, S.; McMeekin, D. P.; Wang, Z.; Li, N.; Killian, M. S.; Chen, H.; Richter, M.; Levchuk, I.; Schrenker, N.; Spiecker, E.; Stubhan, T.; Luechinger, N. A.; Hirsch, A.; Schmuki, P.; Steinrück, H. P.; Fink, R. H.; Halik, M.; Snaith, H. J.; Brabec, C. J. A Generic Interface to Reduce the Efficiency-Stability-Cost Gap of Perovskite Solar Cells. *Science* **2017**, *358* (6367), 1192–1197. https://doi.org/10.1126/SCIENCE.AAO5561/SUPPL_FILE/AAO5561_HOU_SM.PDF.

(114) Richmond, D.; McCormick, M.; Ekanayaka, T. K.; Teeter, J. D.; Swanson, B. L.; Benker, N.; Hao, G.; Sikich, S.; Enders, A.; Sinitskii, A.; Ilie, C. C.; Dowben, P. A.; Yost, A. J. Inkjet Printing All Inorganic Halide Perovskite Inks for Photovoltaic Applications. *JoVE J. Vis. Exp.* **2019**, *2019* (143), e58760. https://doi.org/10.3791/58760.

(115) Wu, T.; Qin, Z.; Wang, Y.; Wu, Y.; Chen, W.; Zhang, S.; Cai, M.; Dai, S.; Zhang, J.; Liu, J.; Zhou, Z.; Liu, X.; Segawa, H.; Tan, H.; Tang, Q.; Fang, J.; Li, Y.; Ding, L.; Ning, Z.; Qi, Y.; Zhang, Y.; Han, L. The Main Progress of Perovskite Solar Cells in 2020–2021. *Nano-Micro Lett.* **2021**, *13* (1), 1–18. https://doi.org/10.1007/S40820-021-00672-W/TABLES/1.

(116) Goetz, K. P.; Taylor, A. D.; Hofstetter, Y. J.; Vaynzof, Y. Sustainability in Perovskite Solar Cells. *ACS Appl. Mater. Interfaces* **2021**, *13* (1), 1–17. https://doi.org/10.1021/ACSAMI.0C17269/ASSET/IMAGES/ACSAMI.0C17269.SOCIAL.JPEG_V03.

(117) Correa-Baena, J. P.; Abate, A.; Saliba, M.; Tress, W.; Jesper Jacobsson, T.; Grätzel, M.; Hagfeldt, A. The Rapid Evolution of Highly Efficient Perovskite Solar Cells. *Energy Environ. Sci.* **2017**, *10* (3), 710–727. https://doi.org/10.1039/C6EE03397K.

(118) *Best Research-Cell Efficiency Chart | Photovoltaic Research | NREL.* https://www.nrel.gov/pv/cell-efficiency.html (accessed 2022-01-14).

(119) Saliba, M.; Correa-Baena, J. P.; Wolff, C. M.; Stolterfoht, M.; Phung, N.; Albrecht, S.; Neher, D.; Abate, A. How to Make over 20% Efficient Perovskite Solar Cells in Regular (n-i-p) and Inverted (p-i-n) Architectures. *Chem. Mater.* **2018**, *30* (13), 4193–4201. https://doi.org/10.1021/ACS.CHEMMATER.8B00136/SUPPL_FILE/CM8B00136_SI_003.MPG.

(120) Goetz, K. P.; Vaynzof, Y. The Challenge of Making the Same Device Twice in Perovskite Photovoltaics. *ACS Energy Lett.* **2022**, 1750–1757. https://doi.org/10.1021/ACSENERGYLETT.2C00463.

(121) Grancini, G.; Roldán-Carmona, C.; Zimmermann, I.; Mosconi, E.; Lee, X.; Martineau, D.; Narbey, S.; Oswald, F.; De Angelis, F.; Graetzel, M.; Nazeeruddin, M. K. One-Year Stable Perovskite Solar Cells by 2D/3D Interface Engineering. *Nat. Commun. 2017 81* **2017**, *8* (1), 1–8. https://doi.org/10.1038/ncomms15684.

(122) Leijtens, T.; Eperon, G. E.; Noel, N. K.; Habisreutinger, S. N.; Petrozza, A.; Snaith, H. J. Stability of Metal Halide Perovskite Solar Cells. *Adv. Energy Mater.* **2015**, *5* (20), 1500963. https://doi.org/10.1002/AENM.201500963.

(123) Wang, D.; Wright, M.; Elumalai, N. K.; Uddin, A. Stability of Perovskite Solar Cells. *Sol. Energy Mater. Sol. Cells* **2016**, *147*, 255–275. https://doi.org/10.1016/j.solmat.2015.12.025.

(124) Niu, G.; Guo, X.; Wang, L. Review of Recent Progress in Chemical Stability of Perovskite Solar Cells. *J. Mater. Chem. A* **2015**, *3* (17), 8970–8980. https://doi.org/10.1039/C4TA04994B.

(125) Spanopoulos, I.; Ke, W.; Kanatzidis, M. G. In Quest of Environmentally Stable Perovskite Solar Cells: A Perspective. *Helv. Chim. Acta* **2021**, *104* (1), e2000173. https://doi.org/10.1002/HLCA.202000173.

(126) Kirmani, A. R.; Sheikh, A. D.; Niazi, M. R.; Haque, M. A.; Liu, M.; Arquer, F. P. G. de; Xu, J.; Sun, B.; Voznyy, O.; Gasparini, N.; Baran, D.; Wu, T.; Sargent, E. H.; Amassian, A. Solar Cells: Overcoming the Ambient Manufacturability-Scalability-Performance Bottleneck in Colloidal Quantum Dot Photovoltaics (Adv. Mater. 35/2018). *Adv. Mater.* **2018**, *30* (35), 1870260. https://doi.org/10.1002/ADMA.201870260.

(127) Mei, S.; Yin, Z.; Gu, P.; Wang, H. Q.; Wang, J.; Song, W. Improved Operational Stability of Perovskite Solar Cells via Au Barrier Layer Incorporation. *ACS Appl. Energy Mater.* **2021**, *4* (10), 11062–11068. https://doi.org/10.1021/ACSAEM.1C01993/SUPPL_FILE/AE1C01993_SI_001.PDF.

(128) Thrithamarassery Gangadharan, D.; Ma, D. Searching for Stability at Lower Dimensions: Current Trends and Future Prospects of Layered Perovskite Solar Cells. *Energy Environ. Sci.* **2019**, *12* (10), 2860–2889. https://doi.org/10.1039/C9EE01591D.

(129) Li, Y.; Xu, X.; Wang, C.; Ecker, B.; Yang, J.; Huang, J.; Gao, Y. Light-Induced Degradation of CH3NH3PbI3 Hybrid Perovskite Thin Film. *J. Phys. Chem. C* **2017**, *121* (7), 3904–3910. https://doi.org/10.1021/ACS.JPCC.6B11853/SUPPL_FILE/JP6B11853_SI_001.PDF.

(130) Misra, R. K.; Aharon, S.; Li, B.; Mogilyansky, D.; Visoly-Fisher, I.; Etgar, L.; Katz, E. A. Temperature- and Component-Dependent Degradation of Perovskite Photovoltaic Materials under Concentrated Sunlight. *J. Phys. Chem. Lett.* **2015**, *6* (3), 326–330. https://doi.org/10.1021/JZ502642B/SUPPL_FILE/JZ502642B_SI_001.PDF.

(131) Domanski, K.; Correa-Baena, J. P.; Mine, N.; Nazeeruddin, M. K.; Abate, A.; Saliba, M.; Tress, W.; Hagfeldt, A.; Grätzel, M. Not All That Glitters Is Gold: Metal-Migration-Induced Degradation in Perovskite Solar Cells. *ACS Nano* **2016**, *10* (6), 6306–6314. https://doi.org/10.1021/ACSNANO.6B02613/SUPPL_FILE/NN6B02613_SI_002.MPG.

(132) Lee, S. W.; Kim, S.; Bae, S.; Cho, K.; Chung, T.; Mundt, L. E.; Lee, S.; Park, S.; Park, H.; Schubert, M. C.; Glunz, S. W.; Ko, Y.; Jun, Y.; Kang, Y.; Lee, H. S.; Kim, D. UV Degradation and Recovery of Perovskite Solar Cells. *Sci. Rep. 2016 61* **2016**, *6* (1), 1–10. https://doi.org/10.1038/srep38150.

(133) Ahn, N.; Kwak, K.; Jang, M. S.; Yoon, H.; Lee, B. Y.; Lee, J. K.; Pikhitsa, P. V.; Byun, J.; Choi, M. Trapped Charge-Driven Degradation of Perovskite Solar Cells. *Nat. Commun. 2016 71* **2016**, *7* (1), 1–9. https://doi.org/10.1038/ncomms13422.

(134) Boyd, C. C.; Cheacharoen, R.; Leijtens, T.; McGehee, M. D. Understanding Degradation Mechanisms and Improving Stability of Perovskite Photovoltaics. *Chem. Rev.* **2018**, *119* (5), 3418–3451. https://doi.org/10.1021/ACS.CHEMREV.8B00336.

(135) Rivkin, B.; Fassl, P.; Sun, Q.; Taylor, A. D.; Chen, Z.; Vaynzof, Y. Effect of Ion Migration-Induced Electrode Degradation on the Operational Stability of Perovskite Solar Cells. *ACS Omega* **2018**, *3* (8), 10042–10047. https://doi.org/10.1021/ACSOMEGA.8B01626/SUPPL_FILE/AO8B01626_SI_001.PDF.

(136) Xi, J.; Xi, K.; Sadhanala, A.; Zhang, K. H. L.; Li, G.; Dong, H.; Lei, T.; Yuan, F.; Ran, C.; Jiao, B.; Coxon, P. R.; Harris, C. J.; Hou, X.; Kumar, R. V.; Wu, Z. Chemical Sintering Reduced Grain Boundary Defects for Stable Planar Perovskite Solar Cells. *Nano Energy* **2019**, *56*, 741–750. https://doi.org/10.1016/j.nanoen.2018.11.021.

(137) Guo, Q.; Yuan, F.; Zhang, B.; Zhou, S.; Zhang, J.; Bai, Y.; Fan, L.; Hayat, T.; Alsaedi, A.; Tan, Z. Passivation of the Grain Boundaries of CH 3 NH 3 PbI 3 Using Carbon Quantum Dots for Highly Efficient Perovskite Solar Cells with Excellent Environmental Stability. *Nanoscale* **2018**, *11* (1), 115–124. https://doi.org/10.1039/C8NR08295B.

(138) Niu, T.; Lu, J.; Munir, R.; Li, J.; Barrit, D.; Zhang, X.; Hu, H.; Yang, Z.; Amassian, A.; Zhao, K.; Liu, S. (Frank). Stable High-Performance Perovskite Solar Cells via Grain Boundary Passivation. *Adv. Mater.* **2018**, *30* (16), 1706576. https://doi.org/10.1002/adma.201706576.

(139) Huang, L. B.; Su, P. Y.; Liu, J. M.; Huang, J. F.; Chen, Y. F.; Qin, S.; Guo, J.; Xu, Y. W.; Su, C. Y. Interface Engineering of Perovskite Solar Cells with Multifunctional Polymer Interlayer toward Improved Performance and Stability. *J. Power Sources* **2018**, *378*, 483–490. https://doi.org/10.1016/J.JPOWSOUR.2017.12.082.

(140) Chen, J.; Park, N. G. Materials and Methods for Interface Engineering toward Stable and Efficient Perovskite Solar Cells. *ACS Energy Lett.* **2020**, *5* (8), 2742–2786. https://doi.org/10.1021/ACSENERGYLETT.0C01240.

(141) Bai, Y.; Meng, X.; Yang, S. Interface Engineering for Highly Efficient and Stable Planar P-i-n Perovskite Solar Cells. *Adv. Energy Mater.* **2018**, *8* (5), 1701883. https://doi.org/10.1002/AENM.201701883.

(142) Wang, B.; Yang, J.; Lu, L.; Xiao, W.; Wu, H.; Xiong, S.; Tang, J.; Duan, C.; Bao, Q. Interface Engineering of Air-Stable n-Doping Fullerene-Modified TiO2 Electron

Transport Layer for Highly Efficient and Stable Perovskite Solar Cells. *Adv. Mater. Interfaces* **2020**, *7* (6), 1901964. https://doi.org/10.1002/ADMI.201901964.

(143) Yang, Z.; Babu, B. H.; Wu, S.; Liu, T.; Fang, S.; Xiong, Z.; Han, L.; Chen, W. Review on Practical Interface Engineering of Perovskite Solar Cells: From Efficiency to Stability. *Sol. RRL* **2020**, *4* (2), 1900257. https://doi.org/10.1002/SOLR.201900257.

(144) Boopathi, K. M.; Mohan, R.; Huang, T. Y.; Budiawan, W.; Lin, M. Y.; Lee, C. H.; Ho, K. C.; Chu, C. W. Synergistic Improvements in Stability and Performance of Lead Iodide Perovskite Solar Cells Incorporating Salt Additives. *J. Mater. Chem. A* **2016**, *4* (5), 1591–1597. https://doi.org/10.1039/C5TA10288J.

(145) Yang, Y.; Song, J.; Zhao, Y. L.; Zhu, L.; Gu, X. Q.; Gu, Y. Q.; Che, M.; Qiang, Y. H.; Song, J. Ammonium-Iodide-Salt Additives Induced Photovoltaic Performance Enhancement in One-Step Solution Process for Perovskite Solar Cells. *J. Alloys Compd.* **2016**, *684*, 84–90. https://doi.org/10.1016/J.JALLCOM.2016.05.154.

(146) Matteocci, F.; Cinà, L.; Lamanna, E.; Cacovich, S.; Divitini, G.; Midgley, P. A.; Ducati, C.; Di Carlo, A. Encapsulation for Long-Term Stability Enhancement of Perovskite Solar Cells. *Nano Energy* **2016**, *30*, 162–172. https://doi.org/10.1016/J.NANOEN.2016.09.041.

(147) Das, C.; Kot, M.; Hellmann, T.; Wittich, C.; Mankel, E.; Zimmermann, I.; Schmeisser, D.; Khaja Nazeeruddin, M.; Jaegermann, W. Atomic Layer-Deposited Aluminum Oxide Hinders Iodide Migration and Stabilizes Perovskite Solar Cells. *Cell Rep. Phys. Sci.* **2020**, *1* (7), 100112. https://doi.org/10.1016/J.XCRP.2020.100112.

(148) Mei, Y.; Shen, Z.; Kundu, S.; Dennis, E.; Pang, S.; Tan, F.; Yue, G.; Gao, Y.; Dong, C.; Liu, R.; Zhang, W.; Saidaminov, M. I. Perovskite Solar Cells with Polyaniline Hole Transport Layers Surpassing a 20% Power Conversion Efficiency. *Chem. Mater.* **2021**, *33* (12), 4679–4687. https://doi.org/10.1021/ACS.CHEMMATER.1C01176/SUPPL_FILE/CM1C01176_SI_001.PDF.

(149) Chang, C. Y.; Lee, K. T.; Huang, W. K.; Siao, H. Y.; Chang, Y. C. High-Performance, Air-Stable, Low-Temperature Processed Semitransparent Perovskite Solar Cells Enabled by Atomic Layer Deposition. *Chem. Mater.* **2015**, *27* (14), 5122–5130. https://doi.org/10.1021/ACS.CHEMMATER.5B01933/SUPPL_FILE/CM5B01933_SI_001.PDF.

(150) Jeon, N. J.; Noh, J. H.; Kim, Y. C.; Yang, W. S.; Ryu, S.; Seok, S. I. Solvent Engineering for High-Performance Inorganic–Organic Hybrid Perovskite Solar Cells. *Nat. Mater. 2014 139* **2014**, *13* (9), 897–903. https://doi.org/10.1038/nmat4014.

(151) Xu, Q.; Wang, J.; Shao, W.; Ouyang, X.; Wang, X.; Zhang, X.; Guo, Y.; Ouyang, X. A Solution-Processed Zero-Dimensional All-Inorganic Perovskite Scintillator for High Resolution Gamma-Ray Spectroscopy Detection. *Nanoscale* **2020**, *12* (17), 9727–9732. https://doi.org/10.1039/D0NR00772B.

(152) Mishra, G.; Tripathi, S. N.; Saud, T.; Joshi, M.; Khan, A.; Sapra, B. K. Study on CCN Activity of Fission Product Aerosols (CsI and CsOH) and Their Effect on Size and Other Properties. *Atmospheric Res.* **2020**, *236*, 104816. https://doi.org/10.1016/J.ATMOSRES.2019.104816.

(153) Ma, F.; Li, J.; Li, W.; Lin, N.; Wang, L.; Qiao, J. Stable α/δ Phase Junction of Formamidinium Lead Iodide Perovskites for Enhanced near-Infrared Emission. *Chem. Sci.* **2016**, *8* (1), 800–805. https://doi.org/10.1039/C6SC03542F.

(154) Mater, J.; Chem, C.; Guo, J.; Tang, Y.; Li, L.; Jia, P.; Song, B.; Liu, X.; Li, X.; Deng, Z.; Lou, Z.; Hu, Y.; Teng, F.; Qin, L.; Hou, Y. Aspect-Ratio Controllable Growth of Rectangular Cesium Lead Bromide Crystallites on PTAA Modified Substrates. *J. Mater. Chem. C* **2022**. https://doi.org/10.1039/D2TC00651K.

(155) Oscar Telschow; Miguel Albaladejo-Siguan; Lena Merten; D. Taylor, A.; P. Goetz, K.; Tim Schramm; V. Konovalov, O.; Maciej Jankowski; Alexander Hinderhofer; Fabian Paulus; Frank Schreiber; Yana Vaynzof. Preserving the Stoichiometry of Triple-Cation Perovskites by Carrier-Gas-Free Antisolvent Spraying. *J. Mater. Chem. A* **2022**. https://doi.org/10.1039/D1TA10566C.

(156) Duan, L.; Uddin, A. Defects and Stability of Perovskite Solar Cells: A Critical Analysis. *Mater. Chem. Front.* **2022**, *6* (4), 400–417. https://doi.org/10.1039/D1QM01250A.

(157) Ramasamy, E.; Karthikeyan, V.; Rameshkumar, K.; Veerappan, G. Glass-to-Glass Encapsulation with Ultraviolet Light Curable Epoxy Edge Sealing for Stable Perovskite Solar Cells. *Mater. Lett.* **2019**, *250*, 51–54. https://doi.org/10.1016/J.MATLET.2019.04.082.

(158) Shi, L.; Bucknall, M. P.; Young, T. L.; Zhang, M.; Hu, L.; Bing, J.; Lee, D. S.; Kim, J.; Wu, T.; Takamure, N.; McKenzie, D. R.; Huang, S.; Green, M. A.; Ho-Baillie, A. W. Y. Gas Chromatography-Mass Spectrometry Analyses of Encapsulated Stable Perovskite Solar Cells. *Science* **2020**, *368* (6497). https://doi.org/10.1126/SCIENCE.ABA2412/SUPPL_FILE/ABA2412_SHI_SM.PDF.

(159) Aitola, K.; Gava Sonai, G.; Markkanen, M.; Jaqueline Kaschuk, J.; Hou, X.; Miettunen, K.; Lund, P. D. Encapsulation of Commercial and Emerging Solar Cells with Focus on Perovskite Solar Cells. *Sol. Energy* **2022**, *237*, 264–283. https://doi.org/10.1016/J.SOLENER.2022.03.060.

(160) Zhao, X.; Liu, T.; Burlingame, Q. C.; Liu, T.; HolleyIII, R.; Cheng, G.; Yao, N.; Gao, F.; Loo, Y.-L. Accelerated Aging of All-Inorganic, Interface-Stabilized Perovskite Solar Cells. *Science* **2022**. https://doi.org/10.1126/SCIENCE.ABN5679.

(161) Nie, W.; Blancon, J. C.; Neukirch, A. J.; Appavoo, K.; Tsai, H.; Chhowalla, M.; Alam, M. A.; Sfeir, M. Y.; Katan, C.; Even, J.; Tretiak, S.; Crochet, J. J.; Gupta, G.; Mohite, A. D. Light-Activated Photocurrent Degradation and Self-Healing in Perovskite Solar Cells. *Nat. Commun. 2016 71* **2016**, *7* (1), 1–9. https://doi.org/10.1038/ncomms11574.

(162) Awais, M.; Kirsch, R. L.; Yeddu, V.; Saidaminov, M. I. Tin Halide Perovskites Going Forward: Frost Diagrams Offer Hints. *ACS Mater. Lett.* **2021**, *3* (3), 299–307. https://doi.org/10.1021/ACSMATERIALSLETT.0C00571/ASSET/IMAGES/LARGE/TZ0C00571_0004.JPEG.

(163) Tailor, N. K.; Kar, S.; Mishra, P.; These, A.; Kupfer, C.; Hu, H.; Awais, M.; Saidaminov, M.; Dar, M. I.; Brabec, C.; Satapathi, S. Advances in Lead-Free Perovskite Single Crystals: Fundamentals and Applications. *ACS Mater. Lett.* **2021**, *3*, 1025–1080. https://doi.org/10.1021/ACSMATERIALSLETT.1C00242/ASSET/IMAGES/LARGE/TZ1C00242_0037.JPEG.

(164) Ahmed, Y.; Khan, B.; Bilal Faheem, M.; Huang, K.; Gao, Y.; Yang, J. Organic Additives in All-Inorganic Perovskite Solar Cells and Modules: From Moisture Endurance to Enhanced Efficiency and Operational Stability. *J. Energy Chem.* **2022**, *67*, 361–390. https://doi.org/10.1016/J.JECHEM.2021.09.047.

(165) Liu, D.; Zheng, H.; Ahmed, Y.; Zheng, C.; Wang, Y.; Chen, H.; Chen, L.; Li, S. Enhanced Photovoltaic Performance of SnO2 Based Flexible Perovskite Solar Cells via Introducing Interfacial Dipolar Layer and Defect Passivation. *J. Power Sources* **2022**, *519*, 230814. https://doi.org/10.1016/J.JPOWSOUR.2021.230814.

(166) Aldamasy, M.; Iqbal, Z.; Li, G.; Pascual, J.; Alharthi, F.; Abate, A.; Li, M. Challenges in Tin Perovskite Solar Cells. *Phys. Chem. Chem. Phys.* **2021**, *23* (41), 23413–23427. https://doi.org/10.1039/D1CP02596A.

(167) Ullah, A.; Park, K. H.; Lee, Y. W.; Park, S.; Faheem, A. B.; Nguyen, H. D.; Siddique, Y.; Lee, K. K.; Jo, Y.; Han, C. H.; Ahn, S. J.; Jeong, I.; Cho, S.; Kim, B. S.; Park, Y. S.; Hong, S. Versatile Hole Selective Molecules Containing a Series of Heteroatoms as Self-Assembled Monolayers for Efficient p-i-n Perovskite and Organic Solar Cells. *Adv. Funct. Mater.* **2022**, *32* (49), 2208793. https://doi.org/10.1002/ADFM.202208793.

(168) Xu, B.; Liu, D.; Dong, C.; Awais, M.; Wang, W.; Song, Y.; Deng, Y.; Yao, M.; Tong, J.; Yue, G.; Zhang, W.; Tan, F.; Saidaminov, M. I. NiOx for Interface and Work Function Engineering in Carbon-Based All-Inorganic Perovskite Solar Cells. *J. Colloid Interface Sci.* **2023**, *641*, 105–112. https://doi.org/10.1016/J.JCIS.2023.03.049.

(169) Finkenauer, B. P.; Gao, Y.; Wang, X.; Tian, Y.; Wei, Z.; Zhu, C.; Rokke, D. J.; Jin, L.; Meng, L.; Yang, Y.; Huang, L.; Zhao, K.; Dou, L. Mechanically Robust and Self-Healable Perovskite Solar Cells. *Cell Rep. Phys. Sci.* **2021**, *2* (2). https://doi.org/10.1016/j.xcrp.2020.100320.

(170) Wang, H. Q.; Wang, S.; Chen, L.; Yin, Z.; Mei, S.; Zhong, Y.; Yao, Y.; Li, N.; Wang, J.; Song, W. Understanding Degradation Mechanisms of Perovskite Solar Cells Due to Electrochemical Metallization Effect. *Sol. Energy Mater. Sol. Cells* **2021**, *230*, 111278. https://doi.org/10.1016/J.SOLMAT.2021.111278.

(171) Liu, J.; Pathak, S. K.; Sakai, N.; Sheng, R.; Bai, S.; Wang, Z.; Snaith, H. J. Identification and Mitigation of a Critical Interfacial Instability in Perovskite Solar Cells Employing Copper Thiocyanate Hole-Transporter. *Adv. Mater. Interfaces* **2016**, *3* (22), 1600571. https://doi.org/10.1002/ADMI.201600571.

(172) Leijtens, T.; Eperon, G. E.; Pathak, S.; Abate, A.; Lee, M. M.; Snaith, H. J. Overcoming Ultraviolet Light Instability of Sensitized TiO2 with Meso-Superstructured Organometal Tri-Halide Perovskite Solar Cells. *Nat. Commun. 2013 41* **2013**, *4* (1), 1–8. https://doi.org/10.1038/ncomms3885.

(173) Khenkin, M. V.; Katz, E. A.; Abate, A.; Bardizza, G.; Berry, J. J.; Brabec, C.; Brunetti, F.; Bulović, V.; Burlingame, Q.; Di Carlo, A.; Cheacharoen, R.; Cheng, Y. B.; Colsmann, A.; Cros, S.; Domanski, K.; Dusza, M.; Fell, C. J.; Forrest, S. R.; Galagan, Y.; Di Girolamo, D.; Grätzel, M.; Hagfeldt, A.; von Hauff, E.; Hoppe, H.; Kettle, J.; Köbler, H.; Leite, M. S.; Liu, S. (Frank); Loo, Y. L.; Luther, J. M.; Ma, C. Q.; Madsen, M.; Manceau, M.; Matheron, M.; McGehee, M.; Meitzner, R.; Nazeeruddin, M. K.; Nogueira, A. F.; Odabaşı, Ç.; Osherov, A.; Park, N. G.; Reese, M. O.; De Rossi, F.; Saliba, M.; Schubert, U. S.; Snaith, H. J.; Stranks, S. D.; Tress, W.; Troshin, P. A.; Turkovic, V.; Veenstra, S.;

Visoly-Fisher, I.; Walsh, A.; Watson, T.; Xie, H.; Yıldırım, R.; Zakeeruddin, S. M.; Zhu, K.; Lira-Cantu, M. Consensus Statement for Stability Assessment and Reporting for Perovskite Photovoltaics Based on ISOS Procedures. *Nat. Energy 2020 51* **2020**, *5* (1), 35–49. https://doi.org/10.1038/s41560-019-0529-5.

(174) Yoo, J. J.; Seo, G.; Chua, M. R.; Park, T. G.; Lu, Y.; Rotermund, F.; Kim, Y. K.; Moon, C. S.; Jeon, N. J.; Correa-Baena, J. P.; Bulović, V.; Shin, S. S.; Bawendi, M. G.; Seo, J. Efficient Perovskite Solar Cells via Improved Carrier Management. *Nat. 2021 5907847* **2021**, *590* (7847), 587–593. https://doi.org/10.1038/s41586-021-03285-w.

(175) Nazir, G.; Lee, S.-Y.; Lee, J.-H.; Rehman, A.; Lee, J.-K.; Seok, S. I.; Park, S.-J.; Nazir, G.; Lee, S.-Y.; Lee, J.-H.; Rehman, A.; Park, S.-J.; Lee, J.-K.; Seok, S. I. Stabilization of Perovskite Solar Cells: Recent Developments and Future Perspectives. *Adv. Mater.* **2022**, *34* (50), 2204380. https://doi.org/10.1002/ADMA.202204380.

(176) Fu, W.; Ricciardulli, A. G.; Akkerman, Q. A.; John, R. A.; Tavakoli, M. M.; Essig, S.; Kovalenko, M. V.; Saliba, M. Stability of Perovskite Materials and Devices. *Mater. Today* **2022**, *58*, 275–296. https://doi.org/10.1016/J.MATTOD.2022.06.020.

(177) Quan, L. N.; Rand, B. P.; Friend, R. H.; Mhaisalkar, S. G.; Lee, T. W.; Sargent, E. H. Perovskites for Next-Generation Optical Sources. *Chem. Rev.* **2019**, *119* (12), 7444–7477. https://doi.org/10.1021/ACS.CHEMREV.9B00107/ASSET/IMAGES/LARGE/CR-2019-00107T_0028.JPEG.

(178) Kundu, S.; Zhang, D.; Askar, A. M.; Moloney, E. G.; Adachi, M. M.; Nadeem, A.; Moradi, S.; Yeddu, V.; Abdelhady, A. L.; Voznyy, O.; Saidaminov, M. I. Bismuth Stabilizes the α-Phase of Formamidinium Lead Iodide Perovskite Single Crystals. *ACS Mater. Lett.* **2022**, *4* (4), 707–712. https://doi.org/10.1021/ACSMATERIALSLETT.1C00778/ASSET/IMAGES/MEDIUM/TZ1C00778_M001.GIF.

(179) Wang, S.; Cabreros, A.; Yang, Y.; Hall, A. S.; Valenzuela, S.; Luo, Y.; Correa-Baena, J. P.; Kim, M. cheol; Fjeldberg, Ø.; Fenning, D. P.; Meng, Y. S. Impacts of the Hole Transport Layer Deposition Process on Buried Interfaces in Perovskite Solar Cells. *Cell Rep. Phys. Sci.* **2020**, *1* (7). https://doi.org/10.1016/j.xcrp.2020.100103.

(180) Wu, Z.; Alsalloum, A. Y.; Mohammed, O. F.; Bakr, O. M. Soft Perovskites Stabilized by Robust Heterojunctions. *Joule* **2022**, *6* (5), 951–952. https://doi.org/10.1016/J.JOULE.2022.04.015.

(181) Wu, T.; Qin, Z.; Wang, Y.; Wu, Y.; Chen, W.; Zhang, S.; Cai, M.; Dai, S.; Zhang, J.; Liu, J.; Zhou, Z.; Liu, X.; Segawa, H.; Tan, H.; Tang, Q.; Fang, J.; Li, Y.; Ding, L.; Ning, Z.; Qi, Y.; Zhang, Y.; Han, L. The Main Progress of Perovskite Solar Cells in 2020–2021. *Nano-Micro Lett. 2021 131* **2021**, *13* (1), 1–18. https://doi.org/10.1007/S40820-021-00672-W.

(182) Babics, M.; De Bastiani, M.; Ugur, E.; Xu, L.; Bristow, H.; Toniolo, F.; Raja, W.; Subbiah, A. S.; Liu, J.; Torres Merino, L. V.; Aydin, E.; Sarwade, S.; Allen, T. G.; Razzaq, A.; Wehbe, N.; Salvador, M. F.; De Wolf, S. One-Year Outdoor Operation of Monolithic Perovskite/Silicon Tandem Solar Cells. *Cell Rep. Phys. Sci.* **2023**, *4* (2). https://doi.org/10.1016/j.xcrp.2023.101280.

(183) Mali, S. S.; Patil, J. V.; Park, D. W.; Jung, Y. H.; Hong, C. K. Intrinsic and Extrinsic Stability of Triple-Cation Perovskite Solar Cells through Synergistic Influence of

Organic Additive. *Cell Rep. Phys. Sci.* **2022**, *3* (6). https://doi.org/10.1016/j.xcrp.2022.100906.

(184) Ka, I.; Asuo, I. M.; Nechache, R.; Rosei, F. Highly Stable Air Processed Perovskite Solar Cells by Interfacial Layer Engineering. *Chem. Eng. J.* **2021**, *423*. https://doi.org/10.1016/j.cej.2021.130334.

(185) Byranvand, M. M.; Saliba, M. Defect Passivation of Perovskite Films for Highly Efficient and Stable Solar Cells. *Sol. RRL* **2021**, *5* (8). https://doi.org/10.1002/solr.202100295.

(186) Lu, H.; Krishna, A.; Zakeeruddin, S. M.; Grätzel, M.; Hagfeldt, A. Compositional and Interface Engineering of Organic-Inorganic Lead Halide Perovskite Solar Cells. *iScience* **2020**, *23* (8), 101359. https://doi.org/10.1016/J.ISCI.2020.101359.

(187) Jeon, N. J.; Noh, J. H.; Yang, W. S.; Kim, Y. C.; Ryu, S.; Seo, J.; Seok, S. I. Compositional Engineering of Perovskite Materials for High-Performance Solar Cells. *Nat. 2015 5177535* **2015**, *517* (7535), 476–480. https://doi.org/10.1038/nature14133.

(188) Jiang, Q.; Zhao, Y.; Zhang, X.; Yang, X.; Chen, Y.; Chu, Z.; Ye, Q.; Li, X.; Yin, Z.; You, J. Surface Passivation of Perovskite Film for Efficient Solar Cells. *Nat. Photonics 2019 137* **2019**, *13* (7), 460–466. https://doi.org/10.1038/s41566-019-0398-2.

(189) Zheng, X.; Chen, B.; Dai, J.; Fang, Y.; Bai, Y.; Lin, Y.; Wei, H.; Zeng, X. C.; Huang, J. Defect Passivation in Hybrid Perovskite Solar Cells Using Quaternary Ammonium Halide Anions and Cations. *Nat. Energy 2017 27* **2017**, *2* (7), 1–9. https://doi.org/10.1038/nenergy.2017.102.

(190) Fakharuddin, A.; Schmidt-Mende, L.; Garcia-Belmonte, G.; Jose, R.; Mora-Sero, I. Interfaces in Perovskite Solar Cells. *Adv. Energy Mater.* **2017**, *7* (22), 1700623. https://doi.org/10.1002/AENM.201700623.

(191) Li, X.; Ibrahim Dar, M.; Yi, C.; Luo, J.; Tschumi, M.; Zakeeruddin, S. M.; Nazeeruddin, M. K.; Han, H.; Grätzel, M. Improved Performance and Stability of Perovskite Solar Cells by Crystal Crosslinking with Alkylphosphonic Acid ω-Ammonium Chlorides. *Nat. Chem. 2015 79* **2015**, *7* (9), 703–711. https://doi.org/10.1038/nchem.2324.

(192) Castro-Méndez, A. F.; Hidalgo, J.; Correa-Baena, J. P. The Role of Grain Boundaries in Perovskite Solar Cells. *Adv. Energy Mater.* **2019**, *9* (38), 1901489. https://doi.org/10.1002/AENM.201901489.

(193) Arabpour Roghabadi, F.; Mansour Rezaei Fumani, N.; Alidaei, M.; Ahmadi, V.; Sadrameli, S. M. High Power UV-Light Irradiation as a New Method for Defect Passivation in Degraded Perovskite Solar Cells to Recover and Enhance the Performance. *Sci. Rep. 2019 91* **2019**, *9* (1), 1–11. https://doi.org/10.1038/s41598-019-45756-1.

(194) Wenson, G.; Thakkar, H.; Tsai, H.; Stein, J.; Singh, R.; Nie, W. The Degradation and Recovery Behavior of Mixed-Cation Perovskite Solar Cells in Moisture and a Gas Mixture Environment. *J. Mater. Chem. A* **2022**, *10* (25), 13519–13526. https://doi.org/10.1039/D2TA02352K.

(195) Kundu, S.; Kelly, T. L. In Situ Studies of the Degradation Mechanisms of Perovskite Solar Cells. *EcoMat* **2020**, *2* (2), e12025. https://doi.org/10.1002/EOM2.12025.

(196) Frost, J. M.; Butler, K. T.; Brivio, F.; Hendon, C. H.; Van Schilfgaarde, M.; Walsh, A. Atomistic Origins of High-Performance in Hybrid Halide Perovskite Solar Cells. *Nano*

Lett. **2014**, *14* (5), 2584–2590. https://doi.org/10.1021/NL500390F/SUPPL_FILE/NL500390F_SI_001.PDF.

(197) Jiao, H.; Ni, Z.; Shi, Z.; Fei, C.; Liu, Y.; Dai, X.; Huang, J. Perovskite Grain Wrapping by Converting Interfaces and Grain Boundaries into Robust and Water-Insoluble Low-Dimensional Perovskites. *Sci. Adv.* **2022**, *8* (48), eabq4524. https://doi.org/10.1126/SCIADV.ABQ4524/SUPPL_FILE/SCIADV.ABQ4524_DATA_S1.ZIP.

(198) Qiu, L.; Li, H.; Dai, F.; Ouyang, F.; Pang, D.; Wang, H. Adsorption and Photocatalytic Degradation of Benzene Compounds on Acidic F-TiO2/SiO2 Catalyst. *Chemosphere* **2020**, *246*, 125698. https://doi.org/10.1016/J.CHEMOSPHERE.2019.125698.

(199) Kang, Y. J.; Na, S. I. Multi-Site Passivation-Based Antisolvent Additive Engineering with Gradient Distribution for Superior Triple Cation P-I-N Perovskite Solar Cells. *Nano Energy* **2022**, *97*, 107193. https://doi.org/10.1016/J.NANOEN.2022.107193.

(200) Awais, M.; Thrithamarassery Gangadharan, D.; Tan, F.; Saidaminov, M. I. How to Make 20% Efficient Perovskite Solar Cells in Ambient Air and Encapsulate Them for 500 h of Operational Stability. *Chem. Mater.* **2022**, *34* (18), 8112–8118. https://doi.org/10.1021/ACS.CHEMMATER.2C01422/ASSET/IMAGES/LARGE/CM2C01422_0006.JPEG.

(201) Huang, J.-J.; Ou, S.-L.; Hsu, C.-F.; Shen, X.-Q. The Effect of Boric Acid Concentration on the TiO2 Compact Layer by Liquid-Phase Deposition for Dye-Sensitized Solar Cell. *Appl. Surf. Sci.* **2019**, *477*, 7–14. https://doi.org/10.1016/j.apsusc.2018.05.113.

(202) Sidhik, S.; Wang, Y.; De Siena, M.; Asadpour, R.; Torma, A. J.; Terlier, T.; Ho, K.; Li, W.; Puthirath, A. B.; Shuai, X.; Agrawal, A.; Traore, B.; Jones, M.; Giridharagopal, R.; Ajayan, P. M.; Strzalka, J.; Ginger, D. S.; Katan, C.; Alam, M. A.; Even, J.; Kanatzidis, M. G.; Mohite, A. D. Deterministic Fabrication of 3D/2D Perovskite Bilayer Stacks for Durable and Efficient Solar Cells. *Science* **2022**, *377* (6613), 1425–1430. https://doi.org/10.1126/SCIENCE.ABQ7652/SUPPL_FILE/SCIENCE.ABQ7652_MOVIES_S1_AND_S2.ZIP.

(203) Jiang, X.; Chen, S.; Li, Y.; Zhang, L.; Shen, N.; Zhang, G.; Du, J.; Fu, N.; Xu, B. Direct Surface Passivation of Perovskite Film by 4-Fluorophenethylammonium Iodide toward Stable and Efficient Perovskite Solar Cells. *ACS Appl. Mater. Interfaces* **2021**, *13* (2), 2558–2565. https://doi.org/10.1021/acsami.0c17773.

(204) Azmi, R.; Ugur, E.; Seitkhan, A.; Aljamaan, F.; Subbiah, A. S.; Liu, J.; Harrison, G. T.; Nugraha, M. I.; Eswaran, M. K.; Babics, M.; Chen, Y.; Xu, F.; Allen, T. G.; ur Rehman, A.; Wang, C. L.; Anthopoulos, T. D.; Schwingenschlögl, U.; De Bastiani, M.; Aydin, E.; De Wolf, S. Damp Heat-Stable Perovskite Solar Cells with Tailored-Dimensionality 2D/3D Heterojunctions. *Science* **2022**, *376* (6588), 73–77. https://doi.org/10.1126/SCIENCE.ABM5784/SUPPL_FILE/SCIENCE.ABM5784_SM.PDF.

(205) Li, Q.; Zheng, Y.; Wei, Z.; Xie, J.; Zou, C.; Liu, X.; Liu, D.; Zhou, Z.; Yang, H. G.; Yang, S.; Hou, Y. Halide Diffusion Equilibrium and Its Impact on Efficiency Evolution of Perovskite Solar Cells. *Adv. Energy Mater.* **2022**, *12* (48), 2202982. https://doi.org/10.1002/aenm.202202982.

(206) Nayak, S. K.; Sathishkumar, R.; Row, T. N. G. Directing Role of Functional Groups in Selective Generation of C–H⋯π Interactions: In Situ Cryo-Crystallographic Studies on Benzyl Derivatives. *CrystEngComm* **2010**, *12* (10), 3112–3118. https://doi.org/10.1039/C001190H.

(207) Mi, C.; Gee, G. C.; Lander, C. W.; Shin, D.; Atteberry, M. L.; Akhmedov, N. G.; Hidayatova, L.; DiCenso, J. D.; Yip, W. T.; Chen, B.; Shao, Y.; Dong, Y. Towards Non-Blinking and Photostable Perovskite Quantum Dots. *Nat. Commun.* **2025**, *16* (1), 204. https://doi.org/10.1038/s41467-024-55619-7.

(208) Zhang, Y.; Wang, R.; Lu, H.; Chen, M.; Wang, H.; He, T.; Shao, T.; Liu, Y.; Chen, Y.; Long, G. Alkyl Fluorination Aromatic Acetamidine Cation Enhances the Lattice Stability and Performance of 2D Ruddlesden-Popper Perovskite Solar Cells. *Small* **2025**, *21* (11), 2410546. https://doi.org/10.1002/smll.202410546.

(209) Zhou, H.; Chen, Q.; Li, G.; Luo, S.; Song, T.; Duan, H.-S.; Hong, Z.; You, J.; Liu, Y.; Yang, Y. Interface Engineering of Highly Efficient Perovskite Solar Cells. *Science* **2014**, *345* (6196), 542–546. https://doi.org/10.1126/science.1254050.

(210) Awais, M.; Kundu, S.; Zhang, D.; Yeddu, V.; Kokaba, M. R.; Ahmed, Y.; Zhou, W.; Dayneko, S.; Tan, F.; Saidaminov, M. I. Selective Deactivation of Perovskite Grain Boundaries. *Cell Rep. Phys. Sci.* **2023**, *4* (10). https://doi.org/10.1016/j.xcrp.2023.101634.

(211) Lee, J. H.; Lee, S.; Kim, T.; Ahn, H.; Jang, G. Y.; Kim, K. H.; Cho, Y. J.; Zhang, K.; Park, J.-S.; Park, J. H. Interfacial α-FAPbI3 Phase Stabilization by Reducing Oxygen Vacancies in SnO2−x. *Joule* **2023**, *7* (2), 380–397. https://doi.org/10.1016/j.joule.2022.12.006.

(212) Seo, J.-Y.; Matsui, T.; Luo, J.; Correa-Baena, J.-P.; Giordano, F.; Saliba, M.; Schenk, K.; Ummadisingu, A.; Domanski, K.; Hadadian, M.; Hagfeldt, A.; Zakeeruddin, S. M.; Steiner, U.; Grätzel, M.; Abate, A. Ionic Liquid Control Crystal Growth to Enhance Planar Perovskite Solar Cells Efficiency. *Adv. Energy Mater.* **2016**, *6* (20), 1600767. https://doi.org/10.1002/aenm.201600767.

(213) Li, Z.; Li, P.; Chen, G.; Cheng, Y.; Pi, X.; Yu, X.; Yang, D.; Han, L.; Zhang, Y.; Song, Y. Ink Engineering of Inkjet Printing Perovskite. *ACS Appl. Mater. Interfaces* **2020**, *12* (35), 39082–39091. https://doi.org/10.1021/acsami.0c09485.

(214) Bi, D.; Yi, C.; Luo, J.; Décoppet, J.-D.; Zhang, F.; Zakeeruddin, S. M.; Li, X.; Hagfeldt, A.; Grätzel, M. Polymer-Templated Nucleation and Crystal Growth of Perovskite Films for Solar Cells with Efficiency Greater than 21%. *Nat. Energy* **2016**, *1* (10), 16142. https://doi.org/10.1038/nenergy.2016.142.

(215) Yoo, J. J.; Seo, G.; Chua, M. R.; Park, T. G.; Lu, Y.; Rotermund, F.; Kim, Y.-K.; Moon, C. S.; Jeon, N. J.; Correa-Baena, J.-P.; Bulović, V.; Shin, S. S.; Bawendi, M. G.; Seo, J. Efficient Perovskite Solar Cells via Improved Carrier Management. *Nature* **2021**, *590* (7847), 587–593. https://doi.org/10.1038/s41586-021-03285-w.

(216) Zhao, Q.; Zhang, B.; Hui, W.; Su, Z.; Wang, H.; Zhang, Q.; Gao, K.; Zhang, X.; Li, B.; Gao, X.; Wang, X.; De Wolf, S.; Wang, K.; Pang, S. Oxygen Vacancy Mediation in SnO2 Electron Transport Layers Enables Efficient, Stable, and Scalable Perovskite Solar Cells. *J. Am. Chem. Soc.* **2024**, *146* (28), 19108–19117. https://doi.org/10.1021/jacs.4c03783.

(217) Lv, S.; Wei, Y.; Chen, J.; Cai, Y.; Wu, D.; Huang, Y.; Fan, L.; Wu, J. Co3O4 Assisted Chemical Bath Deposition of SnO2 ETL for Efficient and Stable Perovskite Solar Cells. *J. Power Sources* **2025**, *629*, 236033. https://doi.org/10.1016/j.jpowsour.2024.236033.

(218) E. Courtier, N.; M. Cave, J.; M. Foster, J.; B. Walker, A.; Richardson, G. How Transport Layer Properties Affect Perovskite Solar Cell Performance: Insights from a Coupled Charge Transport/Ion Migration Model. *Energy Environ. Sci.* **2019**, *12* (1), 396–409. https://doi.org/10.1039/C8EE01576G.

(219) Malinkiewicz, O.; Yella, A.; Lee, Y. H.; Espallargas, G. M.; Graetzel, M.; Nazeeruddin, M. K.; Bolink, H. J. Perovskite Solar Cells Employing Organic Charge-Transport Layers. *Nat. Photonics* **2014**, *8* (2), 128–132. https://doi.org/10.1038/nphoton.2013.341.

(220) Shin, S. S.; Lee, S. J.; Seok, S. I. Metal Oxide Charge Transport Layers for Efficient and Stable Perovskite Solar Cells. *Adv. Funct. Mater.* **2019**, *29* (47), 1900455. https://doi.org/10.1002/adfm.201900455.

(221) You, J.; Meng, L.; Song, T.-B.; Guo, T.-F.; Yang, Y. (Michael); Chang, W.-H.; Hong, Z.; Chen, H.; Zhou, H.; Chen, Q.; Liu, Y.; De Marco, N.; Yang, Y. Improved Air Stability of Perovskite Solar Cells via Solution-Processed Metal Oxide Transport Layers. *Nat. Nanotechnol.* **2016**, *11* (1), 75–81. https://doi.org/10.1038/nnano.2015.230.

(222) Ren, X.; Wang, Z. S.; Choy, W. C. H. Device Physics of the Carrier Transporting Layer in Planar Perovskite Solar Cells. *Adv. Opt. Mater.* **2019**, *7* (20), 1900407. https://doi.org/10.1002/adom.201900407.

(223) Xiong, L.; Guo, Y.; Wen, J.; Liu, H.; Yang, G.; Qin, P.; Fang, G. Review on the Application of SnO2 in Perovskite Solar Cells. *Adv. Funct. Mater.* **2018**, *28* (35), 1802757. https://doi.org/10.1002/adfm.201802757.

(224) Park, S. Y.; Zhu, K. Advances in SnO2 for Efficient and Stable n–i–p Perovskite Solar Cells. *Adv. Mater.* **2022**, *34* (27), 2110438. https://doi.org/10.1002/adma.202110438.

(225) Min, H.; Lee, D. Y.; Kim, J.; Kim, G.; Lee, K. S.; Kim, J.; Paik, M. J.; Kim, Y. K.; Kim, K. S.; Kim, M. G.; Shin, T. J.; Il Seok, S. Perovskite Solar Cells with Atomically Coherent Interlayers on SnO2 Electrodes. *Nature* **2021**, *598* (7881), 444–450. https://doi.org/10.1038/s41586-021-03964-8.

(226) Gil, B.; Yun, A. J.; Lim, J.; Cho, J.; Kim, B.; Ryu, S.; Kim, J.; Park, B. Design of SnO2 Electron Transport Layer in Perovskite Solar Cells to Achieve 2000 h Stability Under 1 Sun Illumination and 85 °C. *Adv. Mater. Interfaces* **2023**, *10* (11), 2202148. https://doi.org/10.1002/admi.202202148.

(227) Lee, S.-U.; Park, H.; Shin, H.; Park, N.-G. Atomic Layer Deposition of SnO2 Using Hydrogen Peroxide Improves the Efficiency and Stability of Perovskite Solar Cells. *Nanoscale* **2023**, *15* (10), 5044–5052. https://doi.org/10.1039/D2NR06884B.

(228) Baena, J. P. C.; Steier, L.; Tress, W.; Saliba, M.; Neutzner, S.; Matsui, T.; Giordano, F.; Jesper Jacobsson, T.; Kandada, A. R. S.; M. Zakeeruddin, S.; Petrozza, A.; Abate, A.; Khaja Nazeeruddin, M.; Grätzel, M.; Hagfeldt, A. Highly Efficient Planar Perovskite Solar Cells through Band Alignment Engineering. *Energy Environ. Sci.* **2015**, *8* (10), 2928–2934. https://doi.org/10.1039/C5EE02608C.

(229) Bai, G.; Wu, Z.; Li, J.; Bu, T.; Li, W.; Li, W.; Huang, F.; Zhang, Q.; Cheng, Y.-B.; Zhong, J. High Performance Perovskite Sub-Module with Sputtered SnO2 Electron Transport Layer. *Sol. Energy* **2019**, *183*, 306–314. https://doi.org/10.1016/j.solener.2019.03.026.

(230) Qiu, L.; Liu, Z.; Ono, L. K.; Jiang, Y.; Son, D.-Y.; Hawash, Z.; He, S.; Qi, Y. Scalable Fabrication of Stable High Efficiency Perovskite Solar Cells and Modules Utilizing Room Temperature Sputtered SnO2 Electron Transport Layer. *Adv. Funct. Mater.* **2019**, *29* (47), 1806779. https://doi.org/10.1002/adfm.201806779.

(231) Wu, Z.; Su, J.; Chai, N.; Cheng, S.; Wang, X.; Zhang, Z.; Liu, X.; Zhong, H.; Yang, J.; Wang, Z.; Liu, J.; Li, X.; Lin, H. Periodic Acid Modification of Chemical-Bath Deposited SnO2 Electron Transport Layers for Perovskite Solar Cells and Mini Modules. *Adv. Sci.* **2023**, *10* (20), 2300010. https://doi.org/10.1002/advs.202300010.

(232) Tay, D. J. J.; Febriansyah, B.; Salim, T.; Wong, Z. S.; Dewi, H. A.; Koh, T. M.; Mathews, N. Enabling a Rapid SnO2 Chemical Bath Deposition Process for Perovskite Solar Cells. *Sustain. Energy Fuels* **2023**, *7* (5), 1302–1310. https://doi.org/10.1039/D2SE01475K.

(233) Du, B.; He, K.; Tian, G.; Che, X.; Song, L. Robust Electron Transport Layers of SnO2 for Efficient Perovskite Solar Cells: Recent Advances and Perspectives. *J. Mater. Chem. C* **2023**, *11* (40), 13625–13646. https://doi.org/10.1039/D3TC02445H.

(234) Ni, Z.; Yu, Z.; Huang, J. Unveiling the Ambipolar Carrier Transport Property of SnO2−X for Multiple-Functional Interlayers in Perovskite Solar Cells. *Appl. Phys. Lett.* **2021**, *119* (12), 123501. https://doi.org/10.1063/5.0066843.

(235) Kuang, Y.; Zardetto, V.; van Gils, R.; Karwal, S.; Koushik, D.; Verheijen, M. A.; Black, L. E.; Weijtens, C.; Veenstra, S.; Andriessen, R.; Kessels, W. M. M.; Creatore, M. Low-Temperature Plasma-Assisted Atomic-Layer-Deposited SnO2 as an Electron Transport Layer in Planar Perovskite Solar Cells. *ACS Appl. Mater. Interfaces* **2018**, *10* (36), 30367–30378. https://doi.org/10.1021/acsami.8b09515.

(236) Bu, T.; Li, J.; Zheng, F.; Chen, W.; Wen, X.; Ku, Z.; Peng, Y.; Zhong, J.; Cheng, Y.-B.; Huang, F. Universal Passivation Strategy to Slot-Die Printed SnO2 for Hysteresis-Free Efficient Flexible Perovskite Solar Module. *Nat. Commun.* **2018**, *9* (1), 4609. https://doi.org/10.1038/s41467-018-07099-9.

(237) Zakaria, Y.; Aïssa, B.; Fix, T.; Ahzi, S.; Mansour, S.; Slaoui, A. Moderate Temperature Deposition of RF Magnetron Sputtered SnO2-Based Electron Transporting Layer for Triple Cation Perovskite Solar Cells. *Sci. Rep.* **2023**, *13* (1), 9100. https://doi.org/10.1038/s41598-023-35651-1.

(238) Ren, N.; Tan, L.; Li, M.; Zhou, J.; Ye, Y.; Jiao, B.; Ding, L.; Yi, C. 25% – Efficiency Flexible Perovskite Solar Cells via Controllable Growth of SnO_2. *iEnergy* **2024**, *3* (1), 39–45. https://doi.org/10.23919/IEN.2024.0001.

(239) *CRC Handbook of Chemistry and Physics*; Boca Raton, Fla. : CRC Press : Taylor & Francis Print began with 58th ed. (1977/1978)., 1978.

(240) Lu, Y.; Shih, M.-C.; Tan, S.; Grotevent, M. J.; Wang, L.; Zhu, H.; Zhang, R.; Lee, J.-H.; Lee, J.-W.; Bulović, V.; Bawendi, Moungi. G. Rational Design of a Chemical Bath Deposition Based Tin Oxide Electron-Transport Layer for Perovskite Photovoltaics. *Adv. Mater.* **2023**, *35* (45), 2304168. https://doi.org/10.1002/adma.202304168.

(241) Gao, L.; He, Z.; Zeng, K.; Liu, A.; Jiang, F.; Ma, T. Ultralow-Temperature SnO2 Electron Transport Layers Fabricated by Intermediate-Controlled Chemical Bath Deposition for Highly Efficient Perovskite Solar Cells. *ChemSusChem* **2023**, *16* (18), e202300765. https://doi.org/10.1002/cssc.202300765.

(242) Tian, S.; Gao, X.-X.; Reyes, D.; Syzgantseva, O. A.; Baytemirov, M. M.; Shibayama, N.; Kanda, H.; Schouwink, P. A.; Fei, Z.; Zhong, L.; Tiranito, F. F.; Fang, Y.; Dyson, P. J.; Nazeeruddin, M. K. Enhancing the Efficiency and Stability of Perovskite Solar Cells Using Chemical Bath Deposition of SnO2 Electron Transport Layers and 3D/2D Heterojunctions. *Small* **2024**, *20* (47), 2406929. https://doi.org/10.1002/smll.202406929.

(243) Wang, D.; He, T.; Li, S.; Jiang, Y.; Yuan, M. Li-Doped Chemical Bath Deposited SnO2 Enables Efficient Perovskite Photovoltaics. *ACS Appl. Energy Mater.* **2022**, *5* (5), 5340–5347. https://doi.org/10.1021/acsaem.1c02666.

(244) D. Wagner, C.; Naumkin, A. V.; Kraut-Vass, A.; Allison, J. W.; Powell, C. J.; Rumble, J. R. Jr. *The NIST X-Ray Photoelectron Spectroscopy (XPS) Database*; U.S. Government Priniting Office.

(245) Qiu, S.; Amaro, A.; Fabulyak, D.; Appleby-Millette, J.; Conover, C.; Zhang, D.; Yeddu, V.; Cheong, I. T.; Paci, I.; Saidaminov, M. I. Impact of Tetrakis(Dimethylamido)Tin(IV) Degradation on Atomic Layer Deposition of Tin Oxide Films and Perovskite Solar Cells. *Small* **2025**, *21* (1), 2404966. https://doi.org/10.1002/smll.202404966.

(246) Ko, Y.; Kim, T.; Lee, C.; Lee, C.; Yun, Y. J.; Jun, Y. Alleviating Interfacial Recombination of Heterojunction Electron Transport Layer via Oxygen Vacancy Engineering for Efficient Perovskite Solar Cells Over 23%. *ENERGY Environ. Mater.* **2023**, *6* (2), e12347. https://doi.org/10.1002/eem2.12347.

(247) Bai, C.; Dong, W.; Cai, H.; Zu, C.; Yue, W.; Li, H.; Zhao, J.; Huang, F.; Cheng, Y.-B.; Zhong, J. Electrochemical Reduction and Ion Injection of Annealing-Free SnO2 for High Performance Perovskite Solar Cells. *Adv. Energy Mater.* **2023**, *13* (26), 2300491. https://doi.org/10.1002/aenm.202300491.

(248) Li, Z.; Wang, C.; Sun, P.-P.; Zhang, Z.; Zhou, Q.; Du, Y.; Xu, J.; Chen, Y.; Xiong, Q.; Ding, L.; Nazeeruddin, M. K.; Gao, P. In-Situ Peptization of WO3 in Alkaline SnO2 Colloid for Stable Perovskite Solar Cells with Record Fill-Factor Approaching the Shockley–Queisser Limit. *Nano Energy* **2022**, *100*, 107468. https://doi.org/10.1016/j.nanoen.2022.107468.

(249) Du, B.; He, K.; Tian, G.; Che, X.; Song, L. Robust Electron Transport Layers of SnO 2 for Efficient Perovskite Solar Cells: Recent Advances and Perspectives. *J. Mater. Chem. C* **2023**, *11* (40), 13625–13646. https://doi.org/10.1039/D3TC02445H.

(250) Liu, S.; Li, H.; Zhang, Y.; Tang, Y.; Zhang, Z.; Li, H.; Wu, Y.; Li, Y.; Liu, X.; Wang, H. Decreased Accumulation of SnO2 Particles Results from Sodium Citrate Dispersant Assisted Chemical Bath Deposition for High Quality Perovskite Solar Cells. *Sol. RRL* **2024**, *8* (8), 2400020. https://doi.org/10.1002/solr.202400020.

(251) Vahdatifar, S.; Khodadadi, A. A.; Mortazavi, Y. Effects of Nanoadditives on Stability of Pt/SnO2 as a Sensing Material for Detection of CO. *Sens. Actuators B Chem.* **2014**, *191*, 421–430. https://doi.org/10.1016/j.snb.2013.10.010.

(252) Liu, Z.; Yang, X.; Sun, J.; Ma, F. PVDF Modified Pd-SnO2 Hydrogen Sensor with Stable Response under High Humidity. *Mater. Lett.* **2018**, *212*, 283–286. https://doi.org/10.1016/j.matlet.2017.10.105.

(253) Xu, D.-P.; Yu, L.-J.; Chen, X.-D.; Chen, L.; Sun, Q.-Q.; Zhu, H.; Lu, H.-L.; Zhou, P.; Ding, S.-J.; Zhang, D. W. In Situ Analysis of Oxygen Vacancies and Band Alignment in HfO_2/TiN Structure for CMOS Applications. *Nanoscale Res. Lett.* **2017**, *12* (1), 311. https://doi.org/10.1186/s11671-017-2068-y.

(254) Siol, S.; Hellmann, J. C.; Tilley, S. D.; Graetzel, M.; Morasch, J.; Deuermeier, J.; Jaegermann, W.; Klein, A. Band Alignment Engineering at Cu_2O/ZnO Heterointerfaces. *ACS Appl. Mater. Interfaces* **2016**, *8* (33), 21824–21831. https://doi.org/10.1021/acsami.6b07325.

(255) Kim, J. H.; Lee, J.; Kim, J. H.; Hwang, C. C.; Lee, C.; Park, J. Y. Work Function Variation of MoS2 Atomic Layers Grown with Chemical Vapor Deposition: The Effects of Thickness and the Adsorption of Water/Oxygen Molecules. *Appl. Phys. Lett.* **2015**, *106* (25), 251606. https://doi.org/10.1063/1.4923202.

(256) Casalongue, H. S.; Kaya, S.; Viswanathan, V.; Miller, D. J.; Friebel, D.; Hansen, H. A.; Nørskov, J. K.; Nilsson, A.; Ogasawara, H. Direct Observation of the Oxygenated Species during Oxygen Reduction on a Platinum Fuel Cell Cathode. *Nat. Commun.* **2013**, *4* (1), 2817. https://doi.org/10.1038/ncomms3817.

(257) Huang, B.; Zheng, L.; Hu, R.; Xuan, Y. All-SnO2-Based Conformal Electron Transport Layer for Efficient Perovskite Solar Cells. *Adv. Funct. Mater.* **2025**, *35* (14), 2419678. https://doi.org/10.1002/adfm.202419678.

(258) Huang, B.; Zheng, L.; Hu, R.; Xuan, Y. All-SnO2-Based Conformal Electron Transport Layer for Efficient Perovskite Solar Cells. *Adv. Funct. Mater.* **2025**, *35* (14), 2419678. https://doi.org/10.1002/adfm.202419678.

(259) M. Rombach, F.; A. Haque, S.; J. Macdonald, T. Lessons Learned from Spiro-OMeTAD and PTAA in Perovskite Solar Cells. *Energy Environ. Sci.* **2021**, *14* (10), 5161–5190. https://doi.org/10.1039/D1EE02095A.

(260) Luo, C.; Gao, F.; Wang, X.; Zhan, C.; Zhang, X.; Zheng, G.; Zhang, X.; Gao, X.; He, Z.; Zhao, Q. Eliminating Performance Loss from Perovskite Films to Solar Cells. *Sci. Adv.* **2024**, *10* (39), eadp0790. https://doi.org/10.1126/sciadv.adp0790.

(261) Akin, S.; Bauer, M.; Hertel, D.; Meerholz, K.; Zakeeruddin, S. M.; Graetzel, M.; Bäuerle, P.; Dar, M. I. Robust Nonspiro-Based Hole Conductors for High-Efficiency Perovskite Solar Cells. *Adv. Funct. Mater.* **2022**, *32* (45), 2205729. https://doi.org/10.1002/adfm.202205729.

(262) Afraj, S. N.; Velusamy, A.; Chen, M.-C.; Abd-Ellah, M.; Abdelhady, A. L. Heterocyclic and Heteropolycyclic Moieties in Organic Hole Transport Materials for Perovskite Solar Cells: Design, Synthesis, and Performance. *Coord. Chem. Rev.* **2025**, *532*, 216500. https://doi.org/10.1016/j.ccr.2025.216500.

(263) Saidaminov, M. I.; Abdelhady, A. L.; Murali, B.; Alarousu, E.; Burlakov, V. M.; Peng, W.; Dursun, I.; Wang, L.; He, Y.; Maculan, G.; Goriely, A.; Wu, T.; Mohammed, O. F.; Bakr, O. M. High-Quality Bulk Hybrid Perovskite Single Crystals within Minutes by Inverse Temperature Crystallization. *Nat. Commun.* **2015**, *6* (1), 7586. https://doi.org/10.1038/ncomms8586.

(264) Ahmed, Y.; Wang, W.; Kokaba, M. R.; Amaro, A.; Yeddu, V.; Gartside, H.; Awais, M.; Dayneko, S.; Zhang, D.; Parkin, H. C.; Cheong, I. T.; Marrugat-Arnal, V.; Brolo, A. G.; Saidaminov, M. I. PTAA/Perovskite Contact-Area Reduced Solar Modules. *ACS Energy Lett.* **2025**, 3306–3314. https://doi.org/10.1021/acsenergylett.5c01213.

(265) Azmi, R.; Utomo, D. S.; Vishal, B.; Zhumagali, S.; Dally, P.; Risqi, A. M.; Prasetio, A.; Ugur, E.; Cao, F.; Imran, I. F.; Said, A. A.; Pininti, A. R.; Subbiah, A. S.; Aydin, E.; Xiao, C.; Seok, S. I.; De Wolf, S. Double-Side 2D/3D Heterojunctions for Inverted Perovskite Solar Cells. *Nature* **2024**, *628* (8006), 93–98. https://doi.org/10.1038/s41586-024-07189-3.

(266) Fu, L.; Li, H.; Wang, L.; Yin, R.; Li, B.; Yin, L. Defect Passivation Strategies in Perovskites for an Enhanced Photovoltaic Performance. *Energy Environ. Sci.* **2020**, *13* (11), 4017–4056. https://doi.org/10.1039/D0EE01767A.

(267) Zhang, H.; Pfeifer, L.; Zakeeruddin, S. M.; Chu, J.; Grätzel, M. Tailoring Passivators for Highly Efficient and Stable Perovskite Solar Cells. *Nat. Rev. Chem.* **2023**, *7* (9), 632–652. https://doi.org/10.1038/s41570-023-00510-0.

(268) Seo, S.; Shin, S.; Kim, E.; Jeong, S.; Park, N.-G.; Shin, H. Amorphous TiO2 Coatings Stabilize Perovskite Solar Cells. *ACS Energy Lett.* **2021**, *6* (9), 3332–3341. https://doi.org/10.1021/acsenergylett.1c01446.

(269) Zheng, X.; Li, Z.; Zhang, Y.; Chen, M.; Liu, T.; Xiao, C.; Gao, D.; Patel, J. B.; Kuciauskas, D.; Magomedov, A.; Scheidt, R. A.; Wang, X.; Harvey, S. P.; Dai, Z.; Zhang, C.; Morales, D.; Pruett, H.; Wieliczka, B. M.; Kirmani, A. R.; Padture, N. P.; Graham, K. R.; Yan, Y.; Nazeeruddin, M. K.; McGehee, M. D.; Zhu, Z.; Luther, J. M. Co-Deposition of Hole-Selective Contact and Absorber for Improving the Processability of Perovskite Solar Cells. *Nat. Energy* **2023**, *8* (5), 462–472. https://doi.org/10.1038/s41560-023-01227-6.

(270) Nikbakht, H.; Mariani, P.; Vesce, L.; Giacomo, F. D.; Leonardi, E.; Viskadouros, G.; Spiliarotis, E.; Rogdakis, K.; Pescetelli, S.; Agresti, A.; Bellani, S.; Bonaccorso, F.; Kymakis, E.; Carlo, A. D. Upscaling Perovskite Photovoltaics: From 156 Cm2 Modules to 0.73 M2 Panels. *Adv. Sci.* *n/a* (n/a), 2416316. https://doi.org/10.1002/advs.202416316.

(271) Zhu, X.; Yu, D.; Zhou, X.; Wang, N.; Liu, H.; Liang, Z.; Wu, C.; Wang, K.; Jin, D.; Liu, S.; Yang, D. Interfacial Molecular Anchor for Ambient All-Bladed Perovskite Solar Modules. *Joule* **2025**, 101919. https://doi.org/10.1016/j.joule.2025.101919.

(272) Parvazian, E.; Watson, T. The Roll-to-Roll Revolution to Tackle the Industrial Leap for Perovskite Solar Cells. *Nat. Commun.* **2024**, *15* (1), 3983. https://doi.org/10.1038/s41467-024-48518-4.

(273) Yun, Y.; Chang, Q.; Yan, J.; Tian, Y.; Jiang, S.; Wei, W.; Li, S.; Guo, Y.; Yin, J.; Li, J.; Chen, M.; Huang, K.; Li, C.; Zhang, R. Dimensional Engineering of Interlayer for Efficient Large-Area Perovskite Solar Cells with High Stability under ISOS-L-3 Aging Test. *Sci. Adv.* **2025**, *11* (3), eadp3112. https://doi.org/10.1126/sciadv.adp3112.

(274) Zhang, W.; Li, Q.-S.; Li, Z.-S. Understanding the Surface Passivation Effects of Lewis Base in Perovskite Solar Cells. *Appl. Surf. Sci.* **2021**, *563*, 150267. https://doi.org/10.1016/j.apsusc.2021.150267.

(275) Han, G.; Hadi, H. D.; Bruno, A.; Kulkarni, S. A.; Koh, T. M.; Wong, L. H.; Soci, C.; Mathews, N.; Zhang, S.; Mhaisalkar, S. G. Additive Selection Strategy for High Performance Perovskite Photovoltaics. *J. Phys. Chem. C* **2018**, *122* (25), 13884–13893. https://doi.org/10.1021/acs.jpcc.8b00980.